# 國 立 交 通 大 學

## 應用化學研究所

## 博 士 論 文

# 自身模板輔助成長碳化矽奈米結構

# Self-Templating Assisted Growth of Silicon Carbide Nanostructures

研 究 生：王嘉興

指導教授：裘性天　博士

中 華 民 國 九 十 六 年 七 月

# 自身模板輔助成長碳化矽奈米結構

# Self-Templating Assisted Growth of Silicon Carbide Nanostructures


研 究 生： 王嘉興　　Student：Chia-Hsin Wang

指導教授： 裘性天 博士　　Advisor：Dr. Hsin-Tien Chiu


國 立 交 通 大 學

應 用 化 學 研 究 所

博 士 論 文

A Thesis

Submitted to Institute of Applied chemistry

College of Science

National Chiao Tung University

in Partial Fulfillment of the Requirements

for the Degree of Doctor of Science

in

Applied chemistry

July 2007

Hsinchu, Taiwan, Republic of China

中華民國九十六年七月

## Contents

# Self-Templating Assisted Growth of Silicon Carbide Nanostructures

Student: Chia-Hsin Wang Advisor: Dr. Hsin-Tien Chiu

Institute of Applied Chemistry, National Chiao Tung University

## Abstract:

In this thesis, we employ phase segregation as the concept to develop diverse SiC nanostructures via vapor-liquid and vapor-solid reactions. Inorganic salts $MCl_x$ (M=Na, Mg, Ca) act as templates generated in-situ to assist the morphology development.

First, cubic shells and spherical nanoparticles of β-SiC were produced at 1273 K by processing the ceramic precursors formed from the reactions between vapor of organochlorosilanes, $Me_2SiCl_2$, $MeSiCl_3$, $MeSiHCl_2$, and $PhSiCl_3$, and liquid Na at 523 – 723 K. From $Me_2SiCl_2$, a flexible linear polycarbosilane precursor was synthesized and covered the NaCl byproduct surface to from a cubic shape. Hollow cubic β-SiC shells were produced after the NaCl templates were removed. From $MeSiCl_3$, a rigid cross-linked polycarbosilane was produced and phase segregated from the NaCl byproduct. The precursor was transformed into nanoparticles without special morphology. $MeSiHCl_2$ produced a cross-linked polysilane precursor at low temperatures, which can be converted into a mixture of β-SiC and Si nanoparticles. At high temperatures, the polysilane converted to polycarbosilane and produced hollow cubic β-SiC shells. The carbon-rich $PhSiCl_3$ generated cube-like particles as the final product, which contained β-SiC and carbon.

In the second section, polycrystalline tubular SiC on Si was prepared by reacting $MeSiHCl_2$ vapor and Ca thin film on Si at 773 - 923 K followed by heat-treatment at 1273 K. The products phase-segregated into a cable-like radial heterostructure composed

of a core of $CaCl_2$ and a shell of $SiC_xH_y$. After removal of the $CaCl_2$ core, the layer of polycrystalline SiC tubes on Si emitted electrons at a low applied field of 2.5 V/μm with a current of 10 $\mu A/cm^2$.

In the third section, we also used the phase segregation concept in the reaction of $Me_2SiCl_2$ and $MeHSiCl_2$ between and magnesium metal at 823 - 923 K. The product was heat treated at 1273 K under vacuum. It showed pseudo thin plate SiC nanostructure, which was self-templated by $MgCl_2$ generated in situ.

In the fourth section, we extended the phase segregation idea to create porous SiC thin film on Si subtrate. Using $Sn(SiMe_3)_4$ as the precursor, amorphous $Si_xC_{1-x}$ thin films with Sn nanoparticles embedded were grown on Si substrates at 923 K by low pressure chemical vapor deposition. After treated under hydrogen plasma at 923 K, the Sn nanoparticles in the films were removed by an HF solution and by evaporation at 1423 K. Following the removal of Sn, high temperature treatments at 1273 - 1423 K converted the amorphous thin films into mesoporous semiconducting β-SiC thin films with pore sizes 10 - 100 nm.

Finally, one dimensional high aspect ratio Au nanowires were fabricated via galvanic reduction of $HAuCl_4$ solution in the presence of cetyltrimethylammonium chloride (CTAC) by the Sn nanoparticles embedded in amorphous the $Si_xC_{1-x}$ thin film product.

# 自身模板輔助成長碳化矽奈米結構

研究生：王嘉興　　指導教授：裘性天 博士

國立交通大學應用化學所

## 摘　要

在本論文裡，我們利用相分離的概念，藉由在氣液或氣固界面的化學反應來成長碳化矽奈米結構。反應過程中，自我生成的無機鹽類氯化鈉，氯化鎂，以及氯化鈣提供了形成奈米碳化矽形貌的模板。

首先，利用不同的氣態有機碳氯矽烷，二氯二甲基矽烷、三氯甲基矽烷、二氯甲基矽烷，和三氯苯基矽烷在 523 -723 K 下與液態的金屬鈉反應生成碳化矽的前驅物以及副產物氯化鈉。然後經過 1273 K 的熱處理，生成方形籠狀或圓球型態的碳化矽奈米結構。在利用氣態二氯二甲基矽烷反應時，一開始會生成具可撓曲的線性聚碳矽烷化合物覆著在副產物氯化鈉的表面上。經過熱處理後，可以移除氯化鈉，進而生成方形空心的碳化矽。使用三氯甲基矽烷反應時，則會生成硬性網狀聚碳矽烷化合物與副產物氯化鈉產生相分離，最後移去氯化鈉時，則得到圓球形狀的碳化矽奈米顆粒。然而在使用二氯甲基矽烷時，會因為反應溫度不同而生成不同型態的聚碳矽化合物。在較低溫下會產生硬性聚碳矽烷化合物，進而生成圓球形狀的碳化矽與矽奈米顆粒；而在較高溫度則是生成可撓曲的線性聚碳矽烷化合物，進而生成方形空心的碳化矽。除此之外，如果是具有較多碳的三氯苯基矽烷當前驅物，則會生成類方形碳/碳化矽空心顆粒。

在第二部份，我們利用物理氣相沈積的方法先在矽基材上沈積一層鈣薄膜。然後利用二氯甲基矽烷與鈣金屬在 773 – 923 K 反應 14 小時，之後經過 1273 K 的熱處理，就可以成功的合成出空心長條型態的碳化矽奈米結構。主要的原因是反應一開始副產物氯化鈣會與聚碳矽化合物相分離形成核殼狀的一維型態的產物，而經高溫處理氯化鈣被移除，聚碳矽化合物進而形成空心長條型態碳化矽結構。空心長條型態碳化矽結構可以用

於場發射的應用，實驗發現只需要提供相當低的電場 2.5 V/ μm 就會有 10 μA/$cm^2$ 電流密度的產生。

第三部分，我們再次驗證相分離的概念。藉由二氯甲基矽烷或二氯二甲基矽烷與氫氣電漿處理過後的鎂金屬在 823 K 或 923 K 下反應，之後在 1273 K 高溫熱處理，即可得到藉由自我產生的片狀氯化鎂模板的輔助，得到片狀碳化矽結構。

而在第四部份，我們將相分離的概念延伸到在矽基材上製作孔洞性的碳化矽薄膜。利用 $Sn(SiMe_3)_4$ 當作化學氣相沈積的前驅物，一開始先在 923 K 下成長薄膜；此時奈米錫顆粒會與無晶相的矽碳化合物產生相分離，而形成錫奈米顆粒鑲埋在矽碳化合物的薄膜。之後利用 HF 水溶液或在 1423 K 的高溫真空下將利用氫氣電漿在薄膜上的錫顆粒移除，即可生成孔洞碳化矽薄膜。我們也利用離子佈值的方式，將磷摻雜到 P-type 矽基材上的孔洞碳化矽薄膜，使其展現更好的 heterojunction diode 的性質。

最後，我們也利用錫奈米顆粒鑲埋在矽碳化合物的薄膜當作還原劑。藉由錫顆粒與金氯酸在具有氯化十六烷基三甲基銨鹽(CTAC)的水溶液下，行自發性的賈凡尼置換反應，在矽碳化合物的薄膜表面上生成一維的金奈米線。

# Acknowledgments

五年了，想不到我來交大已經有五年的時間了好像又念了一次大學一樣，新竹像埔里一樣我又多了另一個第二個家。雖然時間差不多，但是所經歷的以及所學到的是截然不同的。五年的研究生生活裡酸甜苦辣的日子都有，曾經為了趕 data 整夜不睡，曾經為了實驗結果不好而整夜難眠，但這些研究上的煩惱都會因實驗室歡樂的環境、實驗室夥伴門的相互討論、鼓勵及老師們的細心指導都會一一的迎刃而解。經過這五年的歷練，除了在學業知識方面學習到許多不同的東西外，在於生活與人生觀上也得到很多的啟發。這一切的提升，要感謝許多人支持與鼓勵。

首先，感謝指導教授裘性天教授在這段期間提供我一個相當優良的學習環境，讓我能夠充分學習、自由發揮，同時也要感謝老師在於研究思考方面的指導與開示，使我的思想更加廣闊、更加深遠。另外要特別感謝老師這一年來辛苦的幫我修改論文，讓我能夠順利的完成此篇論文。還有感謝一起 meeting 的李紫原教授在於實驗上的建議與指導，使得我的實驗能夠順利進行且更加的完備。

其次，感謝口試委員陳登銘教授與李積琛教授，不只在口試的時間指導我，且平時也會提供一些建議及實驗上的協助。此外也要感謝口試委員吳季珍教授，百忙當中從台南遠道而來指導我，使的我的論文能夠更加的完善。

還有感謝清交兩邊實驗室裡的大大小小，讓我在一個快樂的環境裡生活與學習。首先，感謝在交大實驗室的夥伴們，大學長張裕煦博士現在的張教授在我一開始進入實驗室時的教導，讓我受益良多。此外簡俊雄學長、閻明宇學長、周宜萱學姊、彭志偉學長、王隆昇學長、盛焙蓀學姊、陳盈薰學姊、夏志豪學長，還有同學及學弟妹，子厚、文昭、志豪、曜安、亭凱、進興、高翔、惶凱、蕭蕭、宇婕、sif、嘉芳、goby、昕君、季勳、大隻、馨緯、文志、大銘、妍如，大家在實驗室上的相互幫忙及一起玩樂，讓我的研究生活多彩繽紛。

另外也要感謝在清大實驗室的伙伴們，正得學長、鈺芬學姐，學弟們、旻橋、奕仁、聰盈、諺百、鑑嘉，雖然相處時間不多，但也不時的提供了許多實驗上的幫助，讓我實

驗更加的豐富。

還要感謝大學的同學俊邦、澄明、仲德、幫主在週末時、特殊節慶裡能夠一起吃飯聊天或則一起出遊，使我備感溫馨沒有孤單寂寞的感覺。

最後感謝我的家人，給於我無限的自由且能夠容忍念這麼久的時間，讓我順利的完成學業。還有相當感謝上天讓我幸運的遇到這麼多關心我、照顧我的貴人。謝謝。

## Contents of Schemes and Tables

## List of Figures

# Chapter 1

# Introduction

## 1.1 Introduction

Silicon and silicon-based materials have played an important role in the development of modern semiconductor device technology. Today, most of electronic products such as computer, cell phone, and digital audio player are produced by silicon semiconductor. However, silicon carbide (SiC) material has a very high breakdown field (3-5 MV/cm), typically 8-10 times higher than that for silicon (0.25 MV/cm), and prominent thermal conductivity of silicon carbide (3.2-4.9 $Wm^{-1}K^{-1}$) is 2-3 times higher than that for silicon (1.5 $Wm^{-1}K^{-1}$).[1] In addition, its excellent strength, hardness, and resistance to oxidation and thermal shock, SiC has more potential for application in harsh operation environments than widely utilized silicon devices.[2-4] Owing to these superior properties, lots of scientists are devoted to develop silicon carbide material in the last 100 years.

Recently, it is known that size of materials within the nanometer regime might have unique properties associated with their morphology and size. Nanostructured SiC could be a highly functional material.[5] For instance, Wong et al. showed that the elasticity and strength of SiC nanorod were greater than those of bulk SiC in a study of nanobeam mechanism.[6]

In this dissertation, we will reveal different types of SiC nanostructures, such as SiC nanoparticles, SiC nanocages, pseudo thin plate SiC nanostructures, tubular SiC nanostructures, and porous SiC thin films that can be fabricated based on the phase segregation concept. SiC nanostructures have very special properties which bode well for applications in blue light emitters, field emission display, hydrogen storage, photocatalytic and nanoscal electro-devices. In our study, potential application of tubular SiC as an efficient

field emitting material and fabrication of n-type porous SiC thin films on p-type silicon wafer to produce a heterjunction diode will be explored.

## 1.2 Structure and Properties of SiC

### *1.2.1 Structure of SiC*

SiC belongs to IV-IV semiconductors and there exist more than 130 polytypes.[7] All polytypes have a hexagonal frame with a carbon atom located above the center of a triangle of Si atoms and under a Si atom belonging to the next layer as shown in Figure 1.1.[8]

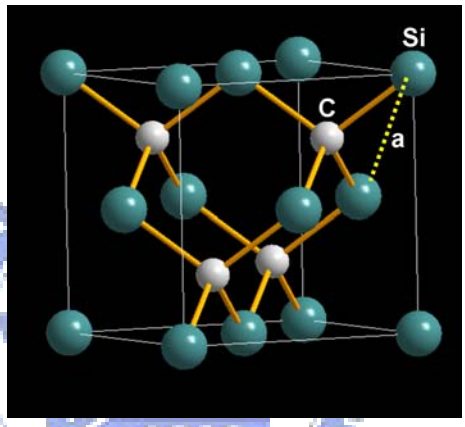


**Figure 1.1** The unit cell of 3C-SiC. The distance, a, between neighboring silicon, and C-Si are approximately 0.308 nm, and 0.189 nm, respectively.

The distance, a, between neighboring silicon or carbon atoms is approximately 0.308 nm for all polytypes.[9] The carbon atom is positioned at the center of mass of the tetrahedral structure outlined by four neighboring Si atoms so that the distance between the C atom to each of the Si atoms is the same. Geometrical considerations give that this distance, C-Si, is $(3/8)^{1/2}$a i.e. approximately equal to 0.189 nm. The polytypes of SiC differ from one another only in the stacking sequence of double layers of silicon and carbon atoms. The stacking direction is the c-axis in the hexagonal frame of reference.

The stacking sequence is shown for the most common polytypes, 3C, 2H, 4H and 6H in Figure 1.2. If the first double layer is called the A position, the next layer that can be placed

according to a closed packed structure will be placed on the B position or the C position. The different polytypes will be constructed by permutations of these three positions. For example, 3C-SiC will have a stacking sequence ABC while the number is the number of double layers in a stacking repeating sequence and the letter represents crystal structure which in this case is cubic. The only cubic form 3C-SiC sometimes referred to as β-SiC. If the double layers have

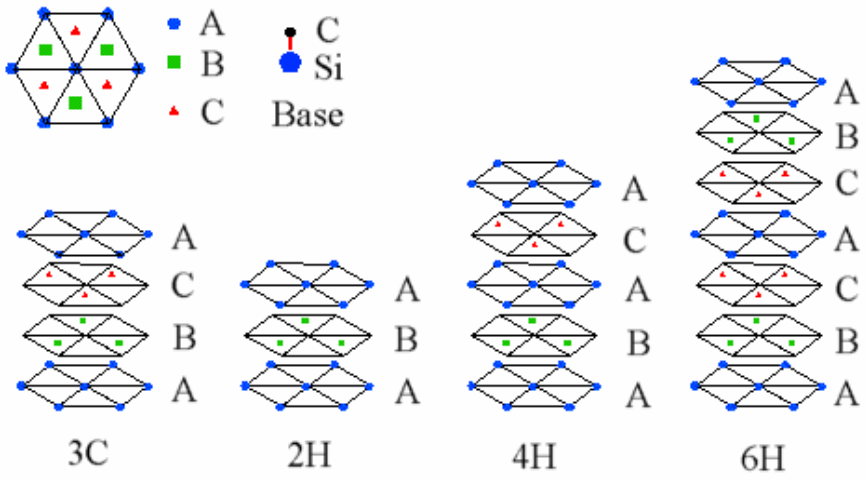


**Figure 1.2** The stacking sequence of double layers of the most common SiC polytypes.[8]

the same adjoining position, they have a 6-fold symetyaxis and crystallize into a hexagonal phase product. For example, 2H-SiC have a stacking sequence AB with a hexagonal structure. Other possibilities are ABAC, called 4H, and ABCACB, called 6H. All of hexagonal (H) or rhombohedral (R) polytypes expect cubic phase are commonly referred to as α–SiC. The crystal structure of 3C-SiC corresponds to cubic ZnS (zinc blende phase) and 2H, 4H, and 6H-SiC are hexagonal ZnS wurtzite phase.

### *1.2.2 Properties of SiC*

The color of 3C-SiC is yellow while 6H–SiC is colorless. The different polytypes of SiC have wide energy band gaps at room temperature from 2.2 eV for 3C-SiC, 2.9 eV for 6H-SiC

to 3.4 eV for 4H-SiC. The bandgaps at liquid helium temperature are 2.4 eV for 3C-SiC, 3.2 eV for 4H-SiC, 3.0 for 6H-SiC. [8,10,11,12] The other physical properties for most common types 3C, 4H, and 6H-SiC are summarized in Table 1.1.

**Table 1.1** Physical properties of the most common SiC polytypes. [8,10,11,12]

| | 3C-SiC | 4H-SiC | 6H-SiC |
|---|---|---|---|
| Bandgap (eV) at 5K | 2.4 | 3.2 | 3.0 |
| Space group | $F\bar{4}3m$ | $P6_3mc$ | $P6_3mc$ |
| Lattice *a* (nm) | 0.436 | 0.308 | 0.308 |
| Lattice *c* (nm) | 0.436 | 1.008 | 1.512 |
| Si-C Bond length (nm) | 0.189 | 0.189 | 0.189 |
| Density ($g/cm^3$) | 3.2 | 3.2 | 3.2 |
| Melting point (K) | 3103 | 3103 | 3103 |
| Mohs hardness | 9.0 | 9.0 | 9.0 |

In addition, we also show some important device parameters in terms of electric properties of most common types 3C, and 6H-SiC and other common semiconductors in Table 1.2. The maxium operating temperature for Si is 573 K, but for SiC, it is above 873 K. Below 1773 K, SiC is stable in an oxidizing atmosphere. This gives it an edge over diamond. Long term stability at high temperatures is a problem for III-V compounds, such as GaAs and GaP. These are reasons why SiC is considered as a good candidate for semiconductor device applications.

**Table 1.2** Electric properties of SiC and other semiconductors. [8,10,11,12]

| | Unit | Si | GaAs | 3C-SiC | 6H-SiC | Diamond |
|---|---|---|---|---|---|---|
| Bandgap at 5 K | eV | 1.12 | 1.43 | 2.4 | 3.0 | 5.6 |
| Electron mobility (R.T.) | $cm^2/V{\cdot}s$ | 1350 | 8500 | 1000 | 500 | 2200 |
| Hole mobility (R.T.) | $cm^2/V{\cdot}s$ | 480 | 400 | 40 | 80 | 1600 |
| Breakdown voltage | $10^6$ V/cm | 0.3 | 0.4 | 4 | 4 | 10 |
| Thermal conductivity | W/cm·K | 1.5 | 0.5 | 5.0 | 5.0 | 20.0 |
| Sat. elec. drift. vel. | $10^7$ V/s | 1.0 | 1.0 | 2.5 | 2.0 | 2.7 |

## 1.3 Synthetic Methods of SiC

The conventional processes for preparation of SiC material are the carbothermic reduction of silica carbon mixture, chemical vapor deposition techniques, and pyrolysis of polycarbosilane precursor. We will discuss more details below. In addition, self-propagating high temperature synthesis (SHS), based on the exothermic reaction between silicon micropowder and active carbon was carried out at ignition temperature of 1523 K - 1923 K.[13,14] Reduction-carbonization route, in which was carried out in autoclave using metallic Na as the reluctant, $SiCl_4$ and carbon, $CCl_x$ as source materials at 873 K - 923 K.[15,16] Na flux method by a mixture of silicon and fullerene powders were heating at 700 K- 1000 K in a sodium melt, and various other methods such as sol-gel, plasma, microwave radiation technologies have also been reported. [17-22]

In 1966, Klinger et al. studied the carbothermic reduction of silica carbon mixture to produce SiC at 1718 K- 2038 K under vacuum, which can be represented below by two equations 1.1-1.2.

$$SiO_{2(s)} + C_{(s)} \xrightarrow{1718\ K - 2038\ K} SiO_{(g)} + CO_{(g)} \quad (1.1)$$

$$SiO_{(g)} + 2C_{(s)} \xrightarrow{1718\ K - 2038\ K} SiC_{(s)} + CO_{(g)} \quad (1.2)$$

The reaction could proceed via the gas phase by dissociation of silica into oxygen and silicon monoxide and subsequent reaction with graphite to form vapor phase carbon monoxide and silicon carbide.[23] This is the most common route to produce SiC powders.

Chemical vapor deposition (CVD) is a single step process, which can deposit SiC material on an arbitrarily shaped substrate.[24,25] Most works use a silicon-containing and a carbon-containing gas-phase species, including a combination of $SiH_4$ and $CH_4$,[26-29] $SiH_4$ and $C_3H_8$,[30,31] and $Si_2H_6$ and $C_2H_2$.[32] For example, the $SiH_4$-$C_3H_8$-$H_2$ system, it is postulated that the following sequence of steps leads to the SiC.[33]

$$SiH_4 \xleftrightarrow{K_1} SiH_2 + H_2 \quad (1.3)$$

$$SiH_2 + X \xleftrightarrow{K_2} SiH_2.X \quad (1.4)$$

$$C_3H_8 \xleftrightarrow{K_3} CH_4 + C_2H_2 + H_2 \quad (1.5)$$

$$CH_4 + X \xleftrightarrow{K_4} CH_4.X \quad (1.6)$$

$$SiH_2.X + CH_4.X \xrightarrow{K_r} SiC_{(s)} + 3H_2 + 2X \quad (1.7)$$

Here X denotes the active substrate site, and D.X denotes the species D in the adsorbed state. The $K_i$'s are equilibrium constants and $K_r$ is the reaction rate constant for the bimolecular surface reaction Eqn. (1.7). At the beginning, $SiH_4$ and $C_3H_8$ decomposed in the gas phase to form $SiH_2$, $H_2$, $CH_4$, and $C_2H_2$ at high reaction temperature. Gas species of $SiH_2$ and $CH_4$ were absorbed on the active substrate site and reacted with each other to form SiC on the surface of the substrate.

Organochlorosilicon compounds, dichlorodimethylsilane ($Me_2SiCl_2$),[34,35] trichloromethylsilane ($MeSiCl_3$),[36,37] were used as single-source CVD precursors the organochlorosilane molecules first decomposed in the gas phase at high temperature 1273 K-1573 K in $H_2$ atmosphere to form intermediate species containing silicon and/or carbon atoms, followed by surface reactions on the substrate to form SiC films. Alkysilanes such as

hexmethyldisilane (HMDS), 1,1-dimethyl-1-silacyclobutabe, tetrakis(trimethylsilyl)silane (TMSS), and dodecamethylcyclohexasilane also acted as single-source CVD precursors. They decomposed into $H_2SiMe_2$, $HSiMe_3$, $Si_2Me_6$, and $[Me_2SiCH_2]$ at lower reaction temperature to form ceramic precursor layers. These were converted into crystalline SiC thin film by heat treatment above 1273 K.[38-41]

In general, CVD is a complicated process that includes (i) mass and energy transfer in the gas phase and (ii) gas-phase and surface chemical reaction. Film-growth species are sensitive to the reactor geometry and operating conditions. Therefore, it is necessary to design the CVD process and to choose suitable operating conditions.

In 1975, Yajima and his co-workers were the first successful in fabricating silicon carbide from preceramic organosilicon polymers.[42,43] The synthetic method is shown in equation 1.8. Metallic lithium was allowed to dechlorinate dimemethyldichlorosilane to

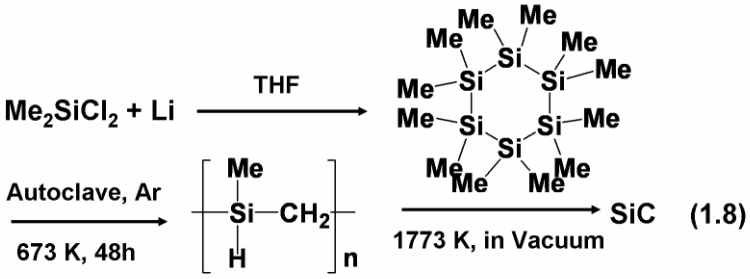


produce dodecamethylcyclohexasilane. The dodecamethylcyclohexasilane was purified by means of recrystallization and sublimation. It was heated at 673 K for 48 h in autoclave to produce polycarbosilane. After heat-treatment at 1773 K under vacuum, polycarbosilane converted into SiC. This is a complicated, expensive, and time-consuming method. In 1976, Yajima and co-workers improved the above method by replacing lithium with sodium as shown in equation 1.9.[44-49] The $Me_2SiCl_2$ was dechloroinated by the molten sodium, resulting in the precipitation of a linear, polydimethylsilane. After completion of the reaction, the

polysilane was removed by filitration and then heated at at 743 K for 5 h in argon gas atmosphere to form polycarbosilane. After heat-treatment at 1573 K under vacuum, the

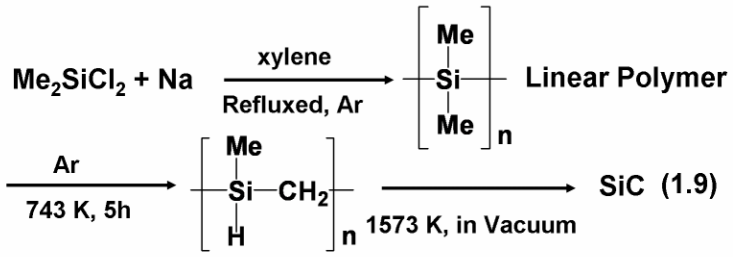


polycarbosilane converted into SiC. This synthetic method of polycarbonsilane is very simpler and more economical.

According to this process, Bianconi and her co-workers fabricated a netwok polymer polysilane, $[RSi]_n$. They used n-hexylSiCl$_3$ instead of $Me_2SiCl_2$ to react with metallic sodium/potassium (1:1) alloy in pentane solution. Pyrolysis of the netwokpolymer formed SiC with some Si.[50,51] In 1992, Seyfer's group also reported various partially linear and partially network precramic polymers, $[(MeSiH)_x(MeSi)_{1-x}]_n$, converted them into SiC with some Si follow by annealed at 1773 K .[52-54]

In this dissertation, we extend on the pyrolysis of polycarbosilane process to produce SiC. We simplified the Yajima process, using organochlorosilanes to react with metallic sodium, magnesium, and calcium in solvent-free condition at 523 K - 923 K. Then the products were converted into SiC nanostructure after heat treatment at 1273 K under vacuum. Besides, we also fabricated porous SiC thin films on Si substrate using a single-source precursor, $Sn(SiMe_3)_4$, by CVD process.

## 1.4 Nanostructures of SiC

### *1.4.1 SiC Nanocrystals*

There are many ways to prepare silicon carbide nanocrystals. These include cabothermic

reduction of silica, reduction-carbonization route, plasma, microwave radiation techniques and various chemical vapor deposition methods.[15-17,20,21,23] Recently, aqueous suspensions of 3C-SiC nanocrystals with a diameter 1-6 nm showing intense emission have been successfully fabricated by dispersing electrochemically etched porous polycrystalline 3C-SiC wafers in different solvents (water, ethanol, toluene).[55-56] The photoluminescence (PL) spectra exhibited continuous redshifts with increasing excitation wavelength and provides clear evidence of quantum confinement.[57-58] Based on this method, 3C-SiC/polystyrene composite films that luminescence in blue region have also been reported.[59] Thermal $SiO_2$ thin films have been implanted Si and C to produce SiC nanocrystals embedded in $SiO_2$ matrix can also exhibit PL emission. The origins of the luminescence were suggested to relate to defects in the silicon oxide at the SiC/$SiO_2$ interface, amorphous carbon clusters, or SiC grains.[60-64] Therefore, SiC nanocrystals have potential to be applied in blue light emitters in displays. Combined with their excellent biocompatibity, especially in blood, low density, and high rigidity SiC nanocrystals are potentially usefulin biology and medicine as well.[65,66]

### *1.4.2 One-Dimensional SiC Nanostructures*

One dimensional (1D) nanostructures such as rods, wires, belts, and tubes have been attracted much attention due to their unique application in mesoscopic physics and fabrication of nanoscale devices.[67-70] SiC 1D nanostructures have shown many outstanding performance because of their excellent properties. It can be used in field emission display, hydrogen storage, photocatalytic and nanoscal electro-devices.[71-73] Thus, many researchers have searched for methods to synthesize 1D SiC nanostructures in the last few years. 1D nanomaterials contains solid nanorods, nanowires, and hollow nanotubes. Below, we will divide into two sections to discuss some general methods to produce 1D SiC nanostructures.

### *1.4.2-1.1 SiC Nanorod and Nanowires from Hard Template Methods*

Since the discovery of carbon nanotubes by Iijima in 1991,[74] most of outstanding mechanical or electrical properties have been known in last few years.[75-76] They show promises in a wide variety of applications, including chemical sensors, field emitter, interconnects, and scanning probe.[77-80] In addition, carbon nanotubes open up new and exciting possibilities for making different kinds of nanosized heterostructures by filling the inside hollow space with other elements or by decorating the outside surfaces of the nanotubes. For example, various metal naowires, gallium nitride nanowires, and Si-B-C-N nanocable, have been synthesized using carbon nanotubes as templates.[81-83] These fabrication methods highly promising because of the morphological integrity of carbon nanotubes, which can spatially confine the reaction inside the nanotubes. The net result is the formation of one-dimensional products with diameters, lengths, and orientations similar to those the carbon nanotubes templates.

Carbon nanotube can act not only as a template but also as a reactant to produce 1D SiC material. Dai et al. successfully prepared SiC nanorods through a reaction between carbon nanotubes and SiO or $SiI_2$.[84] Pan et al. also fabricated SiC nanowires by using high aspect ratio aligned carbon nanotubes to react with SiO at 1673 K.[85]

### *1.4.2-1.2 SiC Nanorod and Nanowires from Vapor-Liquid-Solid Methods*

The growth of one-dimensional nanostructures via a gas phase reaction involving the vapor-liquid-solid (VLS) process has been widely studied. This process was originally developed by Wagner and co-workers to produce micrometer-sized whiskers in 1960s.[86] Recently, many research groups can generate nanowires and nanorods for a rich variety of inorganic materials.[87-90] The VLS process starts with the dissolution of gaseous reactants into nanosized liquid droplets of a catalyst metal. The saturated component would undergo nucleation, crystallization, and growth into rods and then wires. The 1D growth is mainly

induced and dictated by the liquid droplets of catalyst metal. Assuming that the size of the catalyze does not change during the wire growth, and the diameter of wire will be controlled by the liquid droplets of the catalyst metal. Wu et al. and co-workers have demonstrated the validity of VLS at nanometer scale by real-time observation of Ge nanowire growth in an high-temperature transmission electron microscopic (TEM).[91] Moreover, Bando's group effectively fabricated core-shell heterostructure SiC@BN, and SiC-$SiO_2$-C nanocable by VLS method.[92-93]

### *1.4.2-1.3 SiC Nanorod and Nanowires from Vapor-Solid Methods*

The vapor-solid (VS) method, without any metal catalysts for whisker growth, also holds for the growth of 1D nanomaterials.[94] In this process, evaporation, chemical reduction or gaseous reaction first generates the vapor. The vapor is gradually transported and condensed onto a substrate. Thus, it leads to the growth of 1D nanostructure. The supersaturation ratio of condensing species in the gas plays a key role. To enable anisotropic growth to form nanowires, the supersaturation ratio of condensing species must be controlled carefully otherwise, two-dimensional and isotropic growths would occur.[95,96]

Recently, our group reported that addition of poly(dimethylsiloxane) to a solvent-free vapor-solid reaction growth (VSRG) process assisted Cu nanowire formation significantly.[97] A simple high yield synthesis Ag nanowires which is carried out by using $AgNO_3$ and $(Me_3Si)_4Si$ were prepared in a sealed tube under low pressure at 400 K. The key step in this preparation is the in situ generation of a silica shell layer.[98] In VSRG, the reaction takes place at the vapor-solid interface, which is the surface of solid reactant. Phase separated solid product may develop into core-shell nanowires when the conditions are suitable. In additional, we also fabricated $CaF_2$@C and $MgF_2$@C core-shell 1D heterostructures through VSRG method.[99]

### *1.4.2-2 Tubular SiC*

Tubular 1 D materials such as carbon nanotube, vanadium oxide nanotube, and tungsten sulfide nanotube are caused by the transformation from curing the layered nanoparticles (2D) into nanotube (1D) in structure phase due to reduce the dangling bond at the edge of the plane when they are in nanometer size regime. [74,100,101] Other materials with normal crystal structure are difficult to form hollow nanotubes. Therefore, there were little reports on the synthesis of tubular silicon carbide 1 D nanostructures. Hu et al., Zhou et al., and Sun et al. used hard-template-assisted method to produce SiC nanotube. Drawbacks of these approaches include low yields, low crystalline, and difficulty to remove extra-templates. [102-104] It will be a challenge to produce a high yields tubular silicon carbide through a simple method.

### *1.4.3 Porous SiC Nanostructure*

Because of its potential usefulness for luminescence and sensing devices, porous silicon carbide thin film on SiC or Si also have been attracted much attention in recent years. Electrochemical etching of bulk silicon carbide substrates in HF solution, which the same process is used to form porous Si is the only method to fabricate it into the porous form onto SiC and Si wafers .[105-107] However, the route of electrochemical etching is not suitable for the fabrication of porous SiC thin films onto Si substrates. This is due to the high reactivity of Si towards the HF electrolyte, which would cause preferential dissolution of the Si substrate.[108] But porous SiC powders prepared via nanocasting and carbothermal reduction process have been reported.[109,110] Porous SiC powders are not easy to transform into thin films for electronic devices. In addition, it is difficult to produce non-oxide ceramic porous materials via sol-gel process.[111] Thus, it is a challenging issue to develop a new process to fabricate porous SiC on Si substrate for electronic device applications.

## 1.5 Goal of This Thesis

In this thesis, we simplify Yajima process via vapor-liquid or vapor-solid reaction in solvent-free conditions to fabricate SiC nanostructures based on the phase segregation concept. This is a new and simple method to fabricate various SiC nanostructures easily.

We employ various organochlorosilanes react with active metals Na, Ca, and Mg to form preceramic precursor and salt products. The salts work as templates to assist the structure formation. Spherical and nanocages of SiC are formed via the ceramic precursor and the byproduct NaCl. One dimensional SiC nanotubes are successful developed from the precursor and $CaCl_2$. From the byproduct, $MgCl_2$, and the precursor, pseudo thin plate SiC nanostructure can be prepared also.

In addition, we extend the phase segregation concept to grow porous β-SiC thin film onto silicon wafer. Using $Sn(SiMe_3)_4$ as the single-source precursor for metal-organic chemical vapor deposition (MOCVD). SiC thin film with embedded Sn nanoparticles can be grown. The metal Sn particles act as in situ generated templates to assist the formation of porous SiC thin films.

The detail experimental conditions of these results will be discussed in the following chapters.

## 1.6 References


(1) Casady, J. B.; Johnson, R. W. *Solid-State Electron*. **1996**, *39*, 1409.

(2) Niihara, K. *Ceram. Bull.* **1984**, *63*,1160.

(3) Narushima, T.; Goto, T.; Lguchi, Y.; Hirai, T. *J. Am. Ceram. Soc.* **1990**, *73*, 3580.

(4) Spetz, A. L.; Baranzani, A.; Tobias, P.; Lundström, I. *Phys. Stat. Sol. (a)* **1997**, *162*, 493.

(5) Devaty R. P.; Choyke W. J. *Phys Stat Sol (a)* **1997**, *162*, 5.

(6) Wong, E. W.; Sheehan, P. E.; Lieber, C. M. *Science* **1997**, *277*, 1971.

(7) Verma, A. R.; Krishna, P. Polymorphism and Polytypism in Crystals, Wiley, New York, **1966**, Chapter 5, p 92.

(8) http://www.ifm.liu.se/matephys/new_page/research/sic/

(9) Knippenberg, W. F. *Philips Research Reports*, **1963**, *18*, 161.

(10) Harris, G. L.; Yang, C. Y.-W. Amorphous and Crystalline Silicon Carbide, **1987**, Part I, p 3.

(11) Harris, G. L. Properties of Silicon Carbide, Inspec, U.K., **1995**, Chapter 2, p 31.

(12) Zetterling, C.-M. Process Technology for Silicon Carbide Devices, Inspec, U.K., **2002**, Chapter 2, p 4.

(13) Pampuch, R.; Stobierski, L.; Lis, J.; Raczka, M. *Mater. Res. Bull.* **1987**, *22*, 1225.

(14) Narayan, J.; Raghunathan, R.; Chowdhury, R.; Jagannadham, K. *J. Appl. Phys.* **1994**, *75*, 7252.

(15) Hu, J.-Q.; Lu, Q.-Y.; Tang, K.-B. ; Qian, Y.-T. ; Zhou, G.-E. ; Liu, X.-M. ; Wu, J.-X. *Chem. Mater.* **1999**, *11*, 2369.

(16) Shen, G.-Z ; Chen, D. ; Tang, K.B. ; Qian, Y.-T. ; Zhang, S.-Y. *Chem.Phys. Lett.* **2003**, *375*, 177.

(17) Kawamura, F.; Yamane, H.; Yamada, T.; Yin, S.; Sato, T. *J. Ceram. Soc. Jpn.* **2007**, *115*, 74.

(18) Hatakeyama, F.; Kanzaki, S. *J. Am. Ceram. Soc.* **1990**, *73*,2107.

(19) Seog, I. S.; Kim, C. H. *J. Mater. Sci.* **1993**, *28*, 3227.

(20) Zhu, W.; Zhao, G. Y.; Revankaar, V.; Hlavacek, V. *J. Mater. Sci.* **1993**, *28*, 659.

(21) Guo, J. Y.; Gitzhofer, F.; Boulos, M. I. *J. Mater. Sci.* **1995**, *30*, 5589.

(22) Ramesh, P. D.; Vaidhyanathan, B.; Ganguli, M.; Rao, R. J. *J. Mater. Res.* **1994**, *9*, 3025.

(23) Klinger, N. ; Strauss, E. L. ; Komarek K. L. *J. Am. Ceram. Soc.* **1966**, 49, 369.

(24) Schlichting, J. *Powder Metal. Int.* **1980**, *12*, 141.

(25) Fischman, G. S.; Petuskey, W. T. *J. Am. Ceram. Soc.* **1985**, *68*, 185.

(26) Tabata, A.; Nakajima, T.; Mizutani, T.; Suzuoki, Y. *Jpn. J. Appl. Phys.* **2003**, *42* 10.

(27) Schroder, B.; Holger, U.; Lederman, A.; Mukherjee, C. *Thin Solid Films* **2001**, *395*, 298.

(28) Itoh, T.; Fujiwara, T.; Katoh, Y.; Fukunaga, K.; Nonomura, S. *J. Non-Cryst. Solids* **2002**, *299–302*, 880.

(29) Yu, Rusli, M. B.; Yoon, S. F.; Chen, Z. M.; Ann, J.; Zhang, Q.; Chew, K.; Cui, J. *J. Appl. Phys.* **2000**, *87*, 8155.

(30) Nishino, S.; Suhara, H.; Ono, H.; Matsunami, H. *J. Appl. Phys.* **1987**, *61*, 4889.

(31) Allendorf, M. D.; Kee, H. J. *J. Electrochem. Soc.* **1991**, *138*, 841.

(32) Hong, L.-S.; Shimogaki, V.; Egashira, V.; Komiyama, H. *J. Electrochem. Soc.* **1992**, *139*, 3652.

(33) Harris, G. L.; Yang, C. Y.-W. Amorphous and Crystalline Silicon Carbide, **1987**, Part I, p 51.

(34) Takeuchi, T.; Egashira, Y.; Osawa, T.; Komiyama, H. *J. Electrochem. Soc.* **1998**, *145*, 1277.

(35) Chen, L.; Goto, T.; Hirai, T. *J. Mater. Sci.* **1990**, *25*, 4614.

(36) Choi, B. J.; Kin, D. R. *J. Mater. Sci. Lett.* **1991**, *10*, 860.

(37) Fu, Q.-G. ; Li, H.-J. ; Shi, X.-H.; Li, K.-Z.; Wei, J.; Hu, Z.-B. *Mater. Chem. Phys.* **2006**, *100*, 108.

(38) Chiu, H.-T.; Huang, S.-C. *J. Mater. Sci. Lett.* **1993**, *12*, 537.

(39) Chiu, H.-T.; Hsu, J.-S. *Thin Solid Films* **1994**, *252*, 13.

(40) (a) Chiu, H.-T.; Lee, S.-F. *J. Chin. Chem. Soc.* **1992**, *39*, 239. (b) Chiu, H.-T.; Lee, S.-F. *J. Mater. Sci. Lett.* **1991**, *10*, 1323. (c) Chiu, H.-T.; Wu, P.-F. *J. Chin. Chem. Soc.* **1991**, *38*, 231.

(41) (a) Wróbel, A. M.; Wickramanayaka, S.; Nakanishi, Y.; Hatanaka, Y.; Pawłowski, S.; Olejniczak, W. *Diamond Relat. Mater.* **1997**, *6*, 1081. (b) Wróbel, A. M.; Walkiewicz-Pietrzykowska, A. *Chem. Vap. Deposition* **1998**, *4*, 133.

(42) Yajima, S.; Hayashi, J.; Omori, M. *Chem. Lett.* **1975**, 931.

(43) Yajima, S.; Okamura, K.; Hayashi, J. *Chem. Lett.* **1975**, 1209.

(44) Yajima, S.; Omori, M.; Hayashi, J.; Okamura, K.; Matsuzawa, T.; Liaw, C.-F. *Chem. Lett.* **1976**, 551.

(45) Yajima, S.; Hayashi, J.; Omori, M.; Okamura, K. *Nature* **1976**, *261*, 683.

(46) Yajima, S.; Hayasht, J.; Hasegawa, Y.; Iimura, M. *J. Mater. Sci.* **1978**, *13*, 2569.

(47) Hasegawa, Y.; Iimura, M.; Yajima, S. *J. Mater. Sci.* **1980**, *15*, 720.

(48) Hasegawa, Y.; Okamura, K. *J. Mater. Sci.* **1983**, *18*, 3633.

(49) Ichikawa, H; Machino, F.; Mitsuno, S.; Ishikawa, T.; Okamura, K.; Hasegawa, Y. *J. Mater. Sci.* **1986**, *21*, 4352.

(50) Bianconi, P. A.; Weidman, T. W. *J. Am. Chem. Soc.* **1988**, *110*, 2342.

(51) Bianconi, P. A.; Schilling, F. C.; Weidman, T. W. *Macromolecules* **1989**, *22*, 1697.

(52) Seyferth, D.; Wood, T. G.; Tracy, H. J.; Robison, J. I. *J. Am. Ceram. Soc.* **1992**, *75*, 1300.

(53) Seyferth, D.; Lang, H. *Organometallics* **1991**, *10*, 551.

(54) Czubarow, P.; Sugimoto, T.; Seyferth, D. *Macromolecules* **1998**, *31*, 229.

(55) Wu, X. L.; Fan, J. Y.; Qiu, T.; Yang, X.; Siu, G. G.; Chu, P. K. *Phys. Rev. Lett.* **2005**, *94*, 26102.

(56) Fan, J. Y.; Wu, X. L.; Li, H. X.; Liu, H. W.; Siu, G. G.; Chu, P. K. *Appl. Phys. Lett.*

(57) Efros, Al. L.; Efros, A. L.; *Sov. Phys. Semicond.* **1982**, *16*, 772.

(58) Brus, L. *J. Chem. Phys.* **1983**, *79*, 5566.

(59) Fan, J. Y.; Wu, X. L.; Kong, F.; Qiu, T.; Huang, G. S. *Appl. Phys. Lett.* **2005**, *86*, 171903.

(60) Fan, J. Y.; Wu, X. L.; Chu, P. K. *Prog. Mater. Sci.* **2006**, *51*, 983.

(61) Zhao, J.; Mao, D.S.; Lin, Z.X.; Jiang, B.Y.; Yu, Y.H.; Liu, X. H.; Wang, H. Z.; Yang, G. Q. *Appl Phys Lett* **1998**, **73**, 1838.

(62) Pérez-Rodríguez, A.; González-Varona, O.; Garrido, B.; Pellegrino, P.; Morante, J. R.; Bonafos, C.; Carrada, M.; Claverie, A. *J. Appl. Phys.* **2003**, *94*, 254.

(63) Chen, D.; Liao, Z. M.; Wang, L.; Wang, H. Z.; Zhao, F.; Cheung, W. Y. *Opt. Mater.* **2003**, *23*, 65.

(64) An, Z.; Fu, R. K. Y.; Chen, P.; Liu, W.; Chu, P. K.; Lin, C. *J. Vac. Sci. Technol. B* **2003**, *21*, 1375.

(65) Chan, W. C. W.; Nie, S. *Science* **1998**, *281*, 2016.

(66) Bruchez, J. M.; Moronne, M.; Gin, P.; Weiss, S.; Alivisatos, A. P. *Science* **1998**, *281*, 2013.

(67) Wang, Z. L. *Adv. Mater.* **2000**, *12*, 1295.

(68) Xia, Y.; Yang, P.; Sun, Y.; Wu, Y.; Mayers, B.; Gates, B.; Yin, Y.; Kim, F.; Yan, H. *Adv. Mater.* **2003**, *15*, 353.

(69) Hu, J.; Odom, T. W.; Liber, C. M. *Acc. Chem. Res.* **1999**, *32*, 435.

(70) Rao, C. N. R.; Deepak, F. L.; Gundiah, G.; Govindaraj, A. *Prog. Solid State Chem.* **2003**, *31*, 5.

(71) Lo, H. C.; Das, D.; Hwang, J. S.; Chen, K. H.; Hsn, C. H.; Chen, C. F.; Chen, L. C. *Appl. Phys. Lett.* **2003**, *83*, 1420.

(72) Mpourmpakis, G.; Froudakis, G. E. ; Lithoxoos, G. P.; Samios, J. *Nano Lett.* **2006**, *6*, 1581.

(73) Zhou, W.; Yan, L.; Wang, Y.; Zhang, Y. *Appl. Phys. Lett.* **2006**, *89*, 013105.

(74) Iijima, S. *Nature* **1991**, *354*, 56.

(75) Hone, J.; Batlogg, B.; Benes, Z.; Johnson, A. T.; Fischer, J. E. *Science* **2000**, *289*, 1730.

(76) Yu, M. F.; Files, B. S. ; Arepalli, S. ; Ruoff, R. S. *Phys. Rev. Lett.* **2000**, *84*, 5552.

(77) Li, J.; Lu, Y.; Ye, Q.; Cinke, M.; Han, J.; Meyyappan, M. *Nano Lett.* **2003**, *3*, 929.

(78) Cassell, A. M.; Ye, Q.; Cruden, B. A. ; Li, J. ; Sarrazin, P. C.; Ng, H. T.; Han, J.; Meyyappan, M. *Nanotechnol.* **2004**, *15*, 9.

(79) Li, J.; Ng, H. T.; Cassell, A. M.; Fan, W.; Chen, H.; Ye, Q.; Koehne, J.; Han, J.; Meyyappan, M. *Nano Lett*. **2003**, *3*, 597.

(80) Dai, H.; Hafner, J. H.; Rinzler, A. G.; Colbert, D. T.; Smalley, R. E. *Nature* **1996**, *384*, 147.

(81) Guerretpiecout, C.; Lebouar, Y.; Loiseau, A.; Pascard, H. *Nature*, **1994**, *372*, 761.

(82) Han, W. Q. ; Fan, S. S. ; Li, Q. Q.; Hu, Y. D. *Science*, **1997**, *277*, 1287.

(83) Zhang, Y.; Suenaga, K.; Colliex, C.; Iijima, S. *Science* **1998**, *281*, 973.

(84) Dai, H. J.; Wong, E. W. ; Lu, Y. Z.; Fan, S. S.; Lieber, C. M. *Nature* **1995**, *375*, 769.

(85) Pan, Z. W.; Lai, H. L.; Au, F. C. K.; Duan, X. F.; Zhou, W. Y.; Shi, W. S.; Wang, N.; Lee, C. S.; Wong, N. B.; Lee, S. T.; Xie, S. S. *Adv. Mater.* **2000**, *12*, 1186.

(86) Wagner, R. S.; Ellis, W. C. *Appl. Phys. Lett.* **1964**, *4*, 89.

(87) Duan, X. ; Liber, C. M. *Adv. Mater.* **2000**, *12*, 298.

(88) Wu, Y.; Yang, P. *Chem. Mater.* **2000**, *12*, 605.

(89) Chen, C.-C.; Yeh, C.-C.; Chen, C.-H.; Yu, M.-Y.; Liu, H.-L.; Wu, J.-J.; Chen, K.-H.; Chen, L.-C.; Peng, J.-Y.; Chen, Y.-F. *J. Am. Chem. Soc.* **2001**, *123*, 2791.

(90) Huang, M. H.; Wu, Y.; Feick, H. J.; Tran, N.; Weber, E.; Yang, P. *Adv. Mater.* **2001**, *13*, 113.

(91) Wu, Y.; Yang, P. *J. Am. Chem. Soc.* **2001**, *123*, 3165.

(92) Tang, C. C.; Bando, Y.; Sato, T.; Kurashima, K.; Ding, X. X.; Gan, Z. W.; Qi, S. R. *Appl.*

*Phys. Lett.* **2002**, *80*, 4641.

(93) Li, Y.; Bando, Y; Golberg, D. *Adv. Mater.* **2004**, *16*, 93.

(94) Levitt, A. P. Whisker Technology, Wiley-Interscience, New York **1970**.

(95) Hsu, Y.-J; Lu, S.-Y. *J. Phys. Chem. B* **2005**, *109*, 4398.

(96) Wang, Y.; Zhang, L.; Meng, G.; Liang, C.; Wang, G.; Sun, S. *Chem. Commun.* **2001**, 2632.

(97) Yen, M.-Y.; Chiu, C.-W.; Shia, C.-H.; Chen, F.-R.; Kai, J.-J.; Lee, C.-Y.; Chiu, H.-T. *Adv.Mater.* **2003**, *15*, 235.

(98) Hsia, C.-H.; Yen, M.-Y.; Lin, C.-C.; Chiu, H.-T.; Lee, C.-Y. *J. Am. Chem. Soc.* **2003**, *125*, 9940.

(99) Huang, C.-H.; Chang, Y.-H.; Lee, C.-Y.; Chiu, H.-T. *Langmuir* **2006**, *22*, 10.

(100) Patzke, G. R.; Krumeich, F.; Nesper, R. *Angew. Chem. Int. Ed.* **2002**, *41*, 2447.

(101) Rosentsveig, R.; Margolin, A.; Feldman, Y.; Popovitz-Biro, R.; Tenne, R. *Chem. Mater.* **2002**, *14*, 471.

(102) Sun, X. H.; Li, C. P.; Wong, W. K.; Wong, N. B.; Lee, C. S.; Lee, S. T.; Teo, B. K. *J. Am. Chem. Soc.* **2002**, *124*, 14464.

(103) Hu, J. Q.; Bando, Y.; Zhan, J. H.; Golberg, D. *Appl. Phys. Lett.* **2004**, *85*, 2932.

(104) Wang, H.; Li, X.-D.; Kim, T.-S.; Kim, D.-P. *Appl. Phys. Lett.* **2005**, *86*, 173104.

(105) Matsumoto, T.; Takahashi, J.; Tamaki, T.; Futagi, T.; Mimura, H.; Kanemitus. Y. *Appl. Phys. Lett.* **1994**, *64*, 226.

(106) Connolly, E. J.; Timmer, B.; Pham, H. T. M.; Groeneweg, J.; Sarro, P. M.; Olthuis, W.; French, P. J. *Sens. Actuators B* **2005**, *109*, 44

(107) Rittenhouse, T. L.; Bohn, P. W.; Hossain, T. K.; Adesida, I.; Lindesay, J.; Marcus, A. *J. Appl. Phys.* **2004**, *95*, 490.

(108) Takazawa, A.; Tamura, T.; Yamada, M. *Jpn. J. Appl. Phys.* **1993**, *32*, 3148.

(109) Krawiec, P.; Geiger, D.; Kaskel, S. *Chem. Commun.* **2006**, 2469.

(110) Sonnenburg, K.; Adelhelm, P.; Antonietti, M.; Smarsly, B.; Nöske, R.; Strauch, P. *Phys. Chem. Chem. Phys.* **2006**, *8*, 3561.

(111) Soler-IIIia, G. J. de A. A.; Sanchez, C.; Lebeau, B.; Patarin, J. *Chem. Rev.* **2002**, *102*, 4093.

# Chapter 2

# Silicon Carbide Nanostructures from Reactions between Vapors of Organochlorosilanes and Liquid of Sodium - Factors Affecting Morphology and Composition

## 2.1 Introduction

Through its excellent strength, hardness, and resistance to oxidation and thermal shock, SiC is an attractive material for applications in harsh environments.[1-2] Common methods to produce silicon carbide solids include carbothermal reduction of silica, sol-gel synthesis, and various chemical vapor deposition techniques.[3-8] In 1975, Yajima and co-workers were the pioneers successful in fabricating silicon carbide from preceramic organosilicon polymers.[9] Now, there are many reports about the preceramic polymers, prepared by Wurtz type coupling of organochlorosilanes by sodium in polar organic solvents.[10-12] Previously, we communicated the preparation of new-type silicon carbide nanostructures via a simplified Yajima process.[13] In the reaction, vapor phase methylchlorosilanes reacted with liquid phase sodium in a solvent-free environment. The NaCl byproduct acted as an in-situ generated template to affect the final product morphology. Formation of silicon carbide nanoparticles, cubical nanoshells, and cubical nanocages was observed. We suggested that the bonding and the structure of the ceramic precursor would affect the morphology also. In this article, we will discuss in detail the preparation and characterization of the ceramic precursors synthesized from direct reactions between organochlorosilane vapors and liquid sodium and the conversion of these precursors into silicon carbide with unique morphology.

## 2.2 Experimental

### *2.2.1 Materials*

$Me_2SiCl_2$, $MeSiCl_3$, $MeHSiCl_2$, and NaH purchased from Aldrich and $PhSiCl_3$ obtained from Echo Chemical were used in the reactions without further purification.

### *2.2.2 Synthesis of sample DD from $Me_2SiCl_2$ and Na*

A summary of reaction conditions and experimental observations is listed in Table 2.1. The reaction employing $Me_2SiCl_2$ to react with Na is described below as a typical example.

Inside a horizontal tube furnace at 623 K, NaH (0.20 g, 8.3 mmole) in a quartz boat was thermally decomposed in a 30-mm quartz tube under 1 atm of Ar (flow rate: 20 sccm) for 1 h. Then, $Me_2SiCl_2$ was evaporated at 255 K under the assistance of a constant flow of Ar (1 - 2 sccm) into the reactor at 623 K 1 atm. After 20 h, a ceramic precursor **Pre-DD** was obtained. The precursor was further heated at 1273 K for 1 h under vacuum to offer a black powder **DD**.

### *2.2.3 Characterization*

Scanning electron microscopic (SEM) and energy dispersive X-ray (EDX) data were collected using Hitach S-4000 and JEOL JSM-6330F at 15 kV. Transmission electron microscopic (TEM) and electron diffraction (ED) images were obtained on Philips TECNAI 20 and JEOL JEM-2010 at 200 kV. High resolution TEM (HRTEM) images were acquired on JEOL JEM-4000EX at 400 kV. X-ray diffraction (XRD) studies were obtained using MAC MXP-18 and BRUKER AXS D8 ADVANCE diffractometer with Cu $K_\alpha 1$ radiation. Fourier transform infrared (FT-IR) spectra were measured using Perkin Elmer Spectrum One and Nicolet Avatar 360. Thermogravimetric analysis (TGA) data were collected using Seiko SSC 5200 TGA in Ar ambiance. $^{29}Si$ solid state NMR SSNMR) spectra were obtained from

BRUKER DSX400WB. UV-visible spectra were measured with Hitachi 3010.

### 2.3 Results

As shown in Scheme 2.1, vapors of organochlorosilanes $R_xSiH_yCl_{(4-x-y)}$ (R = Me, (x,y) = (2,0), (1,0), (1,1) and R = Ph, (x,y) = (1,0)) were reacted with liquid Na, prepared by decomposing NaH at 623 K,[14] at 523 – 723 K to form NaCl and ceramic precursors composed of Si, C and H. The precursors **Pre-DD**, **Pre-MT**, **Pre-MD-523**, **Pre-MD-673**, and **Pre-MD-723** were isolated from the reactions involving $Me_2SiCl_2$ and $MeSiCl_3$ at 623 K, and $MeSiHCl_2$ at 523, 673, and 723 K, respectively. These precursors were further processed at 1273 K to form the final products, **DD**, **MT**, **MD-523**, **MD-673** and **MD-723**, correspondingly. In the reactions employed $PhSiCl_3$ at 573 and 723 K, the as-produced precursors were not isolated and characterized. They were processed directly to the final products **PT-573** and **PT-723**. A summary of the experimental data, including the overall reaction conditions and general information of the products is listed in Table 2.1. These will be discussed in detail below.

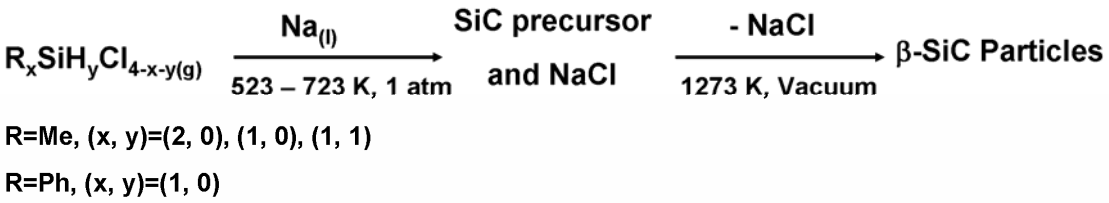


**Scheme 2.1** Summary of reaction processes**.**

**Table 2.1** Summary of reactions between sodium and organochlorosilanes**.**

| Product Sample | Silane | Reaction T (K) | Isolated Ceramic Precursor | Product Color | Product and Morphology from precursor heated at 1273 K | Composition | Grain Size (nm)[a] |
|---|---|---|---|---|---|---|---|
| **DD** | $Me_2SiCl_2$ | 623 | **Pre-DD** | Black | Cubic Particles (edge: 1 - 2 μm) | β-SiC | 4.5 |
| **MT** | $MeSiCl_3$ | 623 | **Pre-MT** | Yellow | Spherical Particles (diameter: 10 nm) | β-SiC | 7.3 |
| **MD-523** | $MeSiHCl_2$ | 523 | **Pre-MD-523** | Yellow | Irregular Aggregates (size: 1 - 3 μm) of Particles (diameter: 40 - 90 nm) | Si and β-SiC | Si: 23.4 β-SiC: 4.0 |
| **MD-673** | $MeSiHCl_2$ | 673 | **Pre-MD-673** | Yellow | Mixture of Cubic (edge: 1 - 1.5 μm) and Spherical Particles (diameter: 5 - 10 nm) | Si and β-SiC | Si: 9.6 β-SiC: 5.0 |
| **MD-723** | $MeSiHCl_2$ | 723 | **Pre-MD-723** | Yellow | Cubic Particles (edge: 1 - 2 μm) | β-SiC | 5.7 |
| **PT-573** | $PhSiCl_3$ | 573 | - | Black | Cubic-like Particles (diameter: 100 - 300 nm) | β-SiC and graphite(minor) | 3.9 C: 1.0 |
| **PT-723** | $PhSiCl_3$ | 723 | - | Black | Cubic Particles (edge: 400 - 800 nm) | β-SiC and graphite (major) | β-SiC: 7.6 C: 2.2 |

[a]Grain sizes were calculated from the β-SiC (111), Si (111), and C (002) reflection widths in XRD using the Scherrer equation.

### *2.3.1 Characterizations of Ceramic Precursors*

SEM images of **Pre-DD** and **Pre-MT** are shown in Figures 2.1A and 2.1B as the examples for the morphology of the ceramic precursors. **Pre-DD** displays isolated cubic particles with edge lengths of 500 – 800 nm. Apparently, the particles contain a precursor shell layer which covers the surface of the inner cubic core. The image of **Pre-MT** shows a mixture of a precursor material and cubic particles with smooth surface. EDX data of the precursors (insets) suggest that they contain Na, Cl, Si, and C. A representative XRD pattern of **Pre-DD**, as shown in Figure 2.1C, can be indexed to NaCl.[15] XRD data of the other ceramic precursors also confirm the presence of NaCl**.**

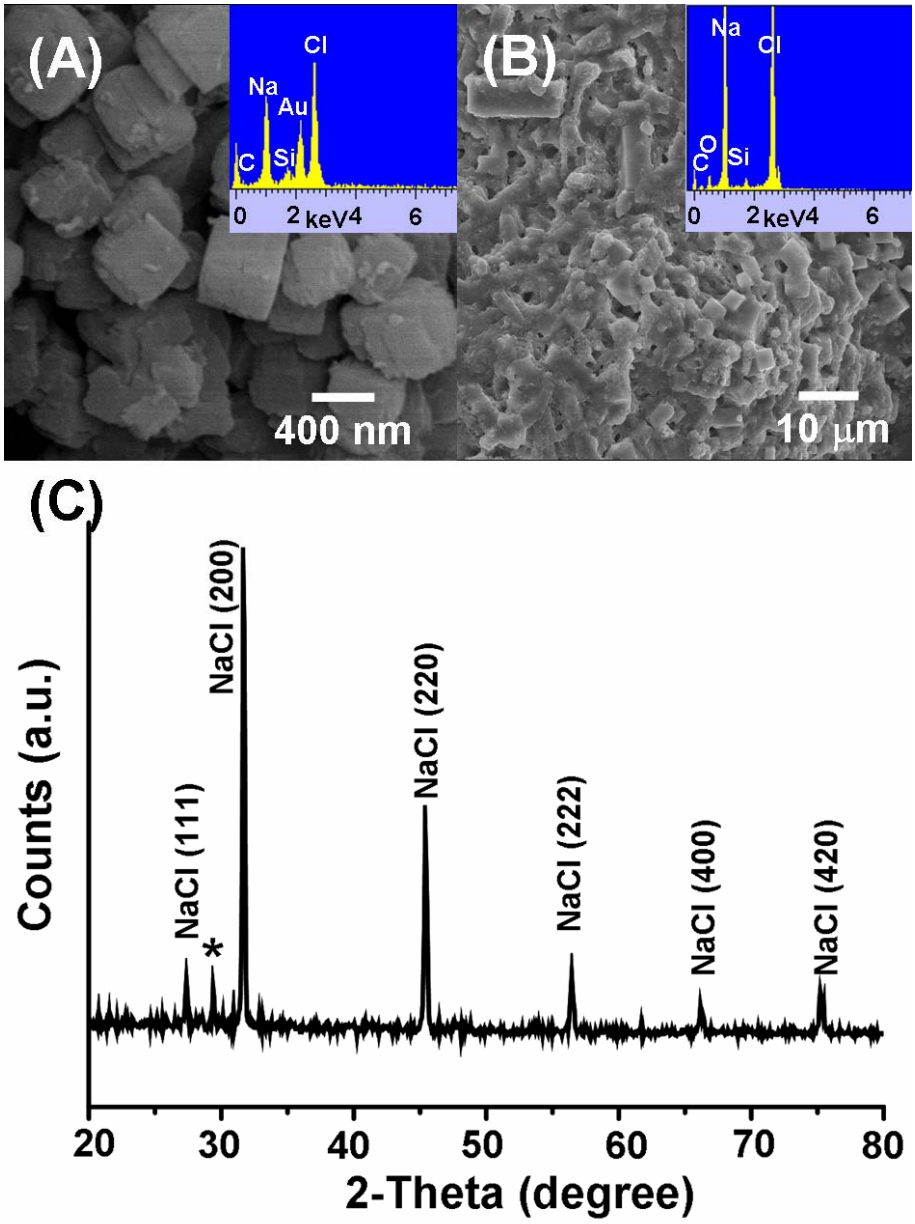


**Figure 2.1** SEM images of (A) **Pre-DD**, and (B) **Pre-MT**. (C) XRD pattern of **Pre-DD**. (Au was sputtered to increase conductivity in EDX, and the peak marked with "*" is from the sample holder in XRD.)

FT-IR spectra of **Pre-DD**, **Pre-MT**, **Pre-MD-673**, and **Pre-MD-723** are shown in Figure 2.2. The absorptions peaks are compared to literature values and listed in Table 2.2.[10,16] The most important feature is the peak near 800 $cm^{-1}$, which can be assigned to Si-C stretching mode. In addition, the absorptions assignable to Si-$CH_2$-Si vibrations are found near 1020 and

1360 $cm^{-1}$ while Si-H stretching is observed near 2100 $cm^{-1}$. The information suggests that polycarbosilane linkage containing Si-$CH_2$-Si units is an important component in the ceramic precursors. This also suggests that Kumada rearrangement is responsible for the structure formation.[17] This is supported by the presence of absorptions from C-H vibrations. Signals originated from moisture absorption in the samples are also observed.

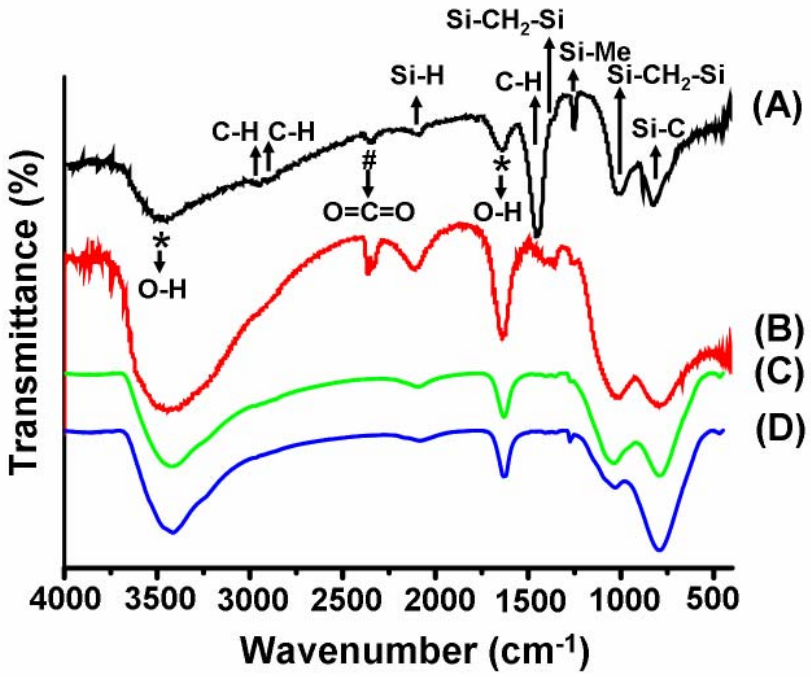


**Figure 2.2** FT-IR spectra of (A) **Pre-DD**, (B) **Pre-MT**,(C) **Pre-MD-673**, and (D) **Pre-MD-723**. (The absorption bands marked with "*" are from absorbed $H_2O$ molecules, and "#"is from atmospheric $CO_2$ molecules.)

$^{29}$Si solid state NMR spectra of **Pre-DD**, **Pre-MT**, **Pre-MD-523**, and **Pre-MD-723** are shown in Figure 2.3. The peaks are observed at -1.2, -17.1, -64.7, and -100.3 ppm. They are assigned to Si atoms in $SiC_4$ (with four Si-C bonds), $SiHC_3$ with one Si-H and three Si-C bonds), $SiHCSi_2$ (with one Si-H, one S-C and two Si-Si bonds), and $SiO_x$ environemnts.[10,18-20] These

results agreed with the FT-IR spectra data discussed above.

**Table 2.2** FT-IR absorptions of the ceramic precursors.[a]

| Vibration Mode | Literature[b] | **Pre-DD** | **Pre-MT** | **Pre-MD-673** | **Pre-MD-723** |
|---|---|---|---|---|---|
| Si-C stretching | 820 | 824 | 794 | 794 | 794 |
| $CH_2$ wagging of Si-$CH_2$-Si bond | 1020 | 1012 | 1024 | 1042 | 1036 |
| Si-Me deformation | 1250 | 1254 | 1260 | 1278 | 1272 |
| $CH_2$ deformation of Si-$CH_2$-Si bond | 1355 | 1369 | 1363 | 1351 | 1357 |
| C-H deformation | 1400 | 1454 | 1411 | 1405 | 1412 |
| Si-H stretching | 2100 | 2096 | 2114 | 2096 | 2084 |
| C-H stretching | 2900 | 2896 | - | - | - |
| C-H stretching | 2950 | 2950 | - | - | - |

[a] All absorption wavenumbers are in $cm^{-1}$. [b] From refs 10 and 15.

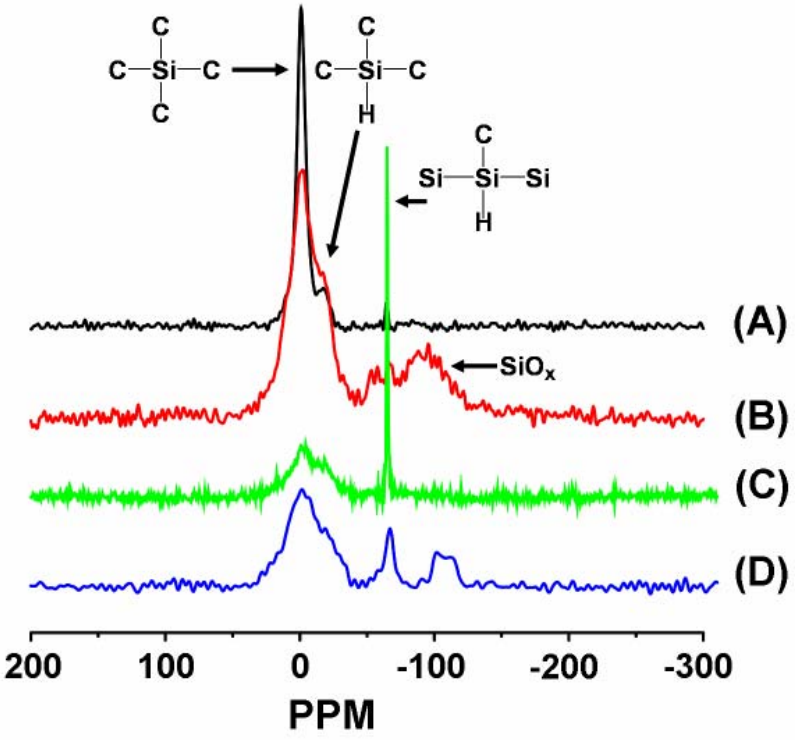


**Figure 2.3** $^{29}$Si-SSNMR spectra of (A) **Pre-DD**, (B) **Pre-MT**, (C) **Pre-MD-523**, and (D) **Pre-MD-723**.

### *2.3.2 SEM Characterizations*

The ceramic precursors discussed above were heated at 1273 K to offer the final products **DD**, **MT**, **MD-523**, **MD-673**, **MD-723**, **PT-573**, and **PT-723.** Colors of the products were either black (**DD**, **PT-573**, and **PT-723**) or yellow (**MT**, **MD-523**, **MD-673**, and **MD-723**). We speculate that the concentration of free carbon affects the color of the products. FT-IR spectra of the samples in Figure 2.4 show a major absorption near 800 $cm^{-1}$. This is assigned to the Si-C stretching of SiC**.**

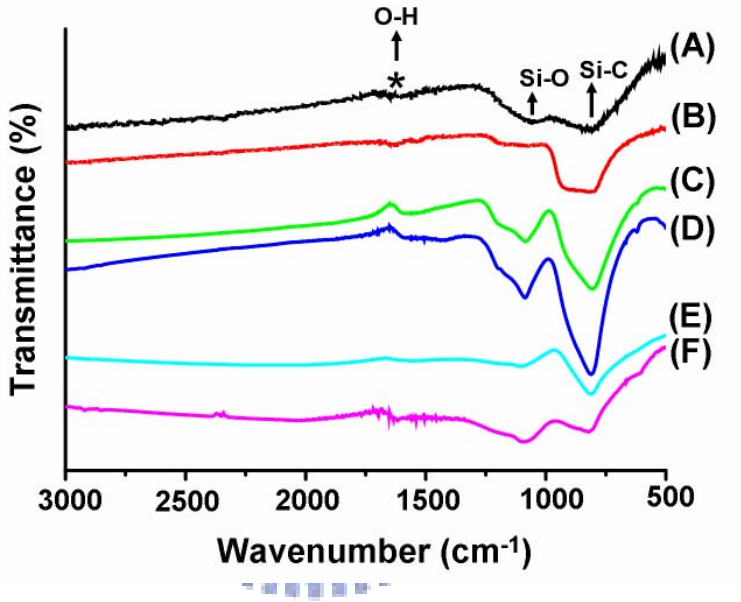


**Figure 2.4** FT-IR spectra of (A) **DD**, (B) **MT**, (C) **MD-673**, (D) **MD-723**, (E) **PT-573**, and (F) **PT-723**. (The Si-O peaks are silica from the quartz boat. The peak marked with "*" is from absorbed $H_2O$.)

SEM images of their morphology are shown in Figures 2.5A – 2.5F, respectively. In general, the products display cubic morphology except **MT** and **MD-523**. Each product will be briefly discussed below. As shown in Figure 2.5A, **DD** contains smooth surface cubes with edge lengths 1 - 2 μm. The powders of **MT**, displayed in Figure 2.5B, are spherical particles

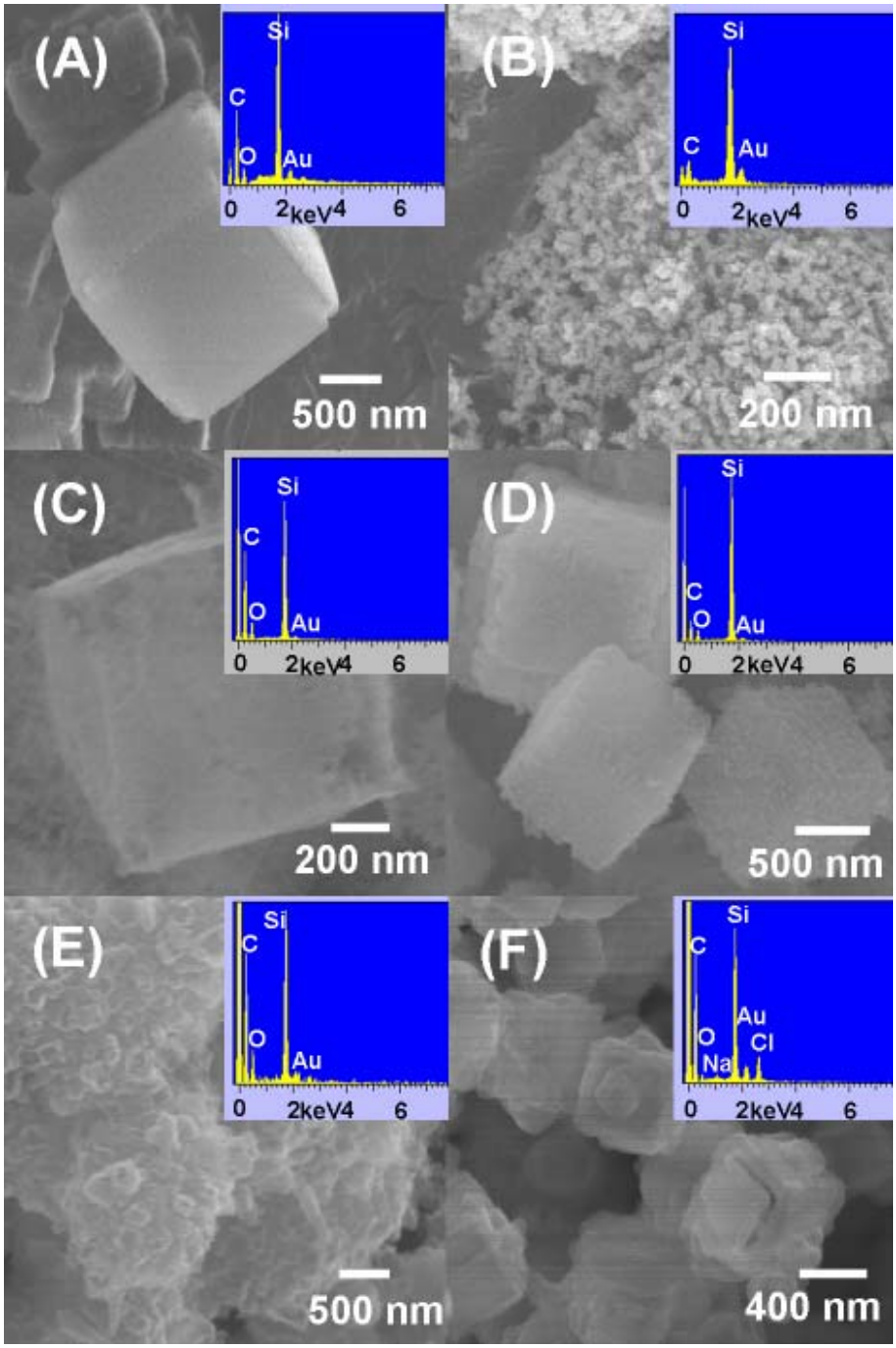


**Figure 2.5** High magnification SEM images of (A) **DD**, (B) **MT**, (C) **MD-673**, (D) **MD-723**, (E) **PT-573**, and (F) **PT-723**. (Au was sputtered to increase conductivity in EDX.)

with diameters of ca. 10 nm. In Figure 2.5C, close examination of the image of **MD-673** reveals that the cube surface is porous. In addition, some spherical particles can be found as a minor component in the corresponding low magnification SEM image in Figure 2.6C.

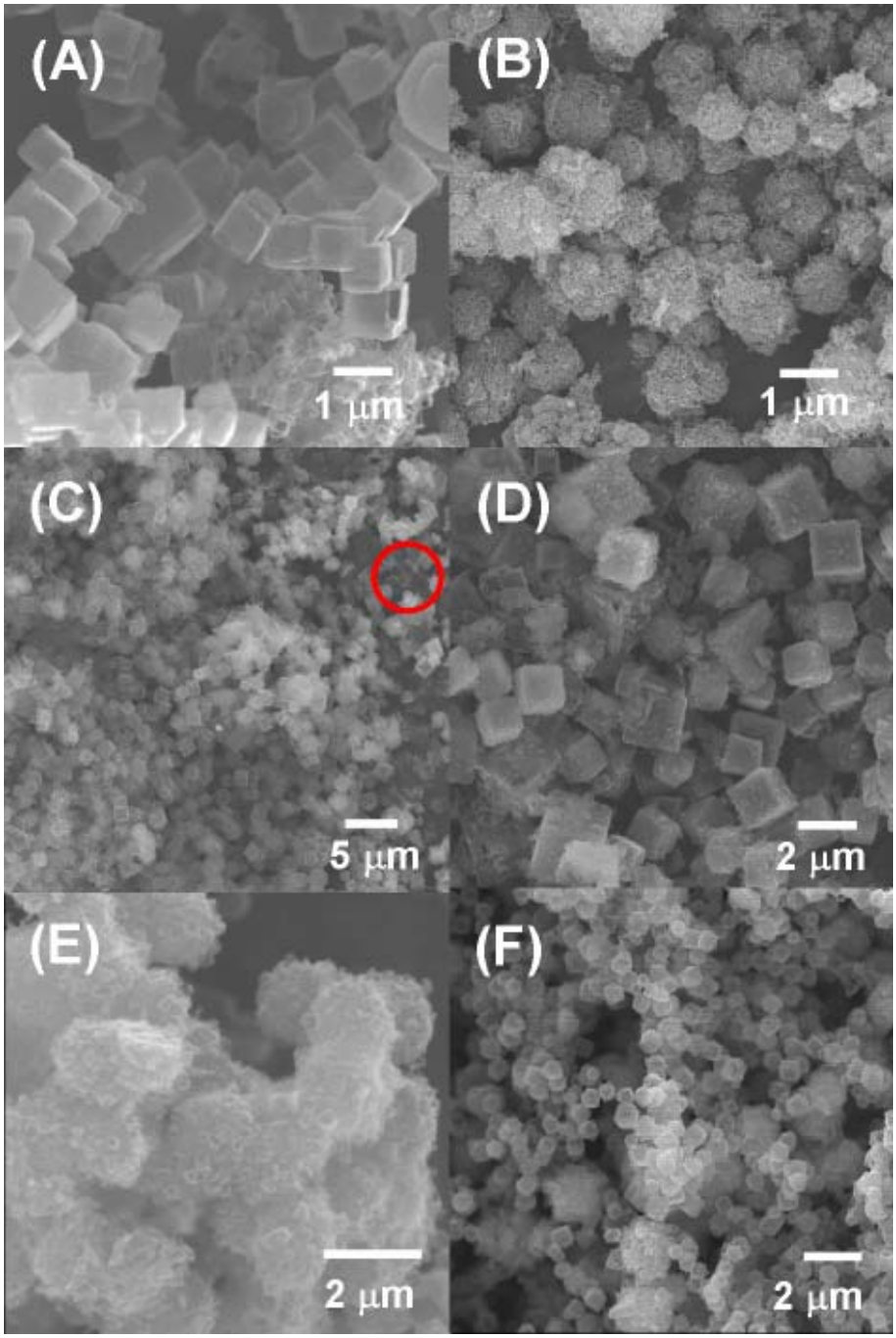


**Figure 2.6** Low magnification SEM images of (A) **DD**, (B) **MT**, (C) **MD-673** (In the red circle, particle aggregates can be seen at high magnification), (D) **MD-723**, (E) **PT-573**, and (F) **PT-723**.

For **MD-723**, it shows a rough surface in Figure 2.5D. In Figure 2.5E, **PT-573** appears to be aggregates of cubic shells with sizes of 100 – 300 nm. Collectively, these aggregates

form cube-like structures, with apparent edge lengths 1.5 – 2 μm. Figure 2.5F shows that **PT-723** is composed of cubic shells (edge lengths 400 - 800 nm) with some spherical particles on the surface.

The corresponding EDX data in the insets suggest that they are composed of Si and C mainly. Signals from residual O, Na and Cl atoms are observed in some cases. The origins of the atoms are attributed to partial oxidation of the precursors in air and the unremoved NaCl byproduct. Both **PT-573** and **PT-723** samples obviously contain more C than the others. Probably due to the pyrolysis of the phenyl groups in the process that generated amorphous and graphitic carbon.[21-23] This could also affect the color of the products.

### *2.3.3 XRD Studies*

XRD patterns of the final products are shown in Figure 2.7. In Figure 2.7A, **DD** shows a broad peak only at 35.7°, which is assigned to β-SiC (111).[24] This suggests that the crystallinity of **DD** is low. **MT** presents in Figure 2.7B distinctive peaks at 2θ 35.6, 60.0 and 71.8. They are assigned to β-SiC (111), (220), and (311) reflections, respectively.[24] The XRD pattern of **MD-673** shown in Figure 2.7C reveals the presence of β-SiC, Si and traces of unremoved NaCl.[24,25,15] The products from the precursors prepared by reacting $MeSiHCl_2$ and Na at 523 - 623 K also showed the patterns of both β-SiC and Si. The origin of Si will be discussed below. **MD-723** shows a comparable pattern in Figure 2.7 with much lower intensities from Si and NaCl. Figure 2.7E suggests that **PT-573** contains β-SiC as the major crystalline phase.[24] A broad peak centred at 23.5° (d = 0.38 nm) was also observed and assigned to the reflection of graphite (002).[26] In Fig. 2.7F, peaks of β-SiC and graphite are also observed for **PT-723**.[24,26] Apparently, the formation of graphite is the result of the presence of the phenyl group in the organochlorosilane.

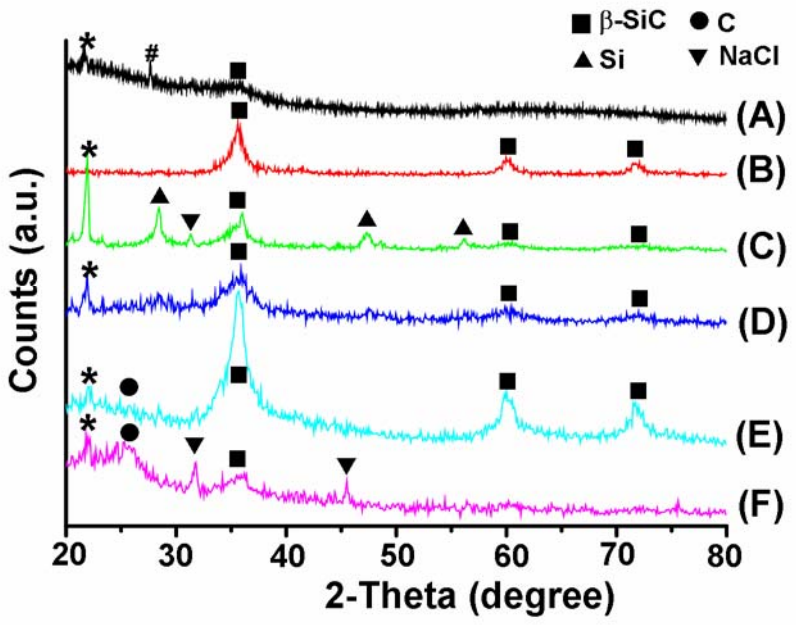


**Figure 2.7** XRD patterns of (A) **DD**, (B) **MT**, (C) **MD-673**, (D) **MD-723**, (E) **PT-573**, and (F) **PT-723**. (The peaks marked with "*" are silica from the quartz boat while the one with "#" is not identified.).

### *2.3.4 TEM Characterizations*

Figure 2.8 shows the TEM images of the products. Figure 2.8A is the image of **DD**. It reveals that **DD** contains cubic particles with edge lengths 0.5 – 1 μm and hollow shell structures. The image of **MT** in Figure 2.8B shows the presence of spherical nanoparticles. An enlarged view suggested that the averaged diameter was about 10 nm.[13] The images of **MD-673** and **MD-723** are shown in Figure 2.8C and 2.6D, respectively. Both show that the products are cubic hollow shells. The surfaces are relatively uneven. For **MD-673**, there are some protruded hollow shells with varying shapes. While for **MD-723**, an apparent layer of a channel structure exists below the cube shell. The ED patterns are shown in the insets of Figure 2.8. All reveal patterns with three distinctive rings, suggesting that they are polycrystalline. Starting from the most inside ring, these rings are

assigned to the reflections from (111), (220), and (311) planes of β-SiC, with an estimated lattice parameter a = 0.44 nm.[24]

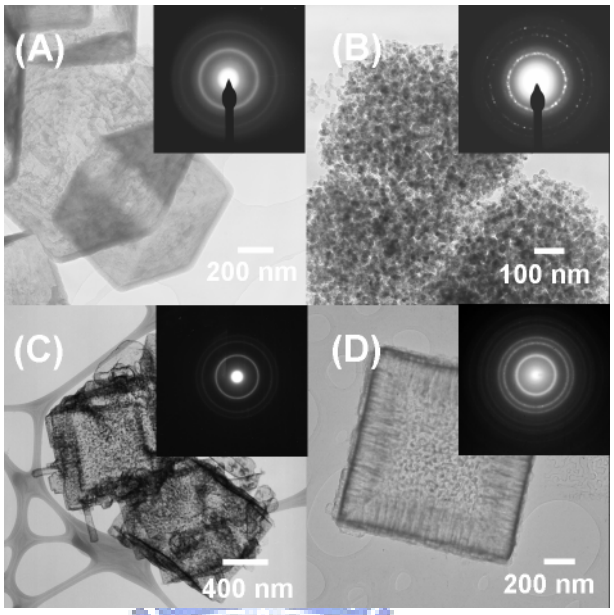


**Figure 2.8** TEM images of (A) **DD**, (B) **MT**, (C) **MD-673**, (D) **MD-723**.

For **MD-673**, another TEM image showed in Figure 2.9A that it also contained nanoparticles with diameters 5 - 10 nm. The ED pattern in Figure 2.9B showed six rings assignable to Si and β-SiC.[24,25] A high resolution TEM image in Figure 2.9B also presented the coexistence of two different lattice spacing values, 0.310 nm and 0.254 nm, corresponding to Si (111) and β-SiC (111) planes of the nanocrystals, respectively.[24,25] This agrees with the XRD pattern of **MD-673** in Figure 2.7. The degree of crystallization suggested by the ED patterns is comparable to that shown in the XRD patterns.

The TEM image of **PT-723** also showed cube-like hollow particles with an averaged shell thickness of 40 nm in Fig. 2.10A. In addition, some round-shaped hollow particles adhered to the surfaces of the cube-like particles. This agrees with the SEM image in Figure 2.5F. The ED pattern of **PT-723** in Figure 2.10A (inset), showing a combination of crescent-shaped and weak diffused rings, indicated that it contained less-ordered graphite and β-SiC. A HRTEM image of a particle edge revealed some fringes spaced at 0.35 nm apart in

Figure 2.10B. This value is slightly larger than the lattice spacing of graphite (002), 0.340 nm.[26]

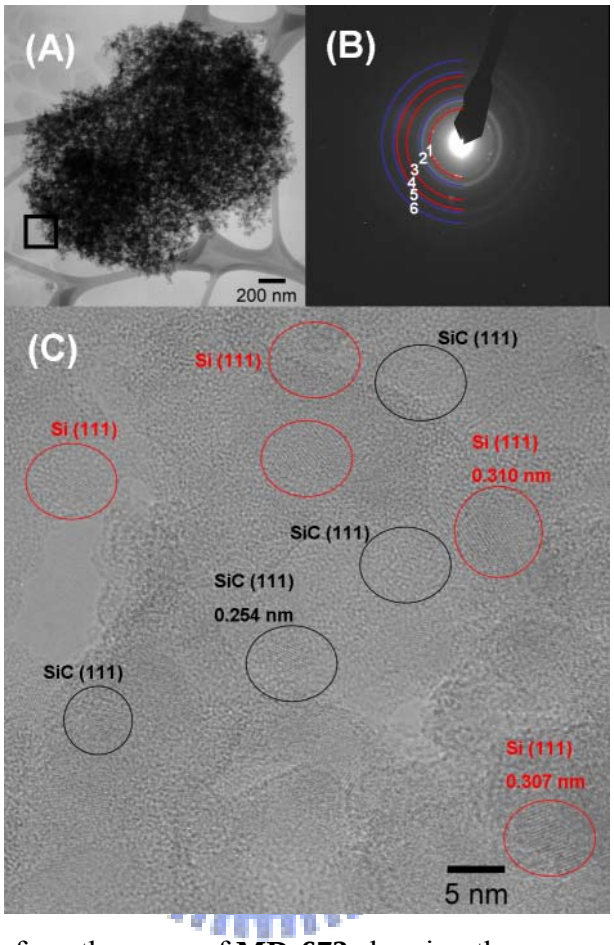


**Figure 2.9** TEM view of another area of **MD-673** showing the presence of nanoparticles. (A) Low magnification TEM, (B) ED, and (C) High-resolution TEM images.

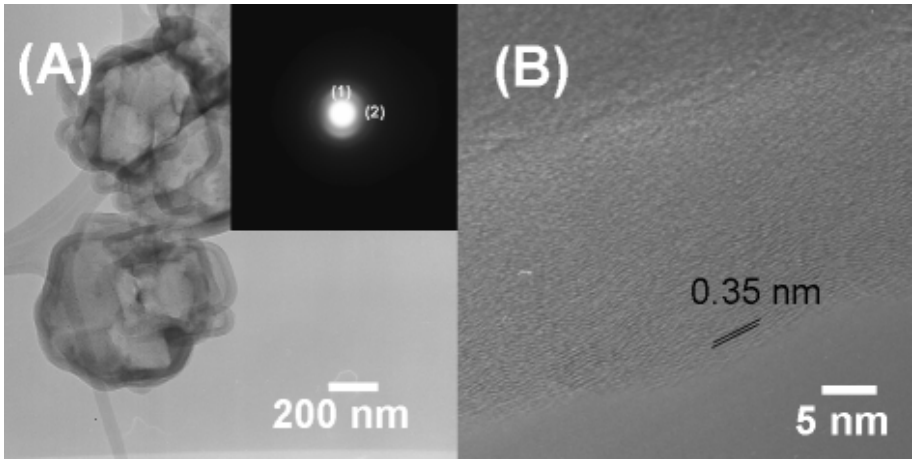


**Figure 2.10** (A) TEM and ED (inset) images of **PT-723** and (B) HRTEM image of **PT-723**.

## 2.4 Discussion

As suggested in Scheme 2.1, the vapor phase organochlorosilanes react with liquid phase sodium to form phase segregated SiC precursors and NaCl solids in the first step. In the original Yajima process, polysilane $(Me_2Si)_n$ was synthesized first in a xylene solution at 373 K and then converted into polycarbosilane $(MeSiHCH_2)_n$ at 723 K. In this study, we prepared β-SiC from a solvent-free condition at elevated temperatures employing the organochlorosilane vapors to react with the Na liquid directly. From the characterization of the ceramic precursors, we conclude that the overall syntheses are parallels to the Yajima process. On the other hand, the reaction variables, including silane sources and reaction temperatures, do show great influences on the β-SiC products. In addition, their final morphology, showing cubic structures in many cases, appears to be shaped cooperatively by the precursor and the NaCl byproduct, which acted as templates generated in situ.

In addition to the characterizations discussed above, a difference between the ceramic precursors **Pre-DD** and **Pre- MT** is demonstrated by TGA studies were shown in Figure 2.11. The TGA of **Pre-DD** showed significant weight loss above 873 K. The loss reached 40% at 1023 K. On the other hand, **Pre-MT** was more stable up to 1023 K. It showed only 8% weight loss at 1073 K. Based on these data and the other analyses, we propose that **Pre-DD** is likely to be a linear polycarbosilane with a general formula (A) shown in Scheme 2.2 while **Pre-MT** is a cross-linked polycarbosilane (B) in Scheme 2.2.[27] Apparently, **Pre-DD** is more flexible than **Pre-MT**. The consequence is that **Pre-DD** could wrap the NaCl byproduct crystals easily to form the shell layers. After the inner NaCl cores are removed under vacuum at 1273 K, **Pre-DD** converts into **DD**, the β-SiC particles with cubic shell structures. The more rigid **Pre-MT** could not fold easily so it separates from NaCl into an independent solid. After the NaCl byproduct is evaporated under vacuum at 1273 K, **Pre-MT** converts into **MT**, the spherical nanoparticles of β-SiC.

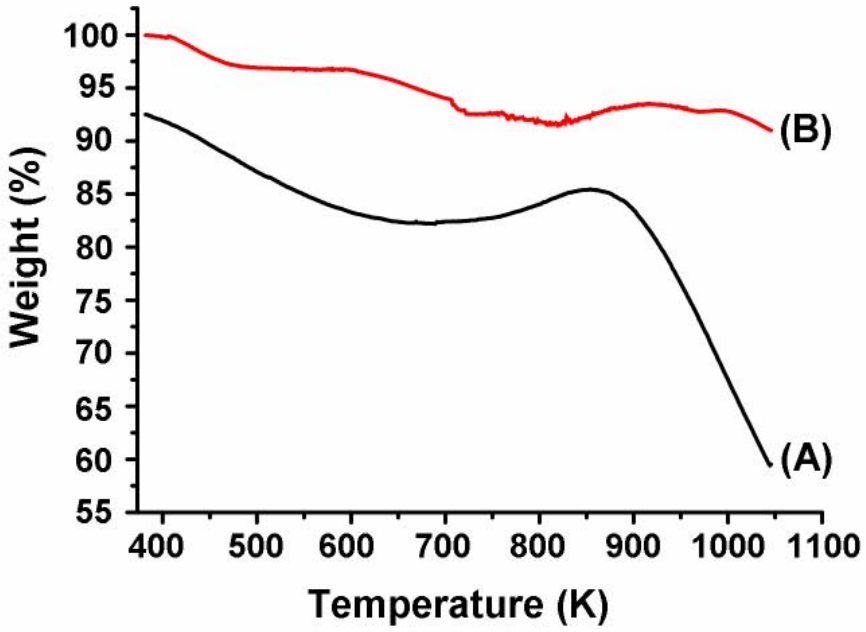


**Figure 2.11** TGA of (A) **Pre-DD** and (B) **Pre-MT**.

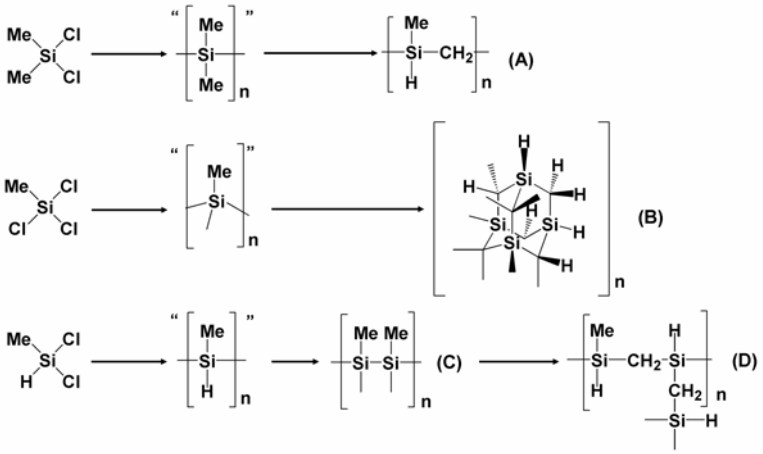


**Scheme 2.2** Proposed conversions of methylchlorosilanes to ceramic precursors.

The effects of reaction temperature on the precursors prepared from $CH_3SiHCl_2$ have been shown in the IR and the SSNMR data discussed above. They suggest that in addition to -Si-$CH_2$- linkages of polycarbosilanes, **Pre-MD-523** contained a significant portion of Si-Si bonds of polysilanes. In contrast, the peak was less significant in the SSNMR **of Pre-MD-723**. In addition, an UV-visible spectrum of **Pre-MD-523** presented an absorption at 280 nm in

Figure 2.12A. This is attributed the σ-σ* transition of organopolysilanes.[20,28,29] **Pre-MD-723** did not show any absorption peak from this transition in Figure 2.12B.. In literature, Seyferth reported that preceramic polymer $(MeSiH)_x(MeSi)_{1-x}$ was produced by reacting $MeSiHCl_2$ with Na in a solution.[12] In addition, Matyjaszewski and co-workers showed that cyclic organopolysilane polymers were formed in the reactions between organochlorosilanes and Na or K.[20] Thus, we propose that **Pre-MD-523** contains rigid polysilanes and flexible polycarbosilanes, (C) and (D) shown in Scheme 2.2, respectively. After the removal of NaCl by evaporation at 1273 K, the two portions probably react and transform independently into cubic shells of β-SiC and nanoparticles mixed with β-SiC and Si, correspondingly. On the other hand, for precursors prepared from $MeSiHCl_2$ at higher temperatures, more (D) is expected to be converted from (C), as shown in Scheme 2.2. This is supported by that **Pre-MD-723** is composed mainly of polycarbosilanes (D). With less rigid organopolysilane polymers in presence, the precursor can cover the surface of NaCl and converts to cubic particles of β-SiC shells mostly.

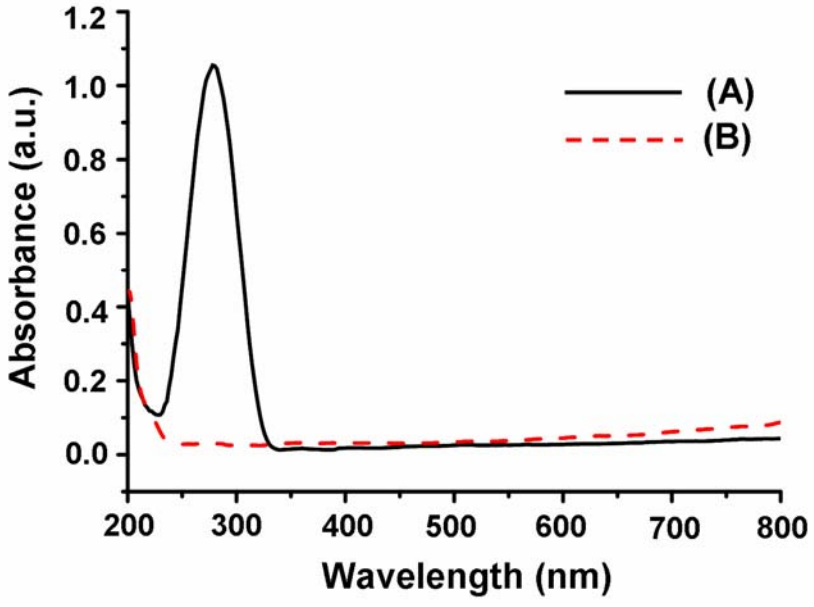


**Figure 2.12** UV spectra of (A) **Pre-MD-523** and (B) **Pre-MD-723**.

When $PhSiCl_3$ was employed as the precursor to form β-SiC, appreciable amount of graphitic products was formed in **PT-573** and **PT-723**. In literature, formation and incorporation of carbon in β-SiC prepared by Yajima type reactions employing phenylchlorosilanes have been reported.[21-23] The carbon-rich precursors appears to be flexible enough to cover the surface of the byproduct NaCl. It is known that probably due to its flexibility, carbon may be shaped into structures with different morphology in related vapour-solid reaction growths (VSRG).[30] After the cubic NaCl core is removed by evaporation, the cube-like particles containing graphite carbon/β-SiC can be formed.

## 2.5 Conclusions

In this study, we have synthesized β-SiC cubic shells and spherical nanoparticles by processing the ceramic precursors formed from the reactions between vapors of organochlorosilanes, $Me_2SiCl_2$, $MeSiCl_3$, $MeSiHCl_2$, and $PhSiCl_3$, and liquid Na. Nature of the silane precursors and the reaction temperatures affect the composition and nanostructure of the ceramic precursors as well as their affinity to the NaCl byproduct, the template generated in situ. Then, all these factors work together to influence the final composition and morphology of the synthesized β-SiC. We found that when precursors with flexible linear polycarbosilanes are produced, they would cover the cubic NaCl surface. Consequently, after the NaCl templates are removed, the final ceramic products are shaped into hollow cubic shells. When rigid precursors, such as polysilanes and cross-linked polycarbosilanes, are produced, they phase segregate from NaCl and are transformed into nanoparticles without special morphology as the final products. The reaction temperature affects the extent of the reaction progress. Together with other processing factors, the final compositions can be altered. When a polysilane precursor is produced, it is converted into Si-rich nanoparticles. On the other hand, when carbon-rich chlorosilanes are used, the final products contain, in addition to β-SiC, a high concentration of carbon byproduct. In conclusion, we demonstrate

again that reactions between vapor and condensed phase reactants can produce phase separated products with unique morphology by templating each other in situ.[30] We expect that β-SiC with other special morphology could be synthesized using this strategy in the future.

## 2.6 References


(1) (a) Niihara, K. *Ceram. Bull.* **1984**, *63*,1160. (b) Narushima, T.; Goto, T.; Lguchi, Y.; Hirai, T. *J. Am. Ceram. Soc.* **1990**, *73*, 3580.

(2) Spetz, A. L.; Baranzani, A.; Tobias, P.; Lundström, I. *Phys. Stat. Sol. (a)* **1997**, *162*, 493.

(3) Biernacki, J. J.; Wotzak, G. P. *J. Am. Ceram. Soc.* **1989**, *72*, 122.

(4) Hatakeyama, F.; Kanzaki, S. *J. Am. Ceram. Soc.* **1990**, *73*, 2107.

(5) Seog, I. S.; Kim, C. H. *J. Mater. Sci.* **1993**, *28*, 3227.

(6) Kamlag, Y.; Goossens, A.;Colbeck, I.; Schoonman, J. *Chem. Vapor. Deposition* **2003**, *9*, 125.

(7) Chiu, H.-T.; Huang, S.-C. *J. Mater. Sci. Lett.* **1993**, *12*, 537.

(8) Pitcher, M. W.; Joray, S. J.; Bianconi, P. A. *Adv. Mater.* **2004**, *16*, 706.

(9) (a) Yajima, S.; Hayashi, J.; Omori, M. *Chem. Lett.* **1975**, 931. (b) Yajima, S. Okamura, K.; Hayashi, J. *J. Chem. Lett.* **1975**, 1209. (c) Yajima, S.; Omori, M.; Hayashi, J.; Okamura, K.; Matsuzawa, T.; Law, C. *Chem. Lett.* **1976**, 551. (d) Yajima, S.; Hayashi, J.; Omori, M.; Okamura, K. *Nature* **1976**, *261*, 683.

(10) (a) Yajima, S.; Hayasht, J.; Hasegawa, Y.; Iimura, M. *J. Mater. Sci.* **1978**, *13*, 2569. (b) Hasegawa, Y.; Iimura, M.; Yajima, S. *J. Mater. Sci.* **1980**, *15,* 720. (c) Hasegawa, Y.; Okamura, K. *J. Mater. Sci.* **1983**, *18*, 3633.

(11) Bianconi, P. A.; Weidman, T. W. *J. Am. Chem. Soc.* **1988**, *110*, 2342.

(12) Seyferth, D.; Wood, T. G.; Tracy, H. J.; Robison, J. I. *J. Am. Ceram. Soc.* **1992**, *75*, 1300.

(13) Wang, C.-H.; Chang, Y.-H.; Yen, M.-Y.; Peng, C.-W.; Lee, C.-Y.; Chiu, H.-T. *Adv. Mater.* **2005**, *17*, 419.

(14) Wang, L.-S.; Lee, C.-Y.; Chiu, H.-T. *Chem.Comm.* **2003**, 1964.

(15) Joint Committee for Powder Diffraction (JCPDS) File No. 05-0628. International Center for Diffraction Data, 2002.

(16) Ishikawa, T.; Shibuya, M.; Yamamura, T. *J. Mater. Sci.* **1990**, *25*, 2809.

(17) (a) Kumada, M.; Hosoni, A.; Sakurai, H. *J. Chem. Soc., Chem. Commun.* **1968**, 930. (b) Kumada, M.; Hosoni, A.; Sakurai, H. *J. Chem. Soc.,Chem. Commun*. **1969**, 4. (c) Kumada, M. *J. Organomet. Chem.* **1975**, *100*, 127.

(18) Iseki, T.; Narisawa, M.; Katase, Y.; Oka, K.; Dohmaru, T.; Okamura, K. *Chem. Mater.* **2001**, *13*, 4163.

(19) Czosnek, C.; Ratuszek, W.; Janik, J. F.; Olejniczak, Z. *Fuel Process. Technol.* **2002**, *79*, 199.

(20) Matyjaszewski, K.; Greszta, D.; Hrkach, J. S.; Kim, H. K. *Macromolecules* **1995**, *28*, 59.

(21) Andrianov, K. A.; Kotov, V. M. *J. Organometal. Chem.* **1967**, *7*, 211.

(22) Shieh, Y.-T.; Sawan, S. P. *J. Appl. Polym. Sci.* **1995**, *58*, 2013.

(23) Montgomery, F. C.; Streckert, H. H. *Polym. Prepr.* **1981**, *28*, 258.

(24) Joint Committee for Powder Diffraction (JCPDS) File No. 29-1129. International Center for Diffraction Data, 2002.

(25) Joint Committee for Powder Diffraction (JCPDS) File No. 75-0589. International Center for Diffraction Data, 2002.

(26) Joint Committee for Powder Diffraction (JCPDS) File No. 75-1621. International Center for Diffraction Data, 2002.

(27) Seyferth, D.; Lang, H. *Organometallics* **1991**, *10*, 551.

(28) Bianconi, P. A.; Schilling, F. C.; Weidman, T. W. *Macromolecules* **1989**, *22*, 1697.

(29) Watanabe, A.; Nanjo, M.; Sunaga, T.; Sekiguchi, A. *J. Phys. Chem, A.* **2001**, *105*, 6436.

(30) (a) Huang, C.-H.; Chang, Y.-H.; Lee, C.-Y.; Chiu, H.-T. *Langmuir* **2006**, *22*, 10. (b) Huang, C.-H.; Chang, Y.-H.; Lin, H.-K.; Peng, C.-H.; Chung, W.-S.; Lee, C.-Y.; Chiu, H.-T. *J. Phys. Chem. C.* **2007**, *111*, 4138. (c) Huang, C.-H.; Chang, Y.-H.; Wang, H.-W.; Cheng, S.; Lee, C.-Y.; Chiu, H.-T. *J. Phys. Chem. B*, **2006**, *110*, 11818.

# Chapter 3

# Growth of Polycrystalline Tubular Silicon Carbide - Yajima-Type Reaction at the Vapor-Solid Interface

## 3.1 Introduction

Silicon carbide is an important semiconductor material for high temperature, high power and high frequency applications in demanding environments.[1] Therefore, fabrication of silicon carbide into nanometer scale devices has received considerable attention. To date, many kinds of silicon carbide nanostructures have been successfully fabricated, including nanoboxes, hollow nanospheres, nanorods, nanowires, and nanocables.[2-5] But, there were only limited reports on the synthesis of tubular silicon carbide nanostructure.[6-8] Drawbacks of these approaches include low-yields, low crystallinity, and difficulty to remove templates. Here, we demonstrate that using simple vapor-solid reaction growth (VSRG) methodology,[9-11] high yield synthesis of large area polycrystalline tubular SiC on Si substrates can be achieved by employing methyldichlorosilane, $MeSiHCl_2$, to react with Ca thin films on Si(100) wafers at relatively low temperatures. The reaction is an improved Yajima-type reaction carried out in a solvent-free condition.[12] One-dimensional β-SiC fibers prepared from the Yajima process can be used for many advanced structural applications.[13] In this study, potential application of the tubular SiC as an efficient field emitting material will be explored.[14-15]

## 3.2 Experimental Section

A hot-wall reactor composed of a Lindberg HTF55122A tube furnace and a 27 mm diameter quartz tube was used. In a typical reaction, Ca powders (Alfa Aesar 99.5%, 0.30 g, 7.5 mmole) in a 10 cm quartz boat were placed at a distance 5 cm upstream away from the

center of the reactor. Another quartz boat loaded with Si(100) substrates was placed at 25 cm away from the center, which was located just outside the furnace and at 430 K. Evaporation of Ca was performed at 973 K under vacuum for 1 h so that Ca thin films deposited on the Si substrates. Then, under 1 atm of Ar, the Ca coated Si substrates were pushed into the reactor center. Under the assistance of a constant flow of Ar (10 sccm), $MeSiHCl_2$ at 255 K was evaporated into the reactor. The reaction was carried out at 773 - 923 K for 12 h to generate a precursor coating. Finally, the precursor coating was heated at 1273 K for 1 h under vacuum to offer samples of a layer of yellow thin film on Si.

Scanning electron microscopic (SEM) and energy dispersive X-ray (EDX) spectroscopic data were collected using a JEOL JSM-6330F at 15 kV. Transmission electron microscopic (TEM) and electron diffraction (ED) images were obtained on a JEOL JEM-2010 at 200 kV. High resolution TEM (HRTEM) images were acquired on a JEOL JEM-4000EX at 400 kV. X-ray diffraction (XRD) studies were carried out using a BRUKER AXS D8 ADVANCE diffractometer using Cu Kα1 radiation. Fourier transform infrared (FT-IR) spectra were carried out using a Perkin Elmer Spectrum One. Thermal gravimetric analysis (TGA) was carried out on a Perkin Elmer Diamond TGA.

Field emission measurements were performed in a vacuum chamber at a pressure of $1.05\times10^{-3}$ Pa at room temperature. A 1 mm diameter spherical-shaped stainless-steel probe was used as the anode. Field emission characteristics of the samples were measured with a Keithley 237 (max output voltage 1100 V, current 10 mA). One sample of tubular SiC material on Si(100), which was grown at 873 K followed by heat treatment at 1273 K, was measured at an anode-sample distance of 65 μm while the applied field voltage was raised from zero to 940 V. Another sample of tubular SiC material on Si(100), which was grown at 923 K followed by heat treatment at 1273 K, was measured with at an anode-sample distance of 75 μm while the applied field voltage was raised from zero to 480 V. We define the turn-on field ($E_{to}$) and the threshold field ($E_{th}$) as the electric fields required to produce a

current density of 10 $\mu Acm^{-2}$ and 10 $mAcm^{-2}$, respectively.

### 3.3 Results and Discussion

The reaction was carried out in a horizontal hot-wall quartz tube reactor. Growth of a fresh surface Ca thin film with a thickness of ca. 5 μm on a Si(100) wafer at 430 K was achieved via a physical vapor deposition (PVD) process by evaporating Ca at 973 K. The Ca thin film, as characterized by SEM and XRD in Figure 3.1, was smooth and free from other crystalline phases, such as CaSi, $CaSi_2$, and CaO. At the deposition temperature, interdiffusion of elemental Ca and Si atoms to form $CaSi_x$ compounds was reported to be insignificant.[16]

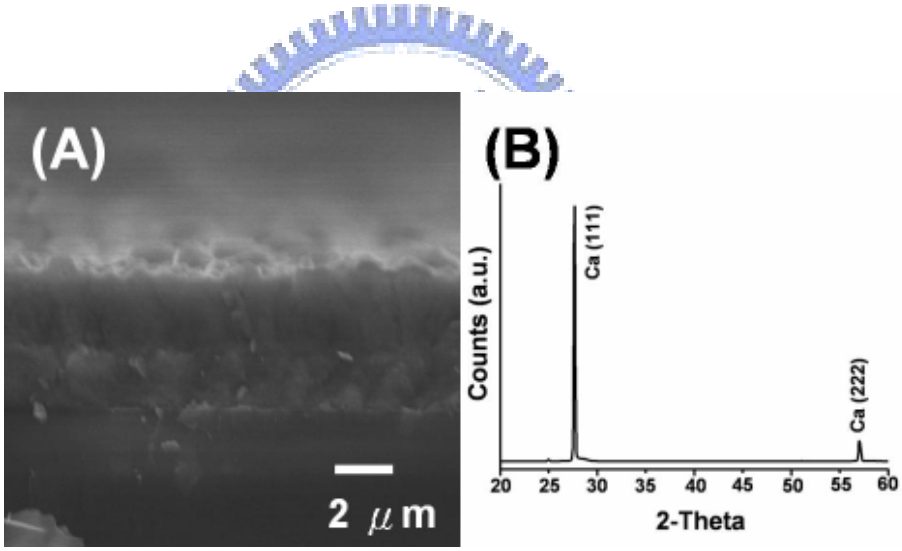


**Figure 3.1** (A) Cross sectional SEM image, and (B) XRD pattern of a calcium thin film deposited on a Si substrate. The XRD pattern can be assigned to JCPDF 23-0423.

Then, the Ca thin film was reacted with vaporized $MeSiHCl_2$ at 773 – 923 K to form a solid precursor layer on Si. The layer was proposed to be $CaCl_2$ encapsulated inside a Yajima-type preceramic polycarbosilane precursor, $SiC_xH_y$.[12] The material was further processed at 1273 K under vacuum to thermally convert it in to the final product. In the process, $CaCl_2$ was removed by evaporation as well. A yellow thin film, covering the Si substrate completely, was

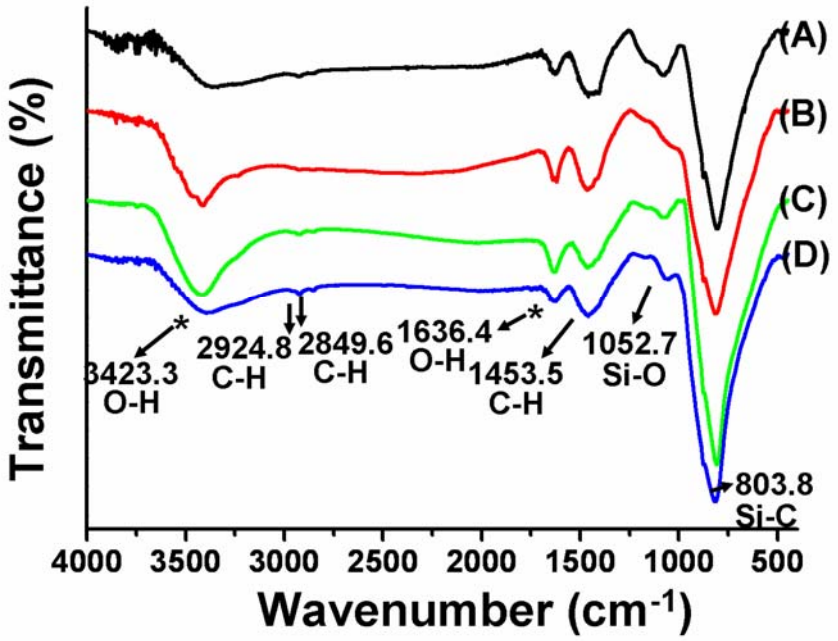


**Figure 3.2** FT-IR spectra of samples grown at (A) 773 K, (B) 823 K, (C) 873 K, and (D) 923 K followed by heat treatment at 1273 K. The absorption bands marked with "*" are from absorbed $H_2O$ molecules.

collected. For all thin films, the FT-IR data in Figure 3.2 show major absorptions from Si-C bonds near 800 $cm^{-1}$ and minor ones from residual C-H bonds near 2925, 2850 and 1450 $cm^{-1}$.[12] XRD data displayed a broad peak at $2\theta = 35.7^{o}$ from SiC (111) reflection (JCPDS 29-1129)[17] and sharp peaks from Si reflections (JCPDS 75-0589) as shown in Figure 3.3.[18] The samples were also characterized by using SEM, EDX, TEM, and selected area ED (SAED). With some variations in growth rates, sizes and crystallinity, i.e. they all increased with the increasing temperature of reaction, the products showed comparable morphology, composition, and microstructures. Typical observations will be discussed below.

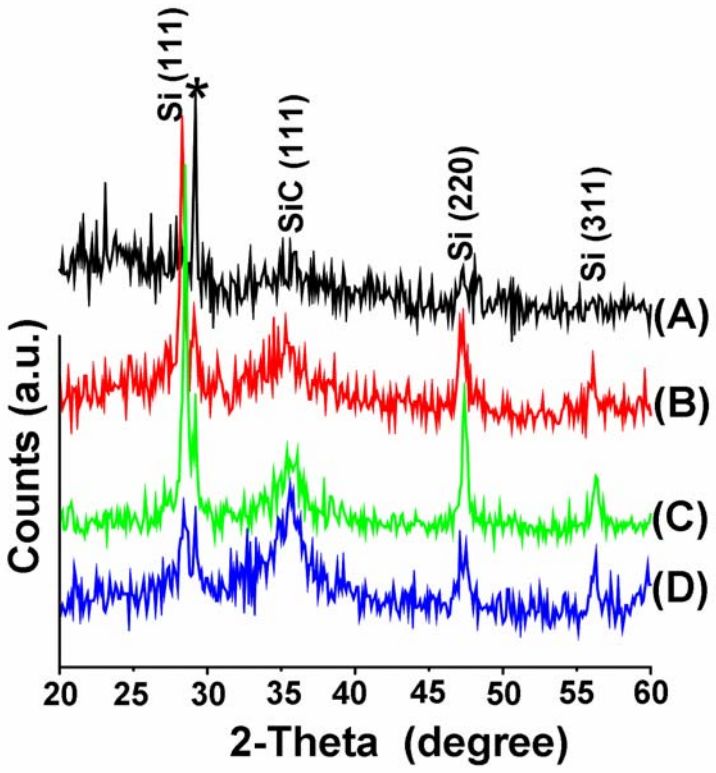


**Figure 3.3** XRD of samples grown at (A) 773 K, (B) 823 K, (C) 873 K, and (D) 923 K followed by heat treatment at 1273 K. All samples were removed from the Si substrates except the sample in C. The peak marked with "*" is from the sample holder.

### *3.3.1 SEM and XRD Characterizations*

A low-magnification SEM image of the yellow thin film grown at 823 K on Si followed by heat treatment at 1273 K is shown in Figure 3.4A. The image displays numerous one-dimensional nanostructures with tens of micrometers long. High-magnification SEM images, such as the one in Figure 3.4B, suggest that the material has an apparently open-end tubular structure with a diameter of 100 - 200 nm. An EDX spectrum shown in Figure 3.4B (inset) indicates that the tubular material contains Si, C, and traces of Ca and Cl. An SEM image of the thin film/substrate cross-section in Figure 3.4C reveals that the tubular nanomaterial layer has a thickness up to several tens micrometers. In addition, an interlayer

with a thickness of ca. 9 μm is observed between the tubular material layer and the Si substrate. An EDX spectrum of the interlayer, as shown in the inset of Figure 3.4C, indicates that the material contains more Si than the tubular material layer does. Figure 3.4D shows the XRD pattern of the deposited layer after being removed from the Si substrate. The SiC (111) reflection and the Si reflections are observed.[18] By using the Scherrer equation, the crystallite sizes of SiC and Si are estimated to be 3 nm and 18 nm, respectively. Since only reflections of electrons from SiC were observed for the tube in the ED studies (to be discussed below), we suggest that the Si pattern in XRD was not from the tubular material layer. In stead, it might originate from the interlayer because it was Si rich as shown in the EDX result. One possible origin of the Si crystals was from residual fragments of the Si substrate. As the product layers were detached, some Si fragments might attach to the product and were removed together. Another possibility was that during the reaction between $MeSiHCl_2$ and Ca at 823 K, a $CaSi_x$ layer was also produced between the Ca thin film and the Si substrate by interdiffusion of the corresponding elements.[19] As the reaction progressed, the $CaSi_x$ layer might react with $MeSiHCl_2$ to generate the interlayer composed of SiC and Si. On the other hand, presence of Si as a minor component in the tubular product layer was observed for samples deposited above 873 K (see below in TEM and TGA Studies). Even though the image in Figure 3.4B suggests that the one-dimensional material has an open-end tubular structure, another SEM image in Figure 3.4E shows a sample with a lot of tubes with broken ends. An enlarged view in Figure 3.4F displays a ruptured tip of a one-dimensional structure.

### *3.3.2 TEM Studies*

Figure 3.5A presents the TEM image of the sample grown at 823 K followed by heat treatment at 1273 K. It confirms that it is one-dimensional and has an apparent open-end tubular structure with a diameter of ca. 100 nm and a wall thickness of 10 - 20 nm. SAED reveals a slightly diffused pattern with three distinctive rings in Figure 3.5B suggesting that

the sample is polycrystalline with crystallite sizes smaller than 4 nm. Starting from the most inside ring, these rings are assigned to the reflections from SiC(111), SiC(220), and SiC(311)

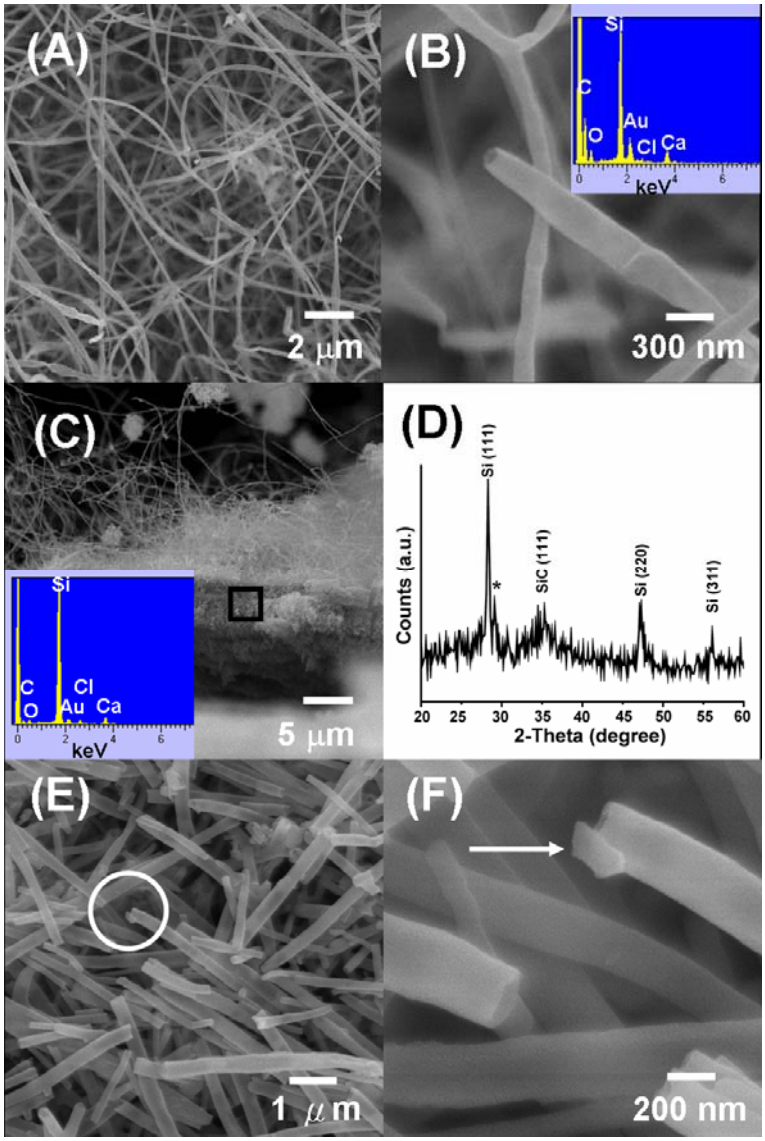


**Figure 3.4** Characterization of a sample grown on Si wafer at 823 K followed by heat treatment at 1273 K. SEM studies: (A) low magnification surface image, (B) high magnification image of a tube end, and EDX (inset. Au was sputtered to increase conductivity), (C) cross-sectional image of the deposited layers on Si, and EDX (inset, from the squared area. Au was sputtered to increase conductivity), (D) XRD pattern. The peak marked with "*" is from the sample holder. (E) Low magnification image of tubes with ruptured ends and (F) high magnification of the circled area in (E) showing a ruptured end of a sample grown on Si wafer at 873 K followed by heat treatment at 1273 K.

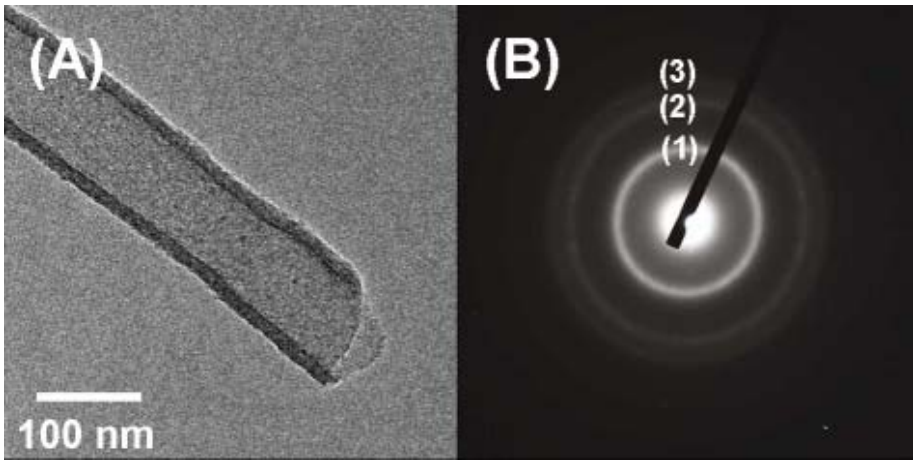


**Figure 3.5** TEM studies of a sample grown at 823 K followed by heat treatment at 1273 K. (A) Low magnification image, and (B) SAED.

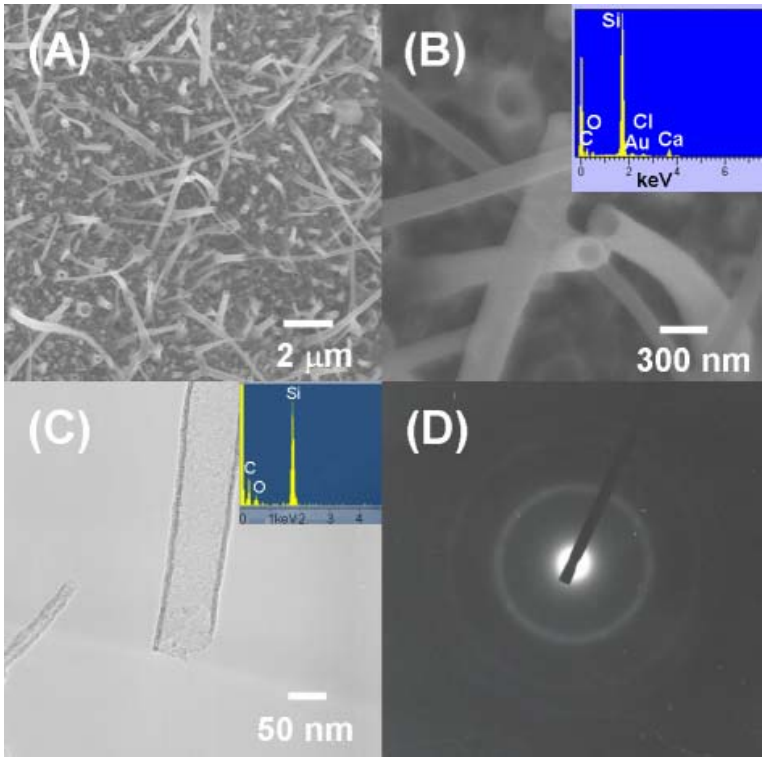


**Figure 3.6** Characterization of a sample grown on Si wafer at 773 K followed by heat treatment at 1273 K. (A) Low magnification SEM image, (B) high magnification image of tube ends, and EDX (inset), (C) TEM image and EDX (inset), and (D) SAED, the polycrystalline diffraction rings are assigned to β-SiC.

planes. They can be assigned to cubic β-SiC with an estimated lattice parameter a = 0.44 nm.[17] No reflections from crystallites of Si and Ca containing solids can be seen. The observations are in good agreement with the XRD data.

For the sample grown at 773 K followed by heat treatment at 1273 K, the TEM and ED data were comparable, showing an apparent open-end polycrystalline SiC tube with a diameter of ca. 80 nm and a wall thickness of 5 - 10 nm as shown in Figure 3.6.

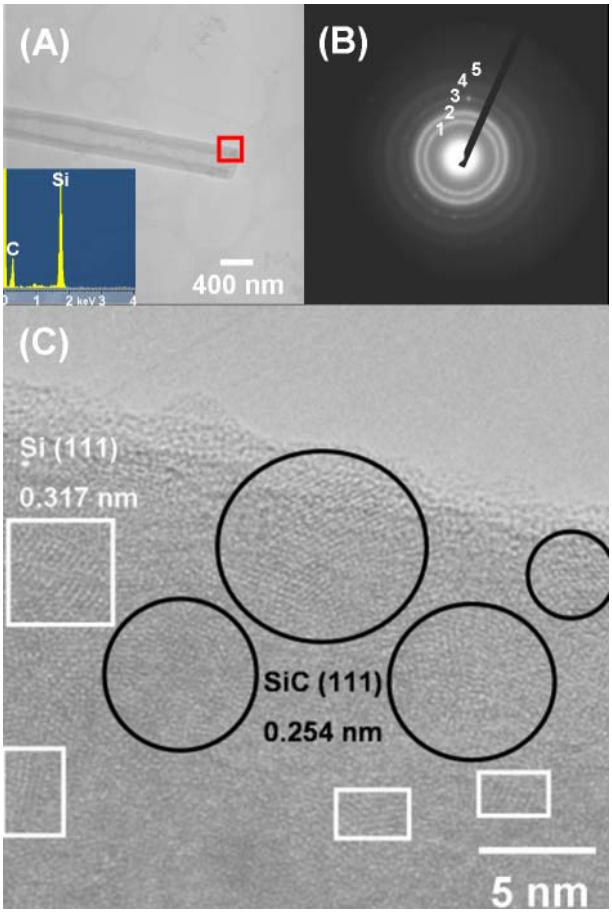


**Figure 3.7** TEM studies of a sample grown at 923 K followed by heat treatment at 1273 K. (A) Low magnification image and EDX (inset, from the squared area). (B) SAED, (C) High-resolution image enlarged from a selected area in A.

Figure 3.7A shows the TEM data of a sample deposited at 923 K and annealed at 1273 K. It is one-dimensional and open-end tubular with a diameter of ca. 300 nm and a wall thickness

of 60 - 80 nm. Only Si and C atoms can be observed in the EDX. SAED reveals a pattern with five distinctive rings in Figure 3.7B, suggesting that the sample is polycrystalline. They can be assigned to cubic Si with an estimated lattice parameter $a$ = 0.54 nm and cubic β-SiC with an estimated lattice parameter $a$ = 0.44 nm.[17,18] Starting from the most inside ring, these rings are assigned to the reflections from Si(111), SiC(111), Si(200), SiC(220), and SiC(311) planes. An HRTEM image, enlarged from the selected area in Figure 3.7A, is shown in Figure 3.7C. Two different lattice spacing values, 0.317 nm and 0.254 nm, are observed and assigned to Si (111) and β-SiC (111) planes, respectively.[17,18]

The Si content will be estimated using the TGA result discussed below. The possible sources of the Si crystallites are the following ones. The first is the extrusion of Si from the polymeric material within the preceramic precursor. In literature, in the preparation of β-SiC via the Yajima-type routes, this was frequently observed at the high temperature processing stage.[12,20,21] Another possible source of Si is from the gas phase decomposition of $MeSiHCl_2$.[22] It was reported that at 905 K, $MeSiHCl_2$ decomposed into $CH_4$ and $SiCl_2$ initially. Then, $SiCl_2$ was transformed into the final gas phase products $HSiCl_3$ and $SiCl_4$. We propose that in this study, these chlorosilanes may react with Ca to form the Si nanocrystals in the tubular walls.[23]

The data in Figure 3.8 suggest that the tubular structure was formed from an originally sealed heterostructure which ruptured later to allow the inner core to evaporate. The TEM image in Figure 3.8A shows a close examination of a tube with a ruptured end, which parallels to the SEM observations in Figures 3.4E and 3.4F. The presence of a core before the heat treatment is supported by the images of a rare example of a filled tube section shown in Figures 3.8B – 3.8D The TEM image in Figure 3.8B reveals that the section is composed of Si, C, Ca and Cl, as identified by the EDX in Figure 3.8C By analyzing the ED pattern in Figure 3.8D carefully, we conclude that the sample contains β-SiC, Si and $CaCl_2$. In the ED pattern, the polycrystalline diffraction rings 2, 5, and 6 are assigned to β-SiC while the rings 1,

3, and 4 are assigned to Si. The diffraction spots from single crystalline $CaCl_2$ are circled. Based on this and the observations discussed above, we suggest that the as formed one-dimensional precursor material has a sealed radial heterostructure, which is composed of an inner core of $CaCl_2$ encapsulated inside a preceramic shell of $SiC_xH_y$. Later, during the high temperature treatment at 1273 K, $CaCl_2$ vaporizes and raises the pressure inside the heterostructure. This would cause the originally sealed tips to rupture and allows $CaCl_2$ to evaporate. We expect that extended heat treatment should lower the $CaCl_2$ concentration further. Meanwhile, SiC crystallizes inside the shell to form the apparent open-end tube morphology.

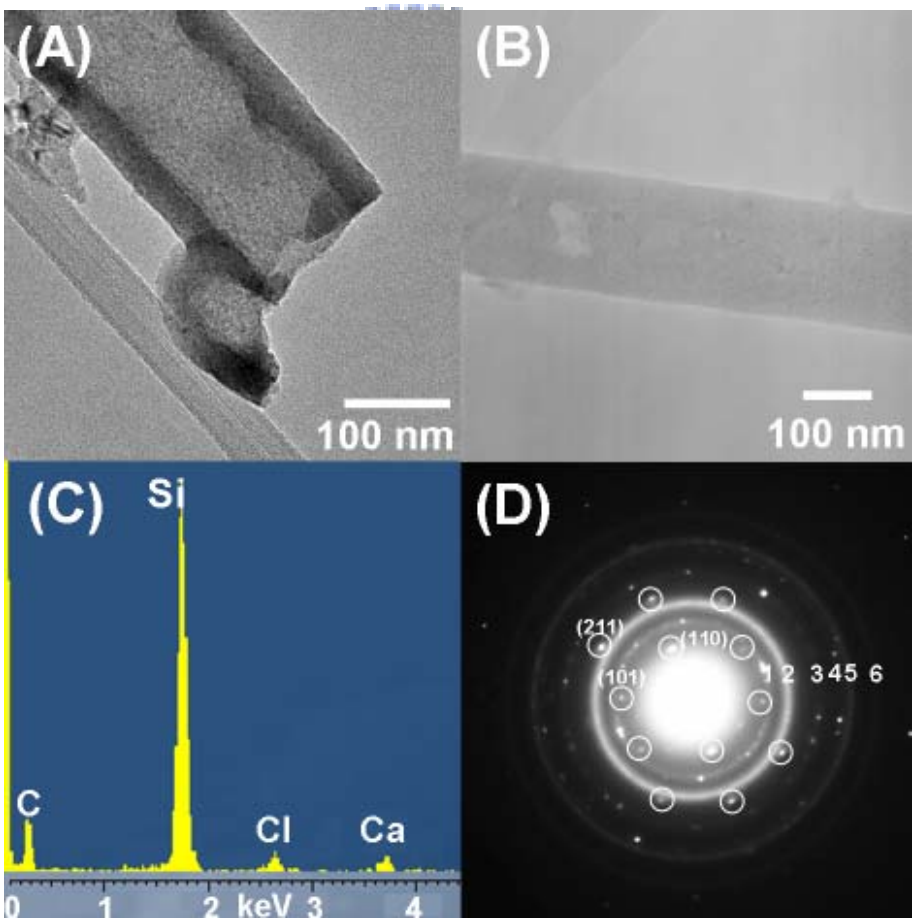


**Figure 3.8** (A) TEM image of a sample grown at 873 K followed by heat treatment at 1273 K showing a tube end. (B) TEM image, (C) EDX, and (D) ED pattern of a sample grown at 923 K followed by heat treatment at 1273 K still retaining the $CaCl_2$ core.

### *3.3.3 TGA Studies*

From the above discussions, it is reasonable to assume that the tubular products are composed of β-SiC mainly. Silicon appears to be a minor component. In addition, the samples may contain amorphous SiC (*a*-SiC) and amorphous C (*a*-C). To understand the stability and composition of the products, they were analyzed by TGA in an ambiance of 100 sccm of flowing air. For the sample grown at 923 K followed by heat treatment at 1273 K, it showed 5% weight loss at 873 K in Figure 3.9(A). This was due to the oxidation of carbon atoms in

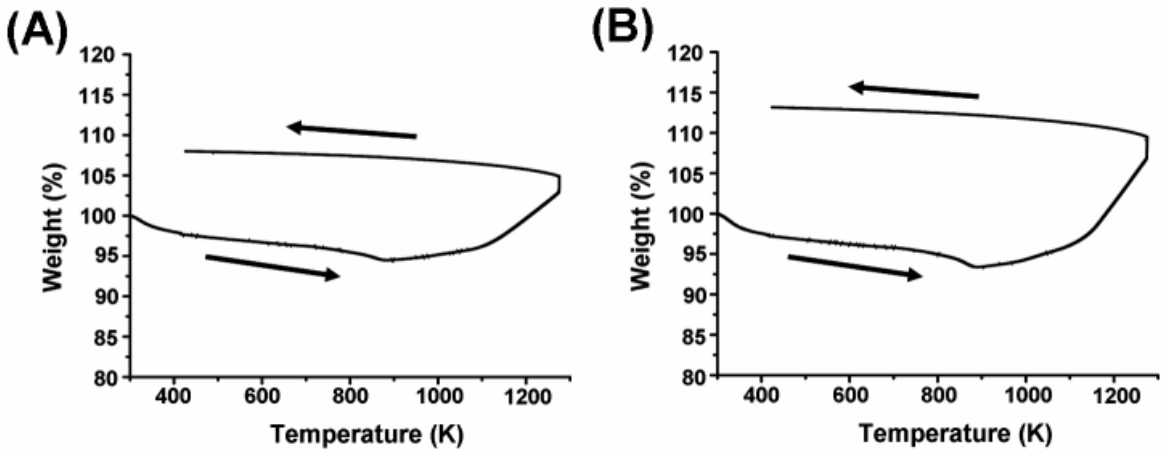


**Figure 3.9** TGA of (A) a sample grown at 923 K followed by heat treatment at 1273 K, (B) a sample grown at 823 K followed by heat treatment at 1273 K.

the sample to form volatile $CO_2$. Bulk β-SiC is known for its resistance to air oxidation at high temperatures.[24] *a*-SiC may be oxidized more easily but the weight should be increased instead of lowered. Thus, the only origin of weight loss is the oxidation of *a*-C. As the temperature increased from 873 K to 1273 K, the weight increased 8%. Then, as the sample was heated at 1273 K for 10 min, the weight increased 2%. Finally, after the temperature was lowered to 425 K, another 3% weight increase was observed. We attribute the 13% weight increase, starting at 873 K, to the oxidation of *a*-SiC and Si in the sample to form $SiO_2$. $HSiCl_3$ and $SiCl_4$, generated from the dissociation of $MeSiHCl_2$, are the probable sources of

Si.[22] The final weight was 108% of the initial sample weight. By assuming that only *a*-C was oxidized below 873 K, we employed the trial and error method to estimate possible tube compositions. If the sample does not contain any *a*-SiC, its composition is 84% β-SiC, 11% Si, and 5% *a*-C by weight. This corresponds to an atomic composition of 72% β-SiC, 14% Si and 14% *a*-C. It is possible that the sample contains some *a*-SiC. For example, if the weight of *a*-SiC is 2% and the amount of *a*-C is the same 5%, there are 83% β-SiC and 10% Si. The atomic composition of the sample is determined to be 72% β-SiC, 2% *a*-SiC, 12% Si and 14% *a*-C. Another estimation shows that if the sample contains 8% *a*-SiC and 5% *a*-C by weight, there are 79% β-SiC and 8% Si. This corresponds to an atomic composition of 69% β-SiC, 10% *a*-SiC, 7% Si and 14% *a*-C.

A similar TGA study and data analysis was performed for the sample grown at 823 K followed by heat treatment at 1273 K in Figure 3.9(B). At 823 K, the decomposition of $MeSiHCl_2$ into $HSiCl_3$ and $SiCl_4$ is insignificant.[22] The sample probably contained a reasonably high amount of *a*-SiC but much less Si. For the first example, we assume that the sample did not have Si at all. If so, the atomic composition is estimated to be 46% β-SiC, 34% *a*-SiC, and 20% *a*-C. Another example assumes that the sample contains some Si, 5% by weight. Under this condition, the possible atomic composition is estimated to be 49% β-SiC, 25% *a*-SiC, 6% Si, and 20% *a*-C. Another estimated atomic composition, with 14% Si by weight, is 58% β-SiC, 7% *a*-SiC, 16% Si and 19% *a*-C. Based on the analyses, we conclude that SiC, including β-SiC and *a*-SiC, was the major component in the tubular products. The Si content in the samples should be far less than 20%. It is important to note that the temperature of reaction affected the ceramic precursor structure and composition significantly. The higher reaction temperature produced better mixed and bonded SiC precursor. In turn, after the heat treatment, the better precursor generated better final product, containing more crystallized β-SiC.

### *3.3.4 Proposed Reaction Pathway*

Based on the above information, we propose in Scheme 3.1 a pathway to summarize the overall reaction steps. We suggest that the SiC tubes are grown via a VSRG pathway similar to the one proposed before for the growth of one-dimensional radial heterostructure composed of a $CaF_2$ core and an *a*-C shell.[9] In the current study, the reaction between $MeSiHCl_2$ and Ca produced phase segregated radial heterostructure of $CaCl_2$ and $SiC_xH_y$ on the substrate. The ionic $CaCl_2$, due to a high cohesive force, forms inner core. In addition, because the reaction temperature employed in this study, 773 – 923 K, is significantly lower than the melting point of $CaCl_2$, 1048 K, $CaCl_2$ can only grow into small diameter seeds at the early growth stage.

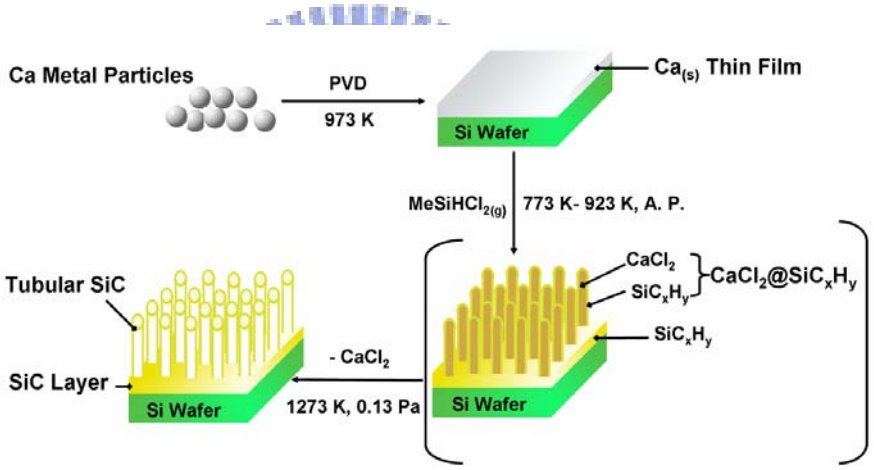


**Scheme 3.1** Reaction steps to form tubular SiC on Si wafer.

The seeds are wrapped inside the other product, soft polymeric shells of $SiC_xH_y$, which are also formed at the vapor-solid reaction interface. Since the inner seed diameter is restricted by the polymeric shell, incorporation of more products to the composite seed does not enlarge it isotropically but elongate it in one dimension. These factors work cooperatively to develop the products into a closed-end cable-like radial heterostructure composed of a $CaCl_2$ core and a $SiC_xH_y$ shell. Then, at an elevated temperature under vacuum, the preceramic shell is transformed into SiC nanocrystals while the $CaCl_2$ core evaporates and erupts from the cable

ends. This would generate the tubes with the apparent open-end morphology.

### 3.4 Field Emission Property Studies

Field emission property of the tubes is evaluated.[25] As shown in Figure 3.10A, a sample grown on Si(100) at 873 K followed by heat treatment at 1273 K shows an excellent emission property $E_{to}$ (turn-on field) 2.8 V/μm and $E_{th}$ (threshold field) exceeding 16 V/μm. Another sample, deposited at 923 K followed by heat treatment at 1273 K, showed an $E_{to}$ 2.5 V/μm and $E_{th}$ less than 7 V/μm in Figure 3.10B. Clearly, the tubes grown at 923 K performed better than the ones grown at 873K, even though they were heat-treated at the same temperature of 1273 K. For both samples, the Fowler-Nordheim plots of the curves showed linear sections above $E_{to}$. This suggests that their field emission mechanism is conventional.[26] It is known that the field enhancement factor, β, is strongly dependent on the sample geometry.[27-28] Generally, samples with high one dimensional aspect ratio structures showed low turn on values.[29,30] In this study, employing a work function (Φ) value of 4.4 eV for SiC and slopes of the F-N plots in the insets in Figure 3.8, the β values are estimated to be 1800 and 2900 for the samples grown at 873 K and 923 K, respectively.[31] The reason why that the tubes grown at 923 K performed better, emitting higher current at lower field, is attributed to the higher content of crystallized β-SiC in the product. As far as we know, the results discussed above are the first field emission property data for SiC tubes. The data are much lower than most of the reported data of other SiC nanostructures.[29-32]

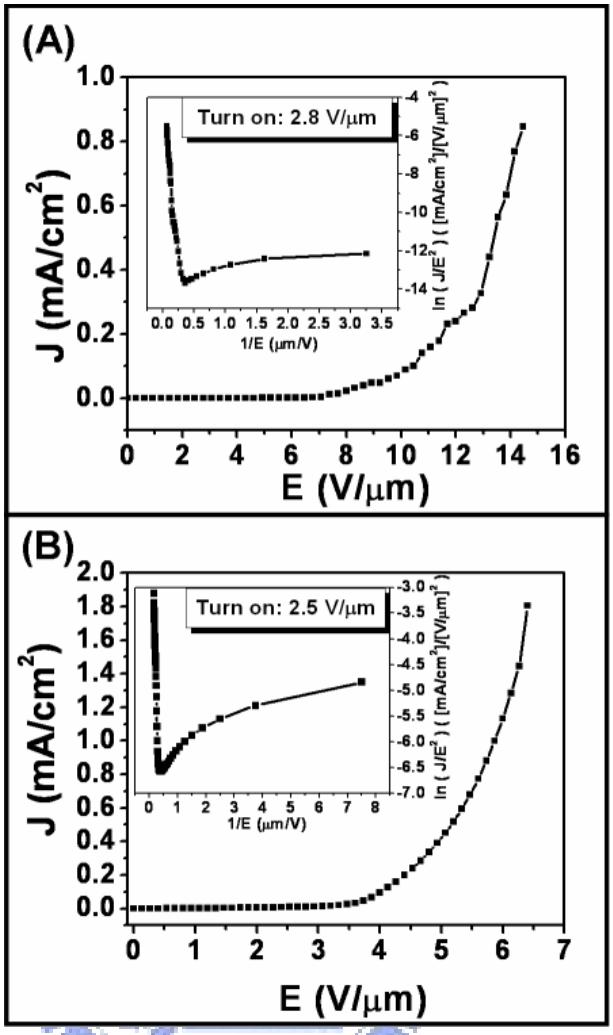


**Figure 3.10** Field emission J-E curve and Fowler-Nordheim (FN) plot (inset). (A) a tubular SiC material on Si(100) at 873 K and heat treated at 1273 K. (B) a tubular SiC material on Si(100) at 923 K and heat treated at 1273 K.

### 3.5 Conclusions

In this study, we have synthesized SiC tubes via a VSRG pathway employing the vapor of $MeSiHCl_2$ to react with Ca deposited on Si. The reaction is a solvent-free Yajima-type process that takes place at the vapor-solid interface. For the reaction, the products $CaCl_2$ and $SiC_xH_y$ phase-segregate and undergo transformation into a cable-like radial heterostructure. After heat treatment, which converts the preceramic $SiC_xH_y$ shell material into SiC and removes the $CaCl_2$ core, the layer of SiC tubes is fabricated on Si. From the tubes, emission of

electrons with a current 10 μA/cm$^2$ can be obtained at an applied field as low as 2.5 V/μm. We suggest that the high performance is not only due to the high aspect ratio of the one dimensional tubular morphology but also to the large field enhancing factor β. This excellent result indicates that the SiC tubes may have promising field-emitting applications for vacuum microelectronic devices.

### 3.6 References


(1) Fissel, A.; Schroter, B.; Richter, W. *Appl. Phys. Lett.* **1995**, *66*, 3182.

(2) Wang, C.-H.; Chang, Y.-H.; Yen, M.-Y.; Peng, C.-W.; Lee, C.-Y.; Chiu, H.-T. *Adv. Mater.* **2005**, *17*, 419.

(3) Dai, H. J.; Wong, E.; Lu, Y. Z.; Fan, S. S.; Lieber, C. M. *Nature* **1995**, *375*, 769.

(4) (a) Pan, Z. W.; Lai, H. L.; Au, F. C. K.; Duan, X. F.; Zhou, W. Y.; Shi, W. S.; Wang, N.; Lee, C. S.; Wong, N. B.; Lee, S. T.; Xie, S. S. *Adv. Mater.* **2000**, *12*, 1186. (b) Ye, H.; Titchenal, N.; Gogotsi, Y.; Ko, F. *Adv. Mater.* **2005**, *17*, 1531.

(5) Li, Y.; Bando, Y.; Golberg, D. *Adv. Mater.* **2004**, *16*, 93.

(6) Sun, X. H.; Li, C. P.; Wong, W. K.; Wong, N. B.; Lee, C. S.; Lee, S. T.; Teo, B. K. *J. Am. Chem. Soc.* **2002**, *124*, 14464.

(7) Hu, J. Q.; Bando, Y.; Zhan, J. H.; Golberg, D. *Appl. Phys. Lett.* **2004**, *85*, 2932.

(8) Wang, H.; Li, X.-D.; Kim, T.-S.; Kim, D.-P. *Appl. Phys. Lett.* **2005**, *86*, 173104.

(9) Huang, C.-H.; Chang, Y.-H.; Lee, C.-Y.; Chiu, H.-T. *Langmuir* **2006**, *22*, 10.

(10) Yen, M.-Y.; Chiu, C.-W.; Shia, C.-H.; Chen, F.-R.; Kai, J.-J.; Lee, C.-Y.; Chiu, H.-T. *Adv. Mater.* **2003**, *15*, 235.

(11) Hsia, C.-H.; Yen, M.-Y.; Lin, C.-C.; Chiu, H.-T.; Lee, C.-Y. *J. Am. Chem. Soc.* **2003**, *125*, 9940.

(12) (a) Yajima, S.; Hayasht, J.; Hasegawa, Y.; Iimura, M. *J. Mater. Sci.* **1978**, *13*, 2569. (b) Hasegawa, Y.; Iimura, M.; Yajima, S. *J. Mater. Sci.* **1980**, *15*, 720. (c) Hasegawa, Y.; Okamura, K. *J. Mater. Sci.* **1983**, *18*, 3633.

(13)(a) Miller, J. H.; Liaw, P. K.; Landes, J. D. *Mater. Sci. and Eng. A* **2001**, *317*, 49. (b) Miriyala, N.; Liaw, P. K.; Mchargue, C. J.; Snead, L. L. *J. Nucl. Mater.* **1998**, *253*, 1. (c) Liaw, P. K.; Hsu, D. K.; Yu, N.; Miriyala, N.; Saini, V.; Jeong, H. *Acta. Mater.* **1996**, *44*, 2101.

(14) Yoshimoto, T.; Yokogawa, N.; Iwata, T. Jpn. *J. Appl. Phys.* **2006**, *45*, L482.

(15) Evtukh, A. A.; Klyui, N. I.; Litovchenko, V. G.; Litvin, Y. M.; Kprneta, O. B.; Puzikov, V. M.; Semenov, A.V. *Appl. Surf. Sci.* **2003**, *215*, 237.

(16) (a) Canepa, F.; Napoletano, M.; Manfrinetti, P.; Palenzona, A. *J. Alloy. Comp.* **2000**, *299*, 20. (b) Affronte, M.; Laborde, O.; Olcese, G. L.; Palenzona, A. *J.* Alloy. Comp. **1998**, *274*, 68.

(17) Joint Committee for Powder Diffraction (JCPDS) File No. 29-1129. International Center for Diffraction Data, 1982.

(18) Joint Committee for Powder Diffraction (JCPDS) File No. 75-0589. International Center for Diffraction Data, 1982.

(19) Würz, R.; Schmidt, M.; Schöpke, A.; Fuhs, W. *Appl. Surf. Sci.* **2002**, *190*, 437.

(20) (a) Bianconi, P. A.; Weidman, T. W. *J. Am. Chem. Soc.* **1989**, *110*, 2342.(b) Bianconi, P. A.; Schilling, F. C.; Weidman, T.W. *Macromolecules* **1989**, *22*, 1697.

(21) Seyferth, D.; Wood, T. G.; Tracy, H. J.; Robison, J. I. *J. Am. Ceram. Soc.* **1992**, *75*, 1300.

(22) Ring, M. A.; O'Neal, H. E.; Walker, K. L. *Int. J. Chem. Kinet.* **1998**, *30*, 89.

(23) Huang, C.-H.; Chang, Y.-H.; Lin, H.-K.; Peng, C.-H.; Chung, W.- S.; Lee, C.-Y.; Chiu, H.-T. *J. Phys. Chem. C.* **2007**, *111*, 4138.

(24) Narushima, T.; Goto, T.; Iguchi, Y.; Hirai, T. *J. Am. Ceram. Soc.* **1990**, *73*, 3580.

(25) Lee, Y.-C.; Pradhan, D.; Lin, S.-J.; Chia, C.-T.; Cheng, H.-F.; Lin, I.-N. *Diamond Relat. Mater.* **2005**, *14*, 2055.

(26) Fowler, R. H.; Nordheim, L. W. *Proc. R. Soc. London, Ser. A* **1928**, *119*, 173.

(27) Yamanaka, T.; Tampo H. ; Yamada, K.; Ohnishi K.; Hashimoto M.; Asahi, H. *Phys. Status Solidi (c)* **2002**, *1*, 469.

(28) Lee, C. J.; Lee, T. J.; Lyu, S. C.; Zhang Y.; Ruh, H.; Lee, H. J. *Appl. Phys. Lett.* **2002**, *81*, 3648.

(29) Shen, G.; Bando, Y.; Ye, C.; Liu, B.; Golberg, D. *Nanotechnology* **2006**, *17*, 3468.

(30) Deng, S. Z.; Li, B. Z.; Wang, W. L.; Xu, N. S.; Zhou, J.; Zheng, X. G.; Xu, H. T.; Chen, J.;

She, J. C. *Appl. Phys. Lett.* **2006**, *89*, 23118.

(31) Wu, Z. S.; Deng, S. Z.; Xu, N. S.; Chen, J.; Zhou, J.; Chen, J. *Appl. Phys. Lett.* **2002**, *80*, 3829.

(32) Zhou, X. T.; Lai, H. L.; Peng, H. Y.; Au, F. C. K.; Liao, L. S.; Wang, N.; Bello, I.; Lee, C. S.; Lee, S. T. *Chem. Phys. Lett.* **2000**, *318*, 58.

## 3.7 Appendix

### Composition Analysis

We assume that the samples may contain *a*-C, Si, *a*-SiC, and β-SiC. In the curve (A) in Figure 3.9, we observe a maximum 5% weight loss at 873 K. It is proposed that this is due to the oxidation of C atoms in *a*-C. From 873 K to 1273 K, the weight increase is 8%. Then, the weight increases 2% at 1273 K. From 1273 K to 425 K, the weight increases 3%. From 873 K to 1273 K then to 425 K, the weight increases 13 % in total. We attribute this to the oxidation of Si atoms in *a*-SiC and Si to form $SiO_2$. The final weight is 108% of the original one. The weight loss at 873 K is assumed to be all contributed by the oxidation of C. The assumptions, equations, and results are shown below.

1. The weight % of -SiC is $x$. Assume it is resistant to oxidation and the weight % does not change.
2. The weight % of *a*-SiC is $y$. Assume it can be fully oxidized to form $SiO_2$ and $CO_2$. The weight % after the oxidation is [M.W.($SiO_2$)/ M.W.(*a*-SiC)]*$y$, (60/40)$y$ = 1.5$y$.
3. The weight % of Si is $z$. Assume it can be fully oxidized to form $SiO_2$. The weight % after the oxidation is [M.W.($SiO_2$)/ A.W.(Si)]*$z$, (60/28)$z$
4. The weight % of *a*-C is $w$, which is the weight loss at 873 K. Assuming it can be fully oxidized to form $CO_2$, the weight % after the oxidation reduces to 0.

Two equations can be established for the initial and final weight %.

Initial weight %: $x + y + z + w = 100$

Final weight %: $x + 1.5\,y + (60/28)z + 0$ = Total final weight % found in TGA

For (A), $w$ is 5. The total final weight % found in TGA is 108.

There are 3 variables to be solved but we can set up only 2 equations. Thus, we use the trial and error method to derive possible compositions of (A). Possible compositions should offer between 7 and 8 weight % increase relative to the initial weight %.

Possible compositions of (A):

| Trial 1 | β-SiC | *a*-SiC | Si | *a*-C | Total |
|---|---|---|---|---|---|
| estimated initial weight % | 84 | 0 | 11 | 5 | 100 |
| weight % after oxidation | 84 | 0 | 23.6 | 0 | 107.6 |
| estimated atomic % | 72 | 0 | 14 | 14 | 100 |

| Trial 2 | β-SiC | *a*-SiC | Si | *a*-C | Total |
|---|---|---|---|---|---|
| estimated initial weight % | 83 | 2 | 10 | 5 | 100 |
| weight % after oxidation | 83 | 3 | 21.4 | 0 | 107.4 |
| estimated atomic % | 72 | 2 | 12 | 14 | 100 |

| Trial 3 | β-SiC | *a*-SiC | Si | *a*-C | Total |
|---|---|---|---|---|---|
| estimated initial weight % | 79 | 8 | 8 | 5 | 100 |
| weight % after oxidation | 79 | 12 | 17.1 | 0 | 108.1 |
| estimated atomic % | 69 | 7 | 10 | 14 | 100 |

In the curve (B), we observe 7% weight loss at 873 K for the oxidation of *a*-C. From 873 K to 1273 K then to 425 K, the weight increase is 20 % for the oxidation of *a*-SiC and/or Si to form $SiO_2$. The final weight is 113 % of the original one. The trial and error method is used again to derive the possible compositions of (B) offering an overall 13 – 14 weight % increase. Since the product was prepared at low temperature, we assume that the *a*-SiC content should be high while the Si content is low. Thus, even though Trial 4 can offer satisfactory composition estimation, the result is unlikely because the amount of *a*-SiC in the trial is assumed to be 0.

Possible compositions of (B):

| Trial 1 | β-SiC | *a*-SiC | Si | *a*-C | Total |
|---|---|---|---|---|---|
| estimated initial weight % | 53 | 40 | 0 | 7 | 100 |
| weight % after oxidation | 53 | 60 | 0 | 0 | 113 |
| estimated atomic % | 46 | 34 | 0 | 20 | 100 |

| Trial 2 | β-SiC | *a*-SiC | Si | *a*-C | Total |
|---|---|---|---|---|---|
| estimated initial weight % | 58 | 30 | 5 | 7 | 100 |
| weight % after oxidation | 58 | 45 | 10.7 | 0 | 113.7 |
| estimated atomic % | 49 | 25 | 6 | 20 | 100 |

| Trial 3 | β-SiC | *a*-SiC | Si | *a*-C | Total |
|---|---|---|---|---|---|
| estimated initial weight % | 71 | 8 | 14 | 7 | 100 |
| weight % after oxidation | 71 | 12 | 30 | 0 | 113 |
| estimated atomic % | 58 | 7 | 16 | 19 | 100 |

| Trial 4 | β-SiC | *a*-SiC | Si | *a*-C | Total |
|---|---|---|---|---|---|
| estimated initial weight % | 75 | 0 | 18 | 7 | 100 |
| weight % after oxidation | 75 | 0 | 38.6 | 0 | 113.6 |
| estimated atomic % | 60 | 0 | 21 | 19 | 100 |

# Chapter 4

## Synthesis of Pseudo Thin Plate Silicon Carbide Nanostructure- Another Case of Yajima-Type Reaction at the Vapor-Solid Interface

### 4.1 Introduction

In Chapters 2 and 3, we fabricated cubical nanocages and tubular one-dimensional SiC nanostructures via VSRG methods. NaCl and $CaCl_2$ acted as in-situ generated templates to assist the SiC morphology formation.[1-2] Here, we present another example showing in-situ generated $MgCl_2$ can act as a template to assit the formation of large area pseudo thin plate SiC nanostructure by employing vapors of organochlorosilanes, $MeSiHCl_2$ and $Me_2SiCl_2$ to react with Mg metal at relatively low temperatures.

### 4.2 Experimental Section

A hot-wall reactor composed of a Lindberg HTF55122A tube furnace and a 27 mm diameter quartz tube was used. RF power (13.56 MHz) was applied to the reactor through two pieces of copper foil electrodes outside the furnace. Mg powder (Showa 99 %, 0.30 g, 12.5 mmole) in a 10 cm quartz boat was placed in the plasma region. The powder was treated with hydrogen plasma (10 W, $H_2$ 20 sccm) under the assistance of a constant flow of $H_2$ 20 sccm at room temperature for 1 h to remove surface oxide. Then, under 1 atm of Ar, the treated powders were pushed into the reactor center. $MeHSiCl_2$ was vaporized at 255 K under the assistance of a constant flow of Ar (1 - 2 sccm) into the reactor to react with Mg metal at 823 K 1 atm for 14 h. Yellow powder was obtained after heat treatment at 1273 K for 1 h. In the other case, black powder was obtained from $Me_2SiCl_2$ reacting with Mg powder at 923 K for 14 h and then heat treated at 1273 K for 1 h.

SEM and EDX data were collected using a JEOL JSM-6330F at 15 kV. TEM and ED images were obtained on a JEOL JEM-2010 at 200 kV. HRTEM images were acquired on a JEOL JEM-4000EX at 400 kV. XRD studies were carried out using a BRUKER AXS D8 ADVANCE diffractometer using Cu Kα1 radiation. FT-IR spectra were collected using a Perkin Elmer Spectrum One.

## 4.3 Results and Disscussion

### *4.3.1 Characterizations of the yellow product prepared from Mg and $MeSiHCl_2$*

In Figure 4.1, a low-magnification SEM image of the yellow powder reveals numerous thin plate structures in Figure 4.1A. The high-magnification SEM image in Figures 4.1B and C present that the hexagonal plates with mumberous particles. The plates have a thickness of c.a. 50 nm and an edge length of c.a. 5 μm. The EDX spectrum confirms that the sample contains Si, C, and traces of Mg and Cl, as shown in Figure 4.1D.

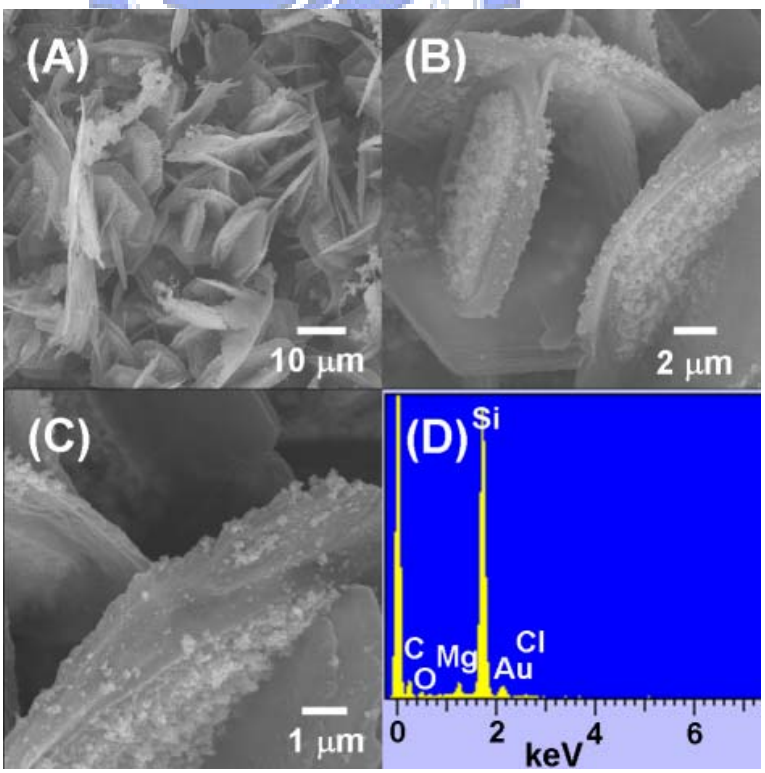


**Figure 4.1** SEM images the yellow product prepared from Mg and $MeSiHCl_2$ (A) Low-magnification, (B) and (C)High-magnification, and (D) EDX.

Low magnification images show that the sample contains one layer particles with a diameter of 200 - 250 nm on the thin plate in Figures 4.2A and B. SAED reveals a slightly diffused pattern with three distinctive rings in the inset of Figure 4.2B. This suggests that the sample have a polycrystalline cubic phase structure. Starting from the most inside ring, these rings are assigned to the reflections from SiC(111), SiC(220), and SiC(311) planes. They can be assigned to cubic β-SiC with an estimated lattice parameter $a$ = 0.44 nm.[3] HRTEM image was shown in Figures 4.2 C and D. Some fringes spaced at 0.254 nm apart can be observed in the particles and the thin plate layer. These are assigned to be originated from the (111) planes of β-SiC. Obviously, particle and thin plate are the same composition, β-SiC.

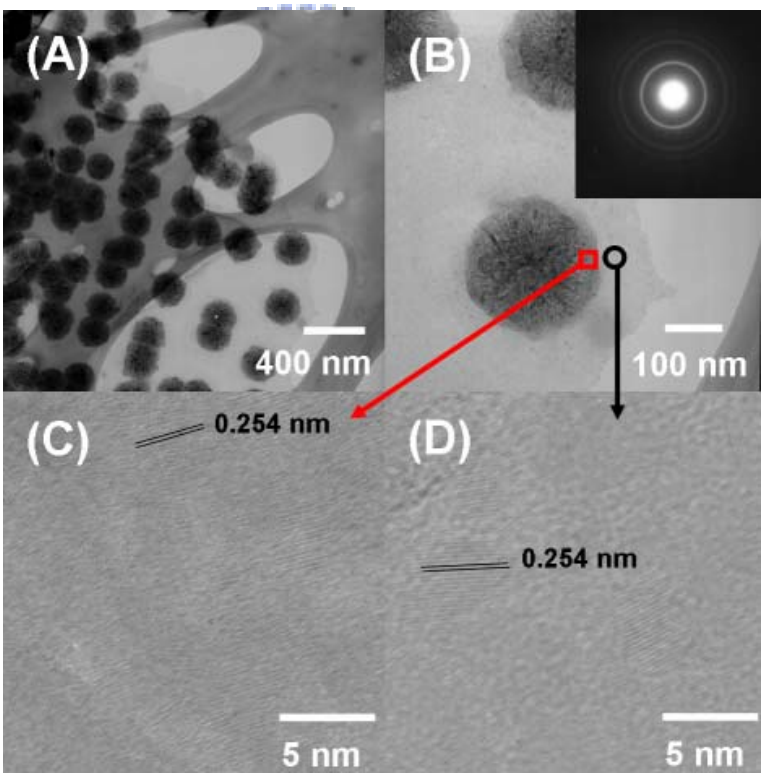


**Figure 4.2** TEM images of yellow product prepared from Mg and $MeSiHCl_2$ (A) and (B) Low-magnification TEM image and SAED inset in (B), (C) HRTEM image of particle from the red square in part (B), and (D) HRTEM image of thin plate, black circle in part (B).

In addition, an FT-IR spectrum in Figure 4.3 shows a broad absorption at 813.9 $cm^{-1}$,

which can be assigned to the Si-C stretching. An XRD pattern in Figure 4.4 shows major β-SiC and minor Si patterns.[3,4] Si appears to be extracted from the polymeric preceramic precursor. In literature, in the preparation of β-SiC via the Yajima-type routes, this was frequently observed at the high temperature processing stage.[5-7] In Chapter 2, we also demonstrated that Si nanoparticles were obtained from the processing of rigid polysilane precursor. We suggest that the product is β-SiC.

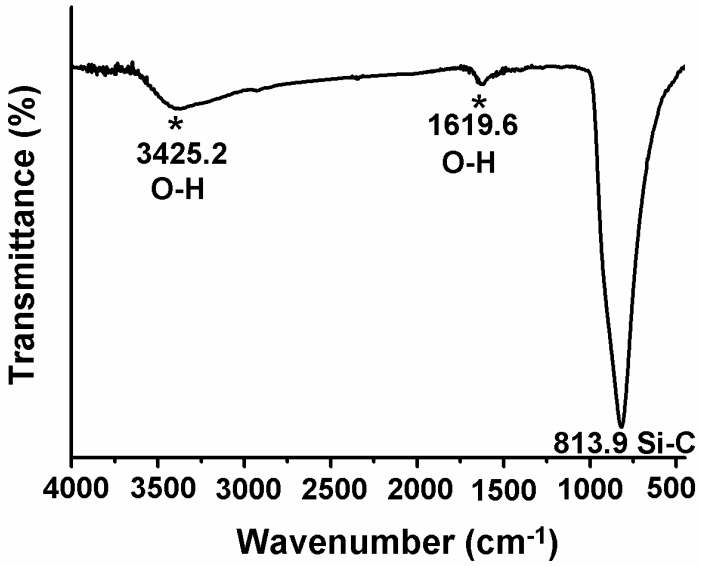


**Figure 4.3** FT-IR spectrum of the yellow product prepared from Mg and $MeSiHCl_2$. The absorption bands marked with "*" are from absorbed $H_2O$ molecules.

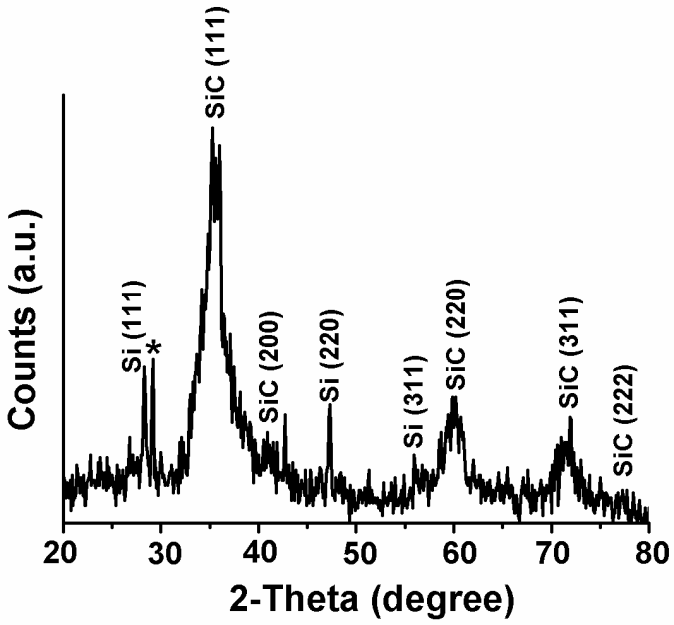


**Figure 4.4** XRD partten of the yellow product prepared from Mg and $MeSiHCl_2$. The peaks marked with "*" are from the XRD holder.

### *4.3.2 Characterizations of the black product prepared from Mg and $Me_2SiCl_2$*

In Figure 4.5, a low-magnification SEM image of the black powder reveals many plates with tens of micrometers in edge lengths in Figure 4.5A. The high-magnification SEM image in Figure 4.5B presents that the plate was composites numberous nanoparticles with dameters of 200 – 300 nm and a thickness of c.a. 300 nm. The EDX spectrum confirms that the sample contains Si, C, and traces of Mg and Cl, as shown in the inset of Figure 4.5B. Low magnification TEM image also shows that the plate is formed by the particles connected together in Figures 4.5C and D. SAED reveals a slightly diffused pattern with three distinctive rings in the inset of Figure 4.5E. Starting from the most inside ring, these rings are assigned to the reflections from SiC(111), SiC(220), and SiC(311) planes. They can be assigned to cubic β-SiC with an estimated lattice parameter $a$ = 0.44 nm.[3] HRTEM image is shown in Figures 4.5F. Some fringes spaced at 0.251 nm apart can be observed. These are assigned to be originated from the (111) planes of β-SiC. Besides, an XRD in Figure 4.6 shows only β-SiC

phase in the product.

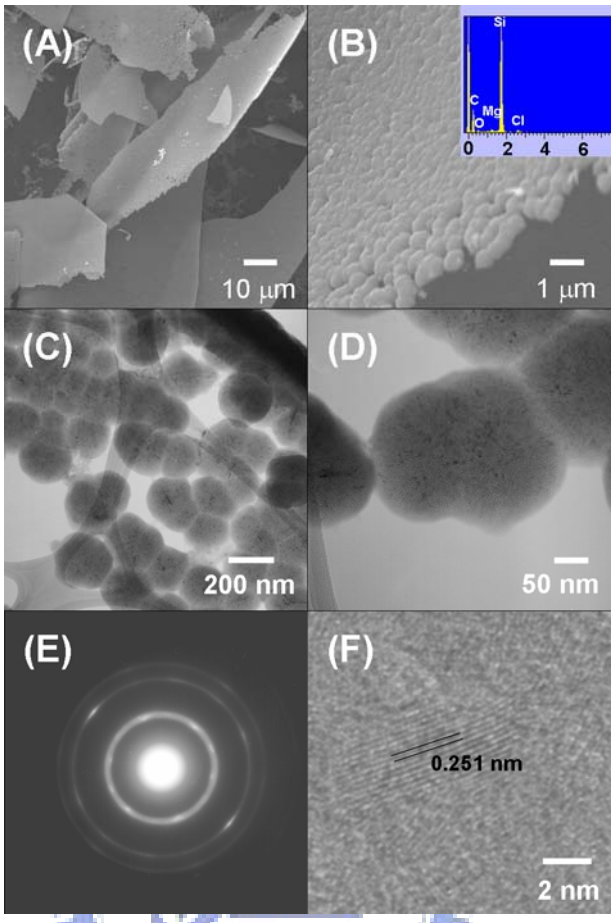


**Figure 4.5** Characterizations of black product prepared from Mg and $Me_2SiCl_2$. (A) Low-magnification SEM image, (B) high-magnification SEM image and EDX (inset), (C) and (D) low-magnification TEM images, (E) SAED, and (F) HRTEM image.

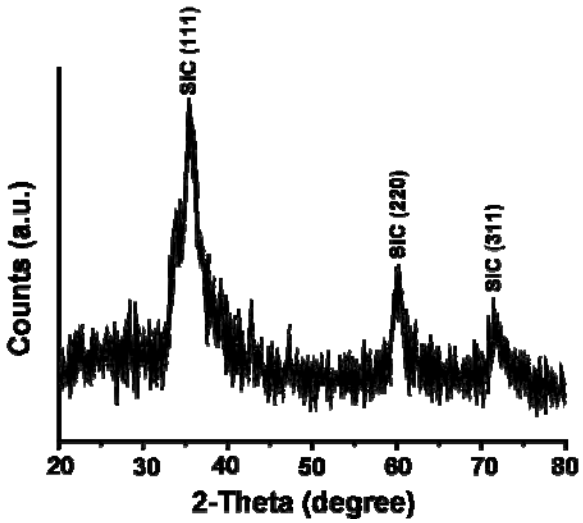


**Figure 4.6** XRD partten of the black product prepared from Mg and $Me_2SiCl_2$.

### *4.3.3 Proposed Reaction Pathway*

Based on the above information, we propose in Scheme 4.1 a pathway to summarize the overall reaction steps. As we know, bulk $MgCl_2$ is easy to form lamellar shape based on $CdI_2$ layer structure. The more detail will discuss bellow. At the beginning, from the reactions between $MeHSiCl_2$ and $Me_2SiCl_2$ and Mg, the products $MgCl_2$ and preceramic precursor are phase-segregated into a stacking layer heterostructure. After heat treatment, the precursor material converts into SiC while $MgCl_2$ is removed. Thus, the pseudo thin plate SiC nanostructure is fabricated. In the reaction between $MeHSiCl_2$ and Mg, not only one layer particles was formed but also thin plates. We suggest that the Si-H bonds in the precursor, $MeHSiCl_2$, may be decomposed on the surface $MgCl_2$ to form the thin plates. After heat treatment, thin plate SiC structure was frbricated.

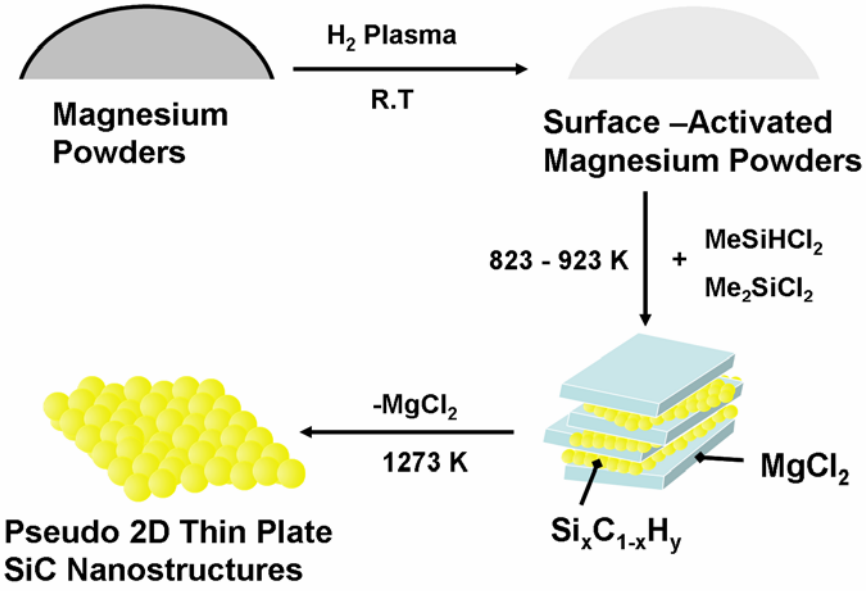


**Scheme 4.1** Reaction steps to form pseudo thin plate SiC nanostructures.

## 4.4 Comparison with Previous Reports through VSRG Process

By varing the active metals from Na, Ca, Mg, we can grow various SiC nanostructures at

reaction temperature 523 – 923 K. These are below the melting points of the corresponding of ionic salt products (NaCl, 1074 K; $MgCl_2$, 985 K; $CaCl_2$, 1045 K.) Ceramic polycarbosilanes (soft and rigid ceramic polycarbosilane) from various organochlorosilanes reacting with the metal reactants at different reaction temperatures have diverse affinity to the salt products. For example, soft ceramic polycarbosilane is flexible to cover the salt products surface. Heat treatment of the polycarbosilanes converts them to various SiC nanostructures according to the shape of salt products. In contrast, rigid ceramic polycarbosilane is too hard to cover the salt products. It is transformed into spherical SiC (nano) particles after heat treatment. In nature, cubic shape bulk NaCl based on NaCl rock structure is commonly discovered in Figure 6.7A.[8] For the same reason, bulk $MgCl_2$ is easy to form lamellar shape based on $CdI_2$ layer structure as shown in Figure 6.7B.[9] On the other hand, $CaCl_2$ is orthorhombic phase rutile-like structure. For this salt, the spherical and planar shapes are most commonly occurred. Because the reaction temperature is significantly lower than the melting point of $CaCl_2$, 1048 K, $CaCl_2$ can only grow into small diameter seeds at the early growth stage. The seeds are wrapped inside the other product, soft polymeric shells of $SiC_xH_y$, which are also formed at the vapor-solid reaction interface. Since the inner seed diameter is restricted by the polymeric shell, incorporation of more products to the composite seed does not enlarge it isotropically but elongate it in one dimension. Therefore, $CaCl_2$ salt can be formed 1D nanowires in our system.

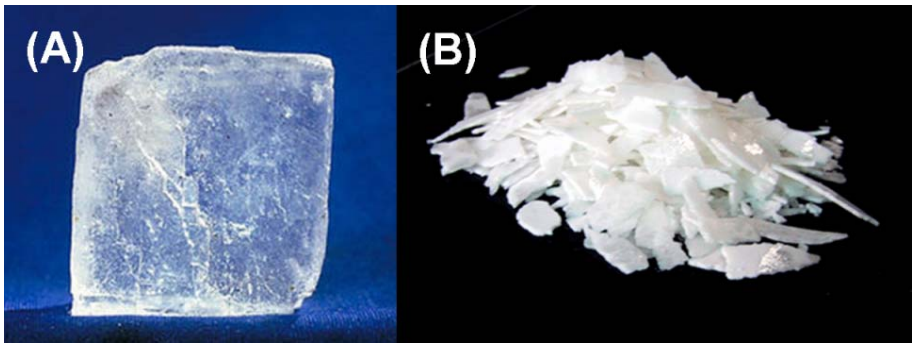


**Figure 4.7** Bulk morphology of (A) NaCl, and (B) $MgCl_2$.[8,9]

## 4.5 Conclusions

We have successfully fabricated pseudo thin plate SiC nanostructure via VSRG method employing the vapor of $MeHSiCl_2$ and $Me_2SiCl_2$ to react with Mg metal. We suggested that the pseudo thin plate SiC nanostructure was fabricated via the same phase segregation concept discussed in chapters 2 and 3. In this chapter, like NaCl and $CaCl_2$, $MgCl_2$ acts as a lamellar template in-situ to assist the growth. Oncemore, we discover that nature of the salt morphology play important role to shape the final products morphology.

## 4.6 References


(1) Wang, C.-H.; Chang, Y.-H.; Yen, M.-Y.; Peng, C.-W.; Lee, C.-Y.; Chiu, H.-T. *Adv. Mater.* **2005**, *17*, 419.

(2) Wang, C.-H.; Lin, H.-K.; Ke, T.-Y.; Palathinkal, T.-J.; Tai, N.-H.; Lin, I-N.; Lee, C.-Y.; Chiu, H.-T. *Chem. Mater.* **2007**, impress.

(3) Joint Committee for Powder Diffraction (JCPDS) File No. 29-1129. International Center for Diffraction Data, 1982.

(4) Joint Committee for Powder Diffraction (JCPDS) File No. 75-0589. International Center for Diffraction Data, 1982.

(5) (a) Yajima, S.; Hayasht, J.; Hasegawa, Y.; Iimura, M. *J. Mater. Sci.* **1978**, *13*, 2569. (b) Hasegawa, Y.; Iimura, M.; Yajima, S. *J. Mater. Sci.* **1980**, *15*, 720.

(6) Bianconi, P. A.; Weidman, T. W. *J. Am. Chem. Soc.* **1989**, *110*, 2342.

(7) Seyferth, D.; Wood, T. G.; Tracy, H. J.; Robison, J. I. *J. Am. Ceram. Soc.* **1992**, *75*, 1300.

(8) http://zh.wikipedia.org/wiki/

(9) http://www.sdhh.com.cn/cp_lhm.htm

(10) Huang, C.-H.; Chang, Y.-H.; Lin, H.-K.; Peng, C.-H.; Chung, W.- S.; Lee, C.-Y.; Chiu, H.-T. *J. Phys. Chem. C.* **2007**, *111*, 4138.

# Chapter 5

## Deposition of Mesoporous Silicon Carbide Thin Films from $(Me_3Si)_4Sn$ - Tin Nanoparticles as In Situ Generated Template

### 5.1 Introduction

In nature and laboratory, morphology and structure of many objects are shaped and altered mainly by phase segregation. Interactions among different domains of the constituents may perform cooperatively as hard and soft templates. The effects can be observed in systems such as the formation of minerals,[1] block copolymers,[2] and nanosized inorganic and organic structures.[3-5] In this report, we wish to discuss how to fabricate mesoporous silicon carbide thin films on silicon substrates based on the methodology. Silicon carbide is an excellent semiconductor material for high temperature, high power and high frequency applications in harsh environments.[6,7] Recently, many new routes have been developed to prepare silicon carbide nanostructures and thin films. These include solid-state carbothermal reduction of silica, solution phase sol-gel synthesis and preceramic process, and various chemical vapor deposition techniques.[3, 8-18] Porous silicon carbide thin film on SiC or Si is potentially useful for luminescence and sensing devices.[19,20] To date, electrochemical etching of bulk silicon carbide substrates in HF solution is the only method to fabricate it into the porous form onto SiC or Si wafers.[19-21] However, the route is not suitable for the fabrication of porous SiC thin films onto Si substrates. This is due to the high reactivity of Si towards the HF electrolyte, which would cause preferential dissolution of the Si substrate.[22] Porous SiC powders prepared by carbothermal reduction are difficult to integrate into the device fabrication process either.[16-18] Clearly, a new method is needed to overcome the difficulty. Here, we demonstrate the integration of a metal-organic chemical vapor deposition (MOCVD) process and phase

segregation strategy to achieve this goal. We show that preceramic amorphous $Si_xC_{1-x}$ thin films containing Sn nanoparticles can be deposited on Si substrates employing $Sn(SiMe_3)_4$ as the precursor. After the Sn nanoparticles are removed, the $Si_xC_{1-x}$ films are processed further into mesoporous semiconducting β-SiC thin films.

## 5.2 Experimental Section

### *5.2.1 Materials.*

The materials used in the present work included trimethylchlorosilane (Aldrich), lithium ribbon (Aldrich, 99.9%), tin(IV) chloride (Aldrich), hydrofluoric acid (Aldrich, 48%), tetrahydrofuran (Echo Chemical, HPLC grade), acetone (Echo chemical, HPLC grade), 1,1,1-trichloroethane (Echo Chemical), buffered hydrofluoric acid (BOE) solution (Echo Chemical), n-type silicon (100) wafer (1 - 10 Ω·cm), p-type silicon (111) wafer (7 - 30 Ω·cm). The MOCVD precursor $Sn(SiMe_3)_4$ was synthesized using a literature route.[23]

### *5.2.2 Growth of Sn/amorphous $Si_xC_{1-x}$ Thin Films, I*

The MOCVD experiments were performed in a hot-wall reactor composed of a Lindberg 55342-4 horizontal tube furnace and a 27 mm-diameter quartz tube shown in Figure 1. Radio frequency (RF) power (13.56 MHz) was applied to the reactor through two pieces of copper foil electrodes. After the cleaned Si wafers (1 cm × 1 cm) were placed inside the reactor, they were further treated by $H_2$ plasma (40 sccm, 20 W, 66.7 Pa) at 923 K for 10 min to create a surface favorable to thin film deposition. $Sn(SiMe_3)_4$ (0.5 g) was evaporated into the reactor at 333 K and 26.7 Pa under the assistance of a constant flow of $H_2$ (20 sccm). The deposition was carried out at 923 K for 6 h to grow dark green thin films (**I**) on the wafers.

### *5.2.3 Preparation of Samples I-P, I-P-HF, II, III, and IV*

Further processing of **I** by $H_2$ plasma (20 sccm, 10 W) at 923 K for 6 h followed by dipping into $HF_{(aq)}$ (48%) for 30 min generated **I-P** and **I-P-HF**, respectively. Then, it was annealed at 1273 K for 1 h to produce **II**. On the other hand, **I-P** and **I** were annealed at 1423 K for 1 h to produce **III** and **IV**, respectively.

### *5.2.4 Preparation of n-type β-SiC/p-type Si heterojunction*

A precursor film **I** was deposited at 923 K for 90 min on p-type Si (7 – 30 Ω·cm) via the MOCVD process described above. After the film was directly annealed at 1423 K to remove Sn particles embedded inside, **IV** was prepared. P was doped into the film **IV** by ion implantation (5 x $10^{14}$ $P^{3+}/cm^2$ at 25 keV) using a Varian E500HP implanter

### *5.2.5 Characterization*

Scanning electron microscopic (SEM) and energy dispersive X-ray (EDX) data were collected using a JEOL JSM-6330F at 15 kV. Transmission electron microscopic (TEM) and selected area electron diffraction (SAED) images were obtained on a JEOL JEM-2010 at 200 kV. X-ray diffraction (XRD) studies were carried out using a Bruker AXS D8 ADVANCE diffractometer using Cu Kα1 radiation. Fourier transform infrared (FT-IR) spectra were carried out using a Perkin Elmer Spectrum One. Gas chromatography-mass spectrometry (GC-MS) data of volatile byproducts trapped at 77 K were measured using a HP 5890 series II (GC) coupled to a Micromass TRIO-2000 and a JEOL JMS-D100. On-line residual gas analysis (RGA) was obtained from a VG Quadruples Sensorlab 300D attached to the reactor. Raman spectra of the samples were measured by using a Jabin Yvon T-64000 equipped with an $Ar^+$ laser (514.5 nm) and a triple monochromator. X-ray photoelectron spectroscopic (XPS) measurements were carried out using a Perkin-Elmer PHI-1600 spectrometer with Mg $K_\alpha$ (1253.6 eV) radiation. Electron probe x-ray microanalysis (EPMA) data were measured from

JEOL JXA-8500F. Secondary ion mass spectrometry (SIMS) was carried out using a Cameca IMS-4f instrument.

Connection of Cu wires to the thin films and wafers was fabricated by applying silver paste to form the contacts followed by heating in an oven at 383 K for 30 min. I-V characters of the thin films were measured with a Keithley 2400 (DC ±5 V). Sheet resistance of the films was determined by four-point probe method using a CMT-SR 2000 N.

## 5.3 Results and Discussion

### *5.3.1 Growth and Characterization of Sn/amorphous $Si_xC_{1-x}$ Thin Films*

The precursor $Sn(SiMe_3)_4$ was vaporized at 333 K into a horizontal hot-wall MOCVD reactor (Figure 5.1) at 923 K to grow thin films on Si substrates. Starting from the precursor inlet, nine pieces of Si wafers were placed at a distance of 5 cm apart inside the reactor. The substrates were numbered from 1 to 9 as the number 1 substrate was at the most upstream position, close to the end of the heated zone, while the number 9 substrate was at the reactor center.

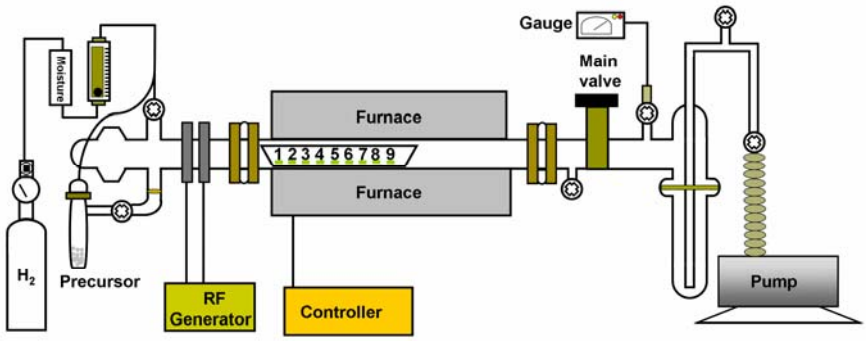


**Figure 5.1** MOCVD reactor setup.

Initially, thin films were grown on all of the substrates so that better deposition locations inside the reactor could be chosen. Starting from sample 1, physical appearance of the films ranged from gray, dark green with silvery white spots, dark green to black as shown in Figure 5.2.

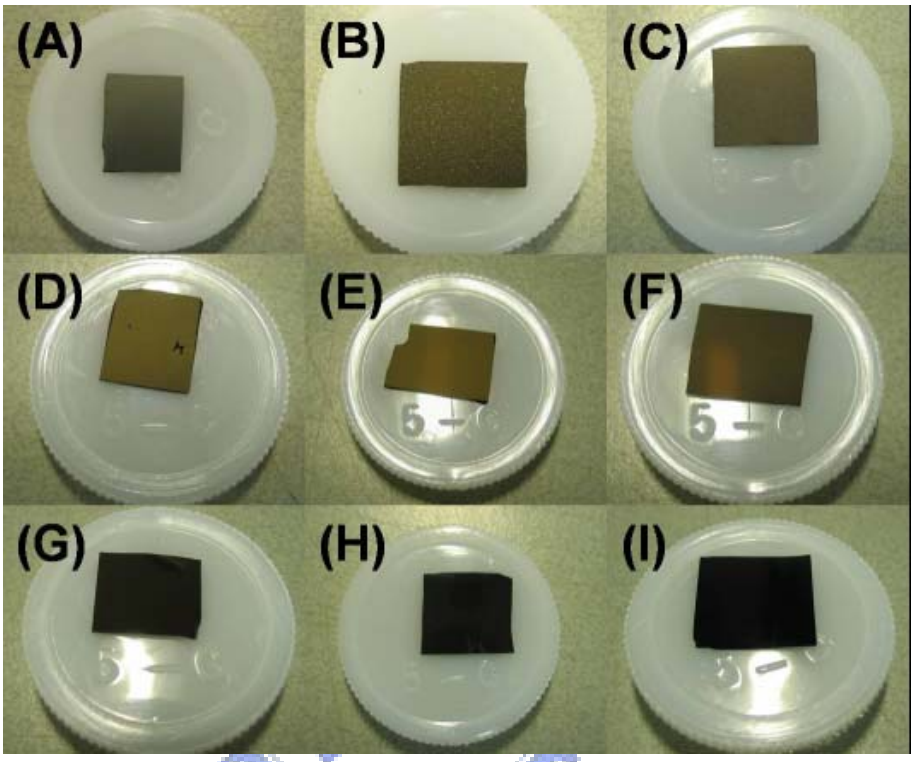


**Figure 5.2** Images of thin films deposited on wafers placed at (A) 40 cm (position 1), (B) 35 cm (position 2), (C) 30 cm (position 3), (D) 25 cm (position 4), (E) 20 cm (position 5), (F) 15 cm (position 6), (G) 10 cm (position 7), (H) 5 cm (position 8), and (I) 0 cm (position 9) away from the center of the furnace.

From SEM studies, morphology and thickness of the films were obtained. From the thickness as shown in Figure 5.3, corresponding film growth rates at these positions were estimated to be 0.4 – 24 nm/min. EPMA and EDX spectra showed that all of the samples contained various amounts of Sn, Si, and C. As shown in the EPMA data in Figure 5.4, this ranges from 53.6 atomic % of Sn, 24.5 atomic % of Si and 21.9 atomic % of C for sample 1 to 3.5 atomic % of Sn, 59.4 atomic % of Si and 37.1 atomic % of C for sample 9.

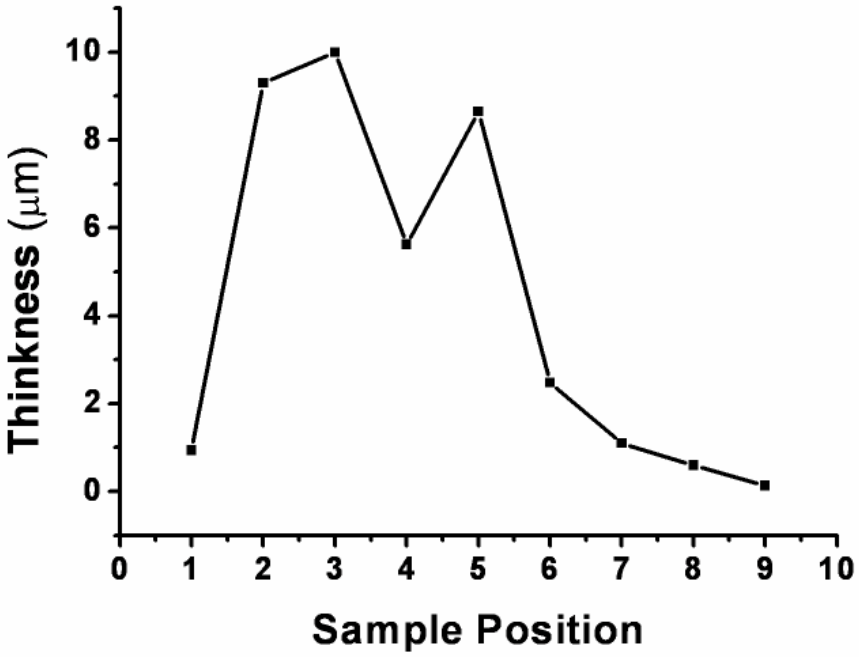


**Figure 5.3** Thickness distributions of the samples in the reactor.

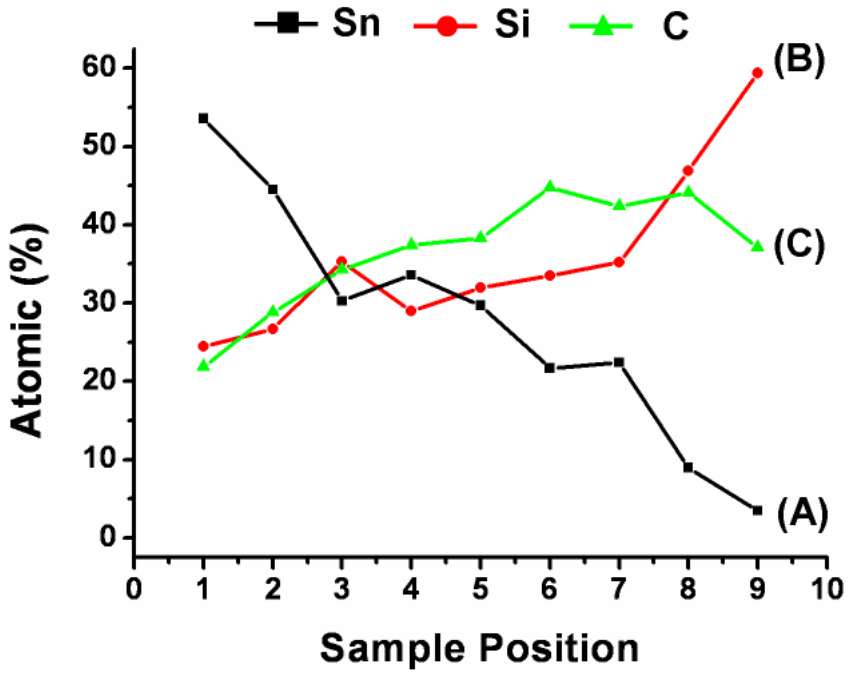


**Figure 5.4** EPMA atomic % concentration of the samples grown from $Sn(SiMe_3)_4$ at 923 K, $H_2$ flow rate 20 sccm, and 26.7 Pa.

For all samples, XRD studies showed reflections from Sn metal only. This suggests that the metal was phase segregated from an amorphous composite containing Si and C. Since we wished to employ films with reasonable growth rates, smooth surface, and balanced distribution of Sn and the amorphous Si/C composite, we selected samples 3 - 5, which were dark green in appearance, for the proposed study. These samples are denoted as sample **I** in the discussion below. This sample and the ones processed from it are summarized in Table 5.1. Rest of the samples, grown at the positions 1, 2 and 6 - 9 did not fit the selection criteria for further processing because they were too thin, too high or low in Sn content, and/or contained high quantity of large-sized particles.

**Table 5.1** Summary of samples.

| Sample | Processing Conditions | Color | Thickness (μm) | Pore sizes (nm) | Atomic % [a] | | | Si/C ratio |
|---|---|---|---|---|---|---|---|---|
| | | | | | Sn | Si | C | |
| **I** [b] | $Sn(SiMe_3)_4$ decomposed at 923 K, $H_2$ 20 sccm, 26.7 Pa for 6 h | Dark green | 5.6 | - | 33.6 | 29.4 | 37.4 | 0.8 |
| **I-P** | **I** treated with $H_2$ plasma at 923 K for 6 h | Gray | Not measured | - | Not measured | | | - |
| **I-P-HF** | **I-P** treated with 48 % $HF_{(aq)}$ at 298 K for 30 min | Black | Not measured | 10 – 50[c] | Not measured | | | - |
| **II** | **I-P-HF** annealed at 1273 K under vacuum for 6 h | Black | 3.0 | 10 – 50[d] | 0.1 | 23.0 | 76.9 | 0.3 |
| **III** | **I-P** annealed at 1423 K under vacuum for 1 h | Yellow | 3.5 | 10– 100[d] | 0.3 | 42.0 | 57.7 | 0.7 |
| **IV** | **I** (grown for only 90 min) annealed at 1423 K under vacuum for 1 h | Yellow | 0.6 | 20 – 100[c] | 0[e] | 49.8 | 49.7 | 1 |

[a] Atomic ratio were calculated from EPMA data. [b] From position 4 in the reactor. [c] Estimated from SEM image. [d] Estimated from SEM and TEM images. [e] Below detection limit.

Typical surface morphology of **I**, characterized by SEM, is displayed in Figure 5.5A. Elemental composition of **I**, determined by EDX, is shown in the inset of Figure 5.5A. It indicates that **I** contains Sn, Si, C, and traces of O. The EPMA data in Figure 5.4 show that the sample contained 33.6, 29.0 and 37.4 atomic % of Sn, Si, and C, respectively. A representative XRD pattern of **I**, as shown in Figure 5.5B, can be indexed to Sn metal (JCPDS, No. 04-0673).[24] The mean crystallite size of the metal is estimated to be 21.3 nm. This was calculated from Scherrer equation by using the width data of the Sn(200) reflections.

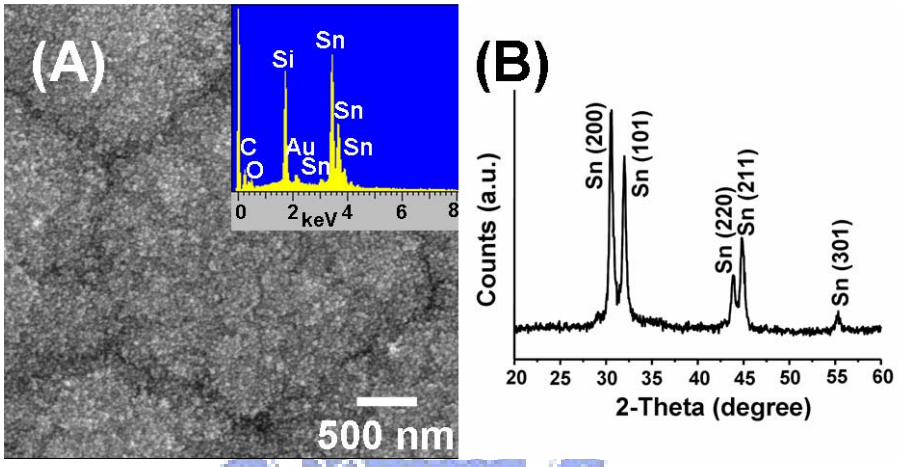


**Figure 5.5** (A) SEM, EDX (inset), and (B) XRD pattern of **I**. **I** was grown from $Sn(SiMe_3)_4$ at 923 K, $H_2$ flow rate 20 sccm, and 26.7 Pa.

XPS studies as shown in Figure 5.6 and 5.7 showed two binding energies of Sn $3d_{5/2}$ electrons at 486.9 and 484.9 eV. These were assigned to $SnO_2$ and Sn metal, respectively. The binding energies of Si 2p and C 1s electrons were observed at 100.9 eV and 283.2 eV, respectively.[25] The data suggest that Si and C atoms formed an amorphous $Si_xC_{1-x}$ matrix. Since Sn and Si have the same the electronegativity value of 1.8, it is difficult to conclude whether direct Sn-Si bonding existed in the film based on the XPS chemical shift data alone.[26]

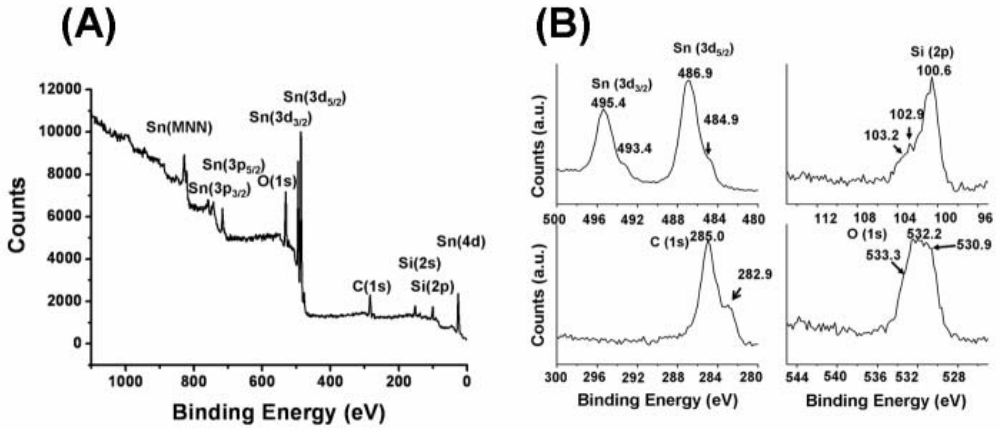


**Figure 5.6** XPS spectra of **I**, grown from $Sn(SiMe_3)_4$ at 923 K, $H_2$ flow rate 20 sccm, and 26.7 Pa, as received. (A) Survey and (B) high resolution spectra.

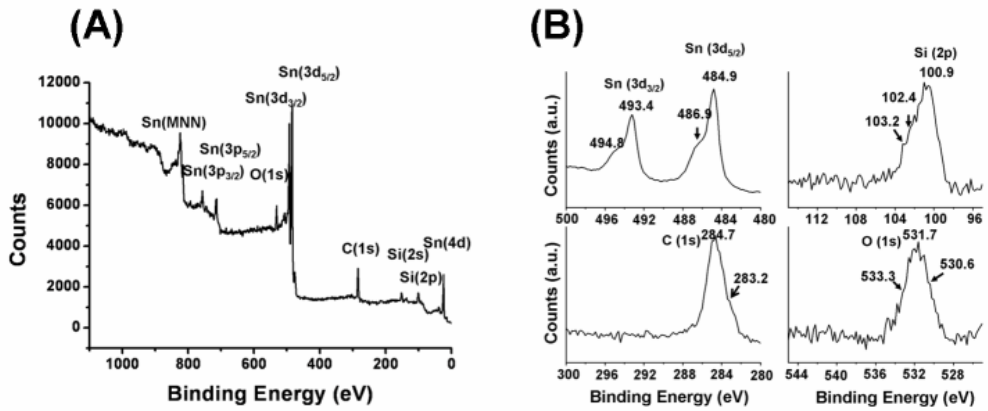


**Figure 5.7** XPS spectra of **I** after $Ar^+$ sputtering for 90 s. (A) Survey and (B) high resolution spectra.

In literature, it was reported that the Sn-Si vibration presented a Raman signal near 400 $cm^{-1}$.[27] For **I**, there was no clear Raman band assignable to this vibration as shown in Figure 5.8. Raman shift at 439.3 $cm^{-1}$ and 489.5 $cm^{-1}$ were assigned to silica bands, $\omega_1$ and $D_1$, respectively.[46] The FT-IR spectrum of **I** showed a broad absorption peak at 800.2 $cm^{-1}$, which

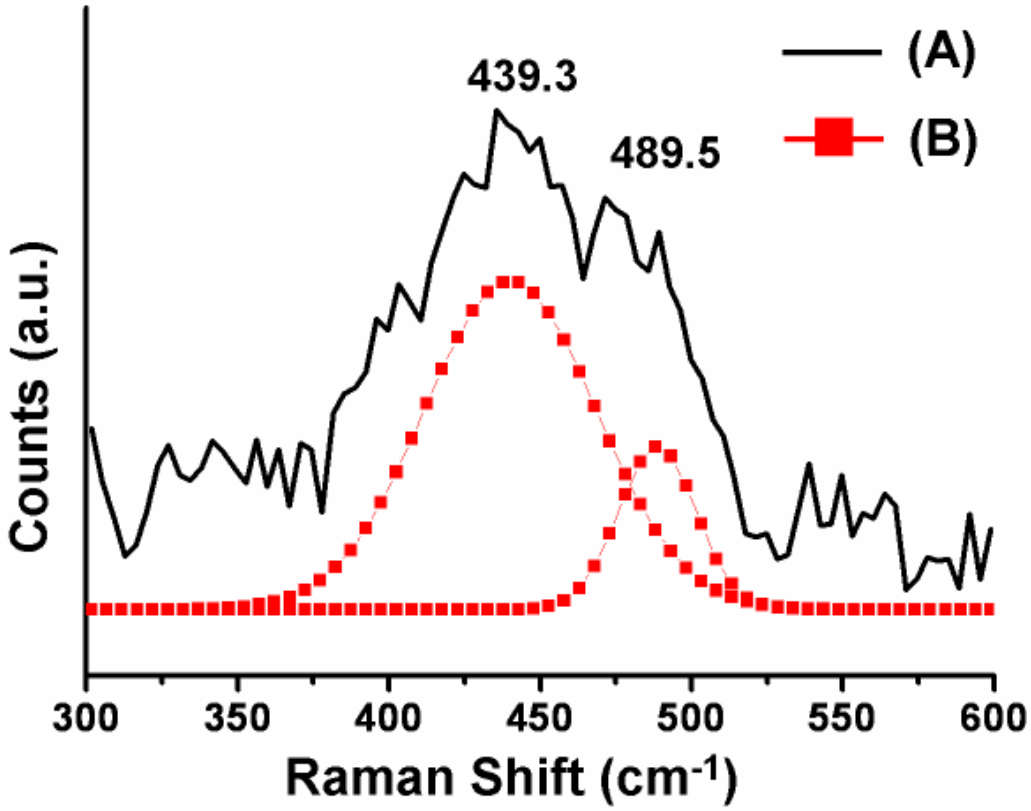


**Figure 5.8** (A) Raman spectrum of **I**, grown from $Sn(SiMe_3)_4$ at 923 K, $H_2$ flow rate 20 sccm, and 26.7 Pa. (B) curve fitting of (A).

can be assigned to the Si-C stretching mode as shown in Figure 5.12. Based on the above information, the film **I** is designatedas Sn/amorphous $Si_xC_{1-x}$ (x = 0.44 - 0.51). Even though the as-deposited film contained a significant quantity of Sn, it displayed low electrical conductivity (this will be discussed below in Electrical Property Studies). This intriguing observation suggests that in **I**, the Sn nanoparticles were dispersed evenly without contacting each other. This morphology would not allow electric current to pass through easily. Otherwise, if the film contained well-connected Sn particles, high electrical conductivity should have been observed.

### *5.3.2 Mesoporous amorphous $Si_xC_{1-x}$ (x = 0.3) Thin Films*

Attempts to remove the Sn nanoparticles by evaporation under low pressure were ineffective at 1273 K but successful at 1423 K. In another effort, we envisioned that by forming channels in **I**, Sn might migrate to the surface for easier removal. This was explored

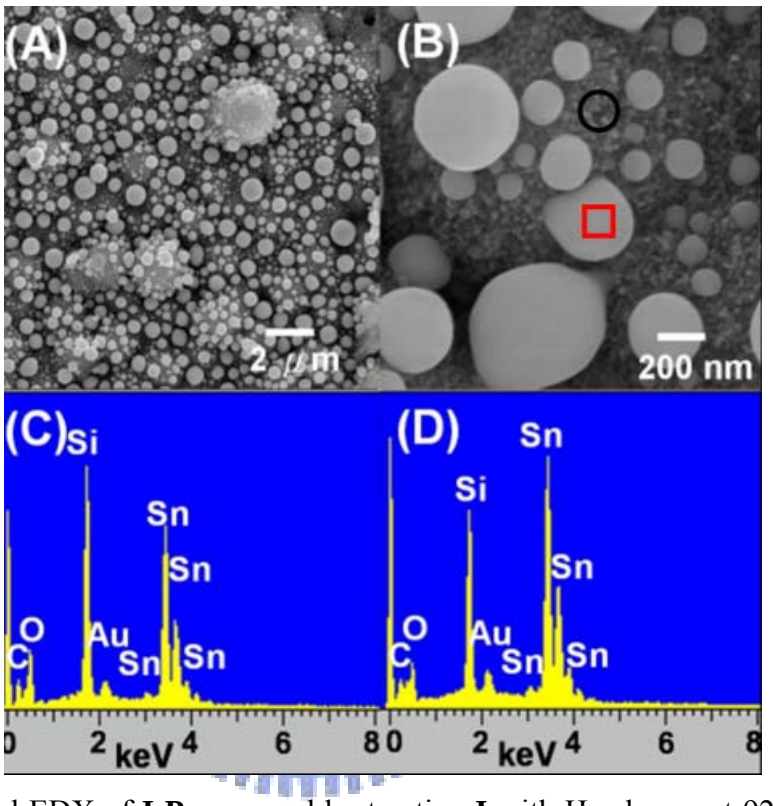


**Figure 5.9** SEM and EDX of **I-P**, prepared by treating **I** with $H_2$ plasma at 923 K. (A) Low and (B) high magnification image, EDX of (C) black circle and (D) red sequare in (B).

by exposing **I** to $H_2$-plasma at 923 K. The plasma treated samples are designated as **I-P**. Indeed, SEM images revealed that numerous spherical Sn particles with a diameter 100 – 500 nm formed on top of **I-P** as shown in Figure 5.9. Then, the samples **I-P** were dipped into an HF solution to offer samples **I-P-HF**. The SEM image in Figure 5.10A confirms that the spherical Sn particles were removed. The surface of **I-P-HF** appears to be uneven with randomly distributed spherical pores of 10 - 50 nm in diameter. The EDX in Figure 5.10B confirms that the Sn concentration in **I-P-HF** was reduced significantly. In contrast,

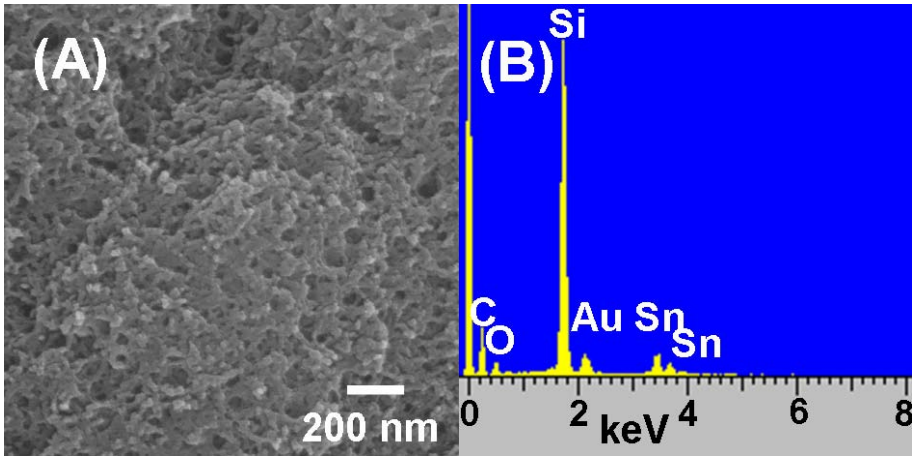


**Figure 5.10** (A) SEM and (B) EDX of **I-P-HF**, prepared by treating **I** with $H_2$ plasma at 923 K followed by etching in $HF_{(aq)}$ at 298 K.

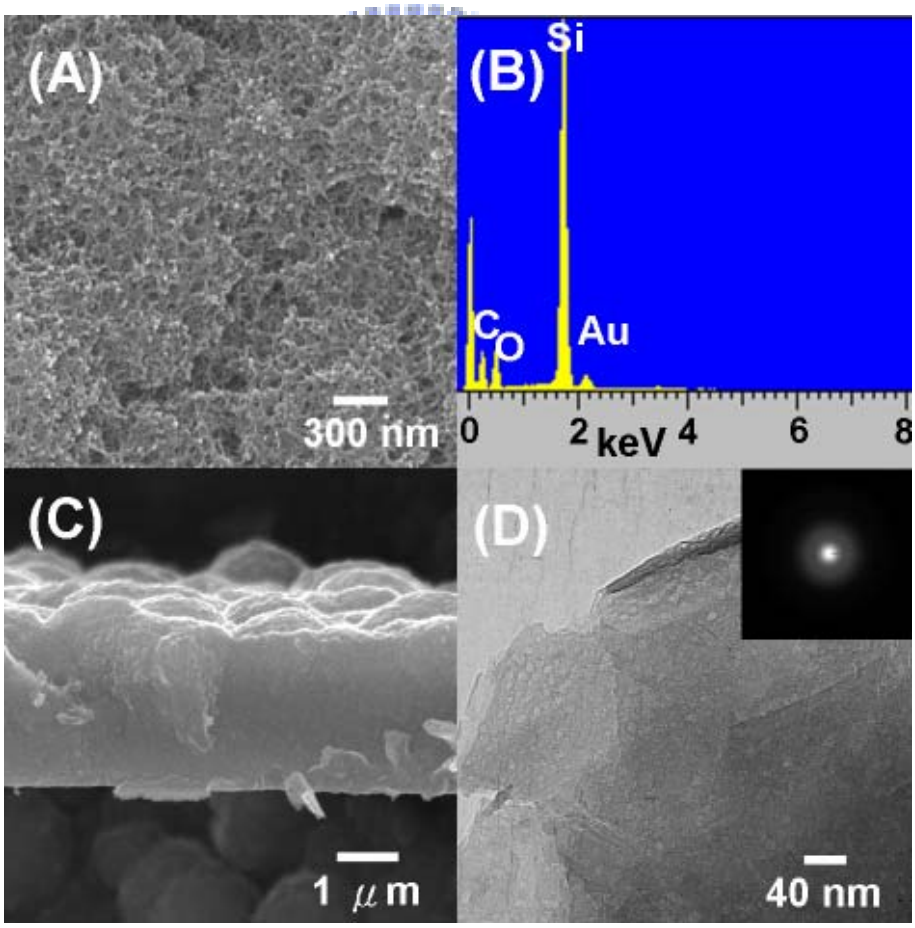


**Figure 5.11** (A) SEM, (B) EDX, (C) cross-sectional SEM, and (D) TEM and ED (inset) of **II**, obtained by annealing **I-P-HF** at 1273 K under vacuum.

apparently the other elements were not notably affected. Thus, we conclude that the film **I-P-HF** shown in Figure 5.10A is mesoporous amorphous $Si_xC_{1-x}$. After **I-P-HF** was annealed at 1273 K, sample **II** was obtained. It displays in Figure 5.11A basically the same mesoporous surface morphology, without any shrinkage and collapse, as **I-P-HF** does in Figure 5.10A. An EDX shown in Figure 5.11B indicates that **II** contains Si, C, and O but without any Sn. EPMA suggested that **II** contained 23.0% Si, 76.9 % C, and only 0.1% Sn. The Si/C atomic ratio of **II** was 0.3. In the SEM image shown in Figure 5.11C, the cross section of **II**, after being removed from the substrate, is displayed. It reveals that the thin film has an average thickness of 3 μm. Figure 5.11D shows a TEM image of **II** lifted from the wafer. The image

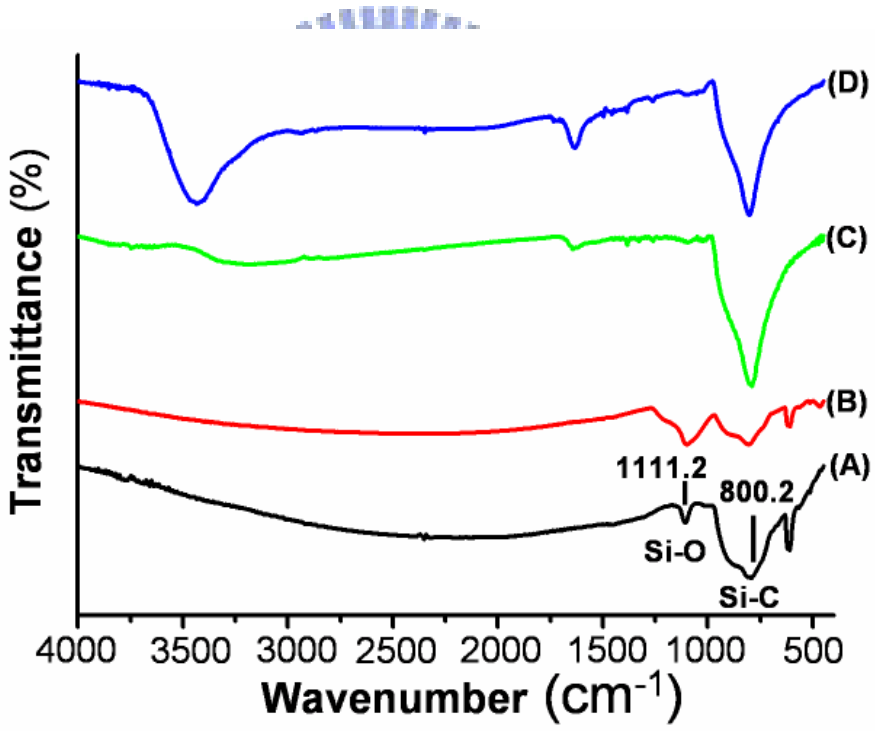


**Figure 5.12** FT-IR spectra of (A) **I**, grown from $Sn(SiMe_3)_4$ at 923 K, $H_2$ flow rate 20 sccm, and 26.7 Pa; (B) **I-P**, prepared by treating **I** with $H_2$ plasma at 923 K; (C) **I-P-HF**, obtained by etching **I-P** in $HF_{(aq)}$ at 298 K; and (D) **II**, obtained by annealing **I-P-HF** at 1273 K under vacuum.

reveals that the film contains numerous randomly distributed spherical pores of 10 - 30 nm in diameter. SAED (inset) reveals that the film is essentially amorphous and does not show any reflection spots from Sn. A FT-IR spectrum of **II** in Figure 5.12 showed a broad absorption at 800.2 $cm^{-1}$, which can be assigned to the Si-C stretching. This suggests that the processing at 1273 K removed residual Sn to form mesoporous amorphous $Si_xC_{1-x}$ (x = 0.3) **II**.

### *5.3.3 Mesoporous β-SiC Thin Films*

Sn nanoparticles can be evaporated successfully from **I** and **I-P** by heating them at 1423 K. In Figure 5.13, characterization of sample **III**, which was prepared by annealing **I-P** at 1423 K, is presented. In Figure 5.13A, the SEM image shows a mesoporous film surface with irregular pores of sizes 30 - 100 nm. The EDX shown in Figure 5.13B indicates that **III** contains only Si and C. EPMA showed that **III** contained 42.0% Si, 57.7 % C, and only 0.3% Sn. The Si/C atomic ratio of **III** was 0.7. The cross sectional SEM image shown in Figure 5.13C reveals that the film thickness of **III** stays at approximately 3.5 μm. After **III** was separated from the wafer, a low-magnification TEM image in Figure 5.13D shows a projected mesoporous structure with estimated pore spaces 10 - 80 nm. The SAED image in Figure 5.13E displays a ring pattern, which can be assigned to the reflections from (111), (220), and (311) planes of polycrystals with a cubic phase. The lattice parameter *a* is estimated to be 0.435 nm, which is consistent with the literature value of β-SiC.[28] A high resolution TEM (HRTEM) image of the wall of a pore, magnified from the red square in Figure 5.13D, is shown in Figure 5.13F. Some fringes spaced at 0.252 nm apart, which are originated from the (111) planes of β-SiC, can be observed.[28] In addition, XRD studies also confirmed that **III** was β-SiC as shown in Figure 5.14.

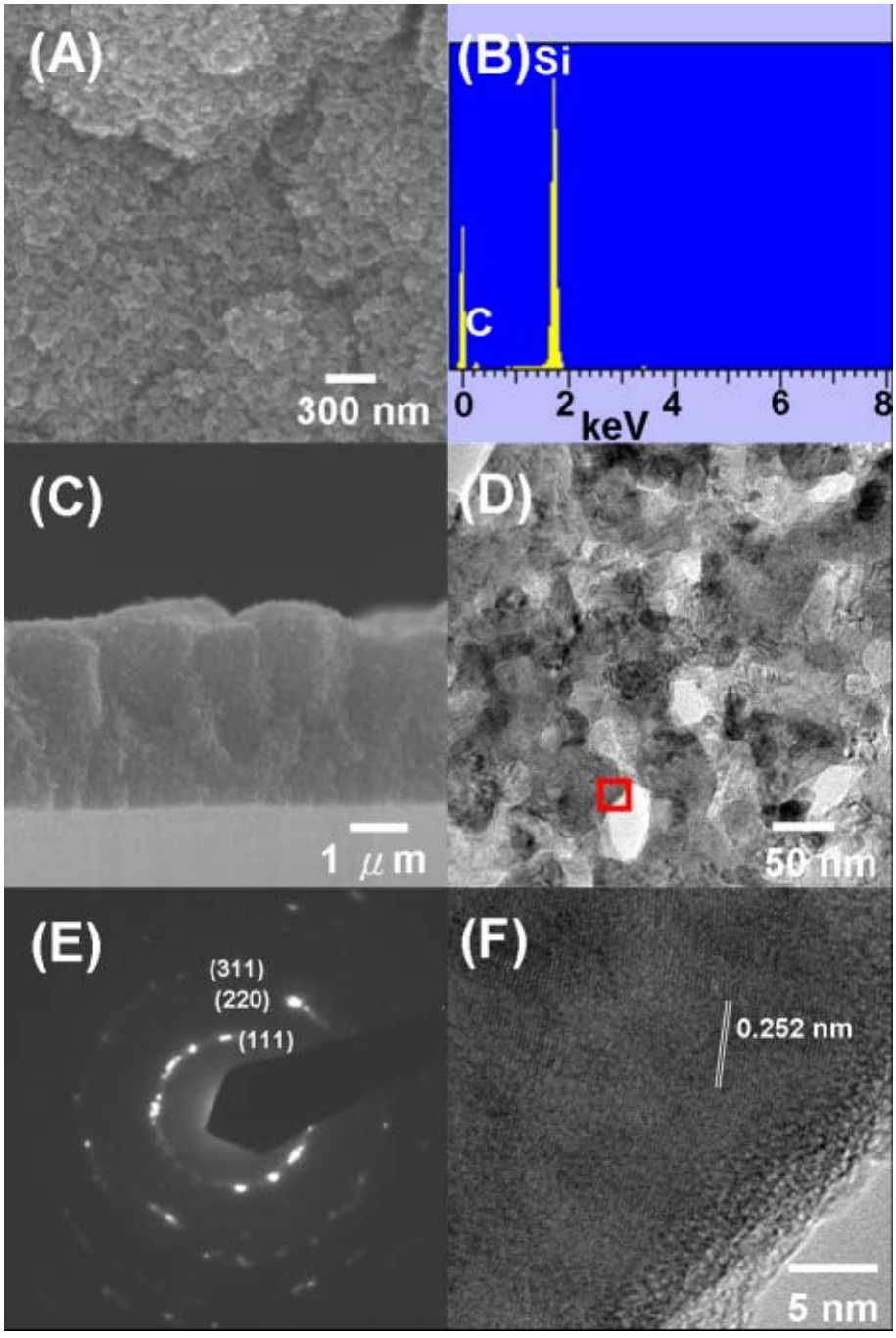


**Figure 5.13** (A) SEM, (B) EDX, (C) cross-sectional SEM, (D) low magnification TEM, (E) SAED, and (F) HRTEM from the red-square area in (D) of **III**, obtained by annealing **I-P** at 1423 K under vacuum.

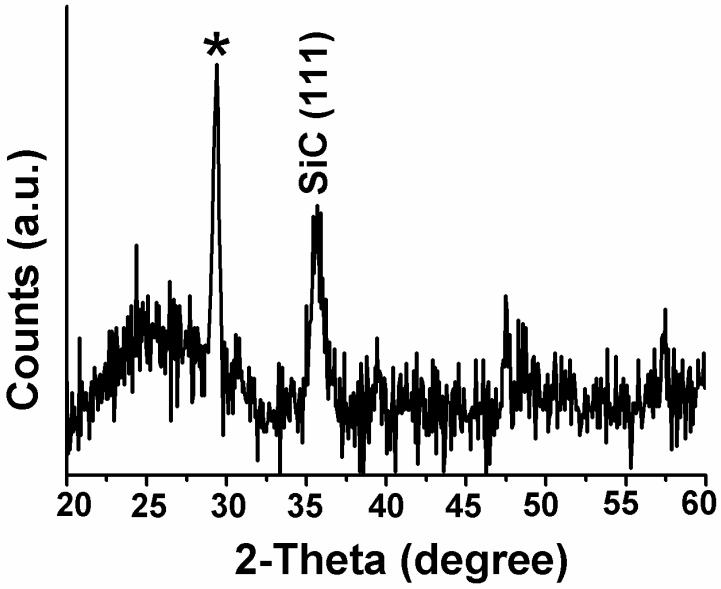


**Figure 5.14** XRD of **III**, obtained by annealing **I-P** at 1423 K under vacuum. (The peak marked with "*" is from the sample holder.)

### *5.3.4 Electrical Property Studies*

Figure 5.15 shows the I-V curves derived from electrical characterization of the thin films. **I** reveals a nonconductor type I-V curve in Figure 5.15A. As the applied bias was swept from -5 to +5 V, the obtained current increased only from -1.4 to +200 μA. This conduction feature is similar to that of well-dispersed metal nanoparticles, without contacting others, embedded in insulating materials.[29] In Figure 5.15B, **I-P** annealed at 1073 K shows a slightly curved I-V feature with an overall resistance of 386 Ω. Since the value is between the values of common metal and insulator, we propose that the Sn particles are loosely connected in this sample. In Figure 5.15C, **III** shows a non-linear I-V curve. At an applied bias of ± 5 V, the current passing through the junction between the film and the wafer in **III** is 0.1 - 27 mA. The resistivity, estimated from the sheet resistance, of **III** is 1.03 Ω·cm. This is within the literature values of undoped β-SiC thin films on Si wafers.[30,31]

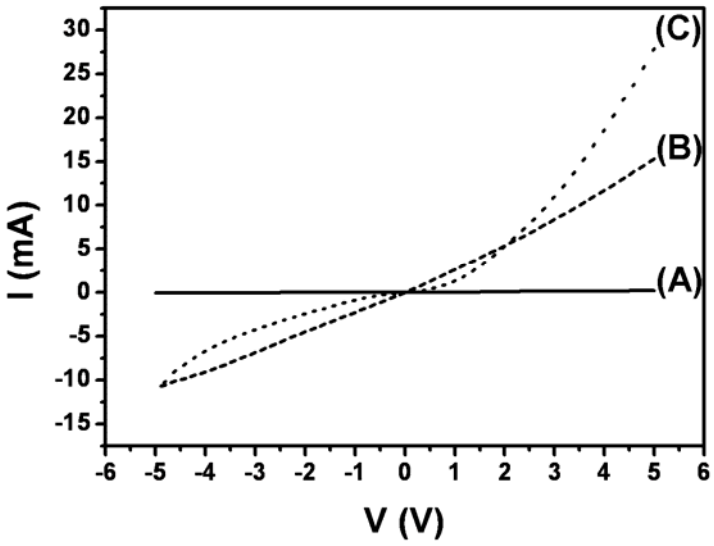


**Figure 5.15** I-V characters of (A) **I**, grown from $Sn(SiMe_3)_4$ at 923 K, $H_2$ flow rate 20 sccm, and 26.7 Pa; (B) **I-P** annealed at 1073 K, prepared by treating **I** with $H_2$ plasma at 923 K and annealed at 1073 K; and (C) **III**, obtained by annealing **I-P** at 1423 K under vacuum.

To evaluate potential device applications, P-N junction diodes were fabricated from mesoporous β-SiC films **IV** grown on p-type Si wafers. EPMA showed that **IV** contained 49.8% Si and 49.7 % C, which corresponds to the Si/C atomic ratio of 1. The Sn content was below the EPMA detection limit. I-V curves of the devices constructed from undoped and P-doped **IV** are shown in Figures 5.16A and 5.16B, respectively. Even β-SiC is an intrinsic n-type semiconductor, it is obvious that after the film was doped, the n-β-SiC/p-Si heterojunction is significantly improved to show a diode-like rectifying behavior.[32,33] A SIMS depth profile study in Figure 5.17 showed that C, P, and Sn secondary ion concentrations dropped significantly at a depth ca. 0.6 - 0.8 μm. This agrees well with the film thickness observed using SEM, 0.6 μm. At the junction, the P atom concentration was ca. $2 \times 10^{17}$ atoms/cm$^3$. We suggest that the diode performance was indeed enhanced by the doping process.

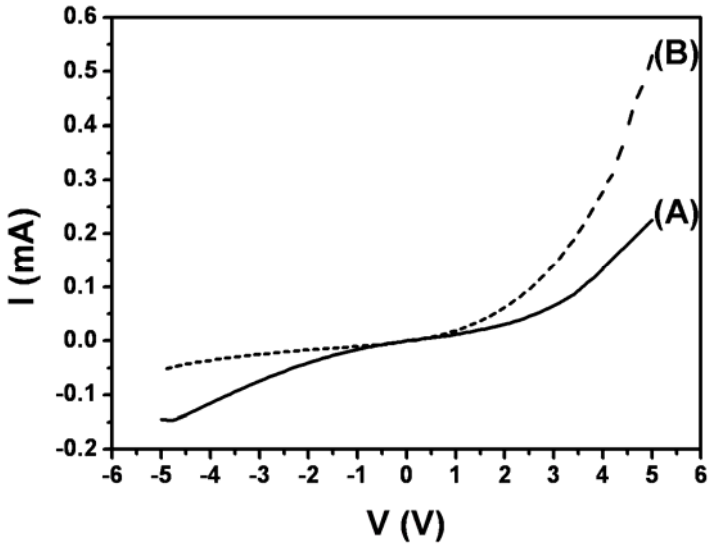


**Figure 5.16** I-V characters of (A) **IV**/p-type Si junction and (B) P doped-**IV**/p-type Si junction. **IV** was prepared by annealing **I** (grown for only 90 min) at 1423 K under vacuum for 1 h.

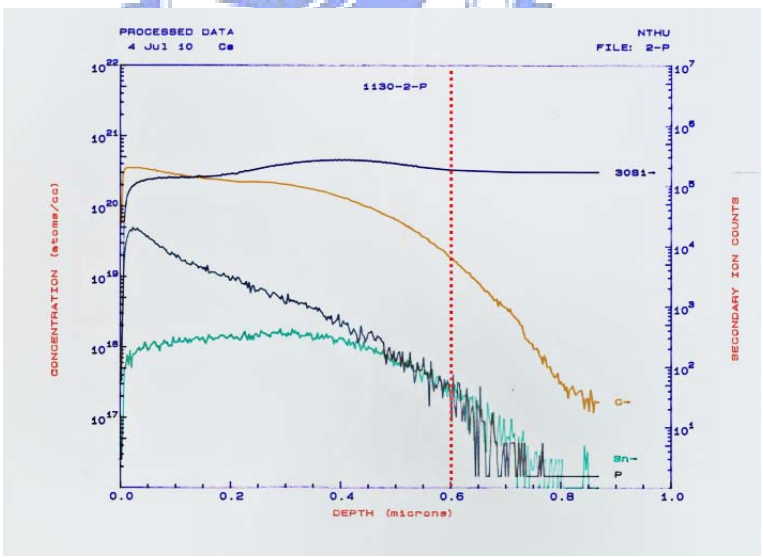


**Figure 5.17** SIMS depth profile of **IV**, obtained by annealing **I** (grown for only 90 min) at 1423 K under vacuum. (The thin film-substrate interface is proposed to be at 0.6 – 0.8 μm, starting at the red line.)

### *5.3.5 Reaction Pathway Elucidation*

Volatile species generated in the MOCVD process were trapped at 77 K and analyzed by GC-MS. The major components were identified to be $HSiMe_3$, $Si_2Me_6$, and $[Me_2SiCH_2]_2$ (1,1,3,3-teramethyl-1,3-disilacyclobutane) as shown in Figure 5.18. In addition to these molecules, on-line RGA data suggested that $H_2$, $CH_4$, $C_2H_2$, and $C_2H_4$, which could not be trapped at 77 K, were also formed in the decomposition process. Since no Sn containing molecules were detected in the gas phase byproducts and Sn crystallized into metallic nanoparticles, we propose that the Sn-Si bonds in the precursor $Sn(SiMe_3)_4$ decomposed extensively during the MOCVD process. $Sn(SiMe_3)_4$ might loose $SiMe_3$ radicals sequentially into metastable $Sn(SiMe_3)_3$ and $Sn(SiMe_3)_2$ species and finally into metallic Sn.[13, 34]

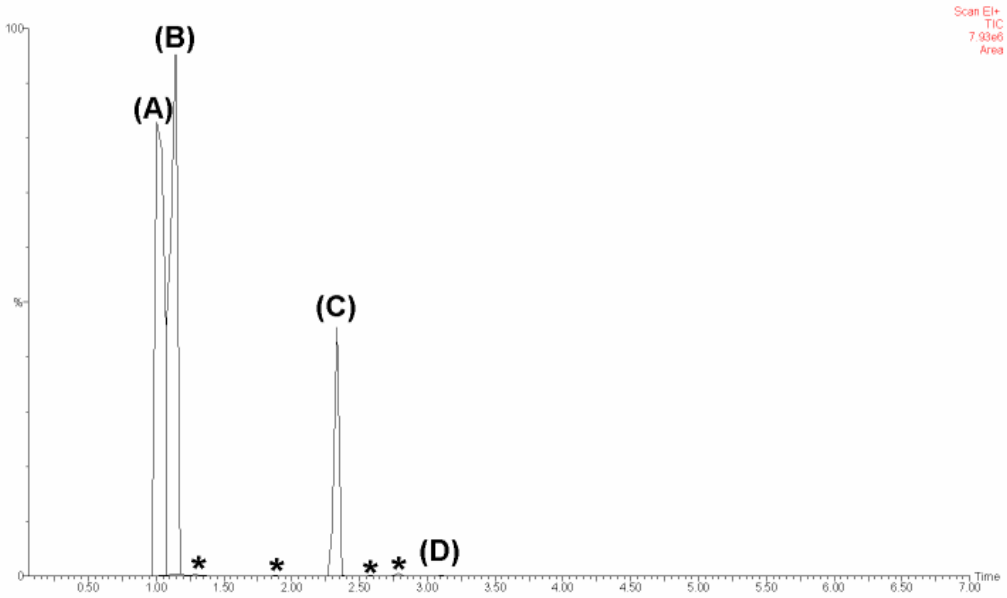


**Figure 5.18** GC-MS traces of volatile byproducts trapped at 77 K. The peaks are identified to be (A) air, (B) $Me_3SiH$, (C) $Me_6Si_2$, and (D) $[Me_2SiCH_2]_2$. (The peak marked with "*" are unidentified.)

These silyl species, including the $SiMe_3$ radicals evolved and the silane byproducts observed, probably decompose on the substrate surface to deposit the amorphous $Si_xC_{1-x}$ layer. Due to a

large size difference between the elements, the thermodynamic solubility of Sn in Si and C is low.[35,36] For example, thermal decomposition of alkyltin compounds generated elemental Sn and C.[37-39] In this study, the formation of phase-segregated Sn and amorphous $Si_xC_{1-x}$ is attributed to the same reason. This contrasts to the solubility of Ge in Si and SiC.[40-42] After the removal of Sn nanoparticles, the amorphous $Si_xC_{1-x}$ layer was transformed into β-SiC by thermal treatments.

A summary of this study is illustrated in a scheme in Scheme 5.1. Based on the experimental observations, we suggest that the initially deposited thin film **I** is a composite of sporadic Sn nanoparticles embedded in a preceramic amorphous $Si_xC_{1-x}$ layer. Then, upon $H_2$-plasma processing at 923 K, **I** is converted to **I-P**. In the process, **I** is etched to form volatile silanes and hydrocarbons and to leave pores and channels inside the films. These defects would allow fluidic Sn nanoparticles embedded in the preceramic amorphous $Si_xC_{1-x}$ layer to migrate to the surface easily. The Sn particles would agglomerate into larger ones in order to reduce the surface tension by ostwald ripening.[43-45] Then, the Sn particles could be removed from **I-P** by dipping it into an HF solution to generate a mesoporous amorphous $Si_xC_{1-x}$ thin film **I-P-HF**. After the film was annealed at 1273 K under vacuum to evaporate residual Sn, amorphous $Si_xC_{1-x}$ (x = 0.3) **II** retaining the mesoporous structure is formed. On the other hand, a simple annealing of **I-P** at 1423 K generates porous β-SiC **III** by evaporating Sn particles and crystallizing the SiC component in the film.

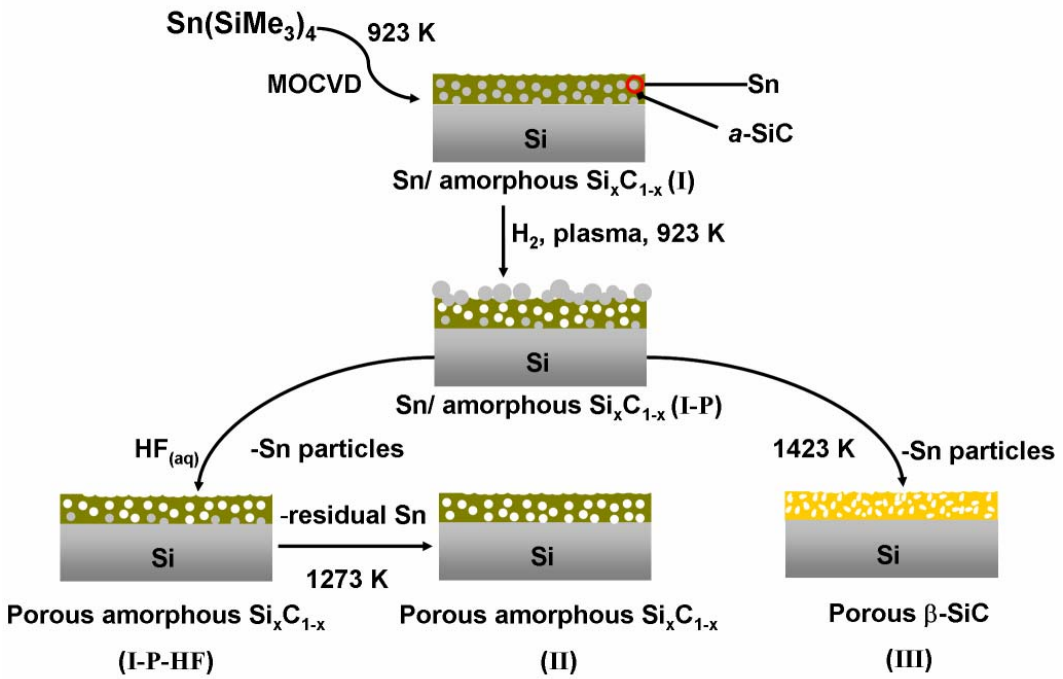


**Scheme 5.1** Reaction steps to form **II**, mesoporous amorphous $Si_xC_{1-x}$ (x = 0.3) and **III**, β-SiC thin films.

## 5.4 Conclusions

We have demonstrated a new strategy to fabricate mesoporous silicon carbide thin films by growing a precursor film which composites sporadic Sn nanoparticles embedded in amorphous $Si_xC_{1-x}$ on Si at 923 K by MOCVD from $Sn(SiMe_3)_4$. The unique phase segregated film structure is attributed to the low solubility of Sn in SiC. The phenomenon parallels the well-known phase-segregation found in many diblock and triblock copolymer systems.[2] The precursor film can be processed further under hydrogen plasma, in $HF_{(aq)}$, and at high temperature to remove Sn from the deposited layer and convert it into a mesoporous SiC thin film on Si. We also demonstrated how to fabricate p-n junction diodes from the mesoporous n-type SiC thin film on p-type Si wafer. We expect that many unique devices may be developed for future applications.

## 5.5 References


(1) (a) Brian, J.; Charles, F. K. *J. Sed. Petrol.* **1993**, *63*, 1018. (b) Guillaume, C.; Olivier, B.; Christophe, D.; Michel, A.; Eric, P. V. *Catena* **2005**, *59*, 1.

(2) (a) Muthukumar, M.; Ober, C. K.; Thomas, E. L. *Science* **1997**, *277*, 1225. (b) Förster, S.; Plantenberg, T. *Angew. Chem. Int. Ed.* **2002**, *41*, 688.

(3) Wang, C.-H.; Chang, Y.-H.; Yen, M.-Y.; Peng, C.-W.; Lee, C.-Y.; Chiu, H.-T. *Adv. Mater.* **2005**, *17*, 419.

(4) (a) Huang, C.-H.; Chang, Y.-H.; Lee, C.-Y.; Chiu, H.-T. *Langmuir* **2006**, *22*, 10; (b) Yen, M.-Y.; Chiu, C.-W.; Hsia, C.-H.; Chen, F.-R.; Kai, J.-J.; Lee, C.-Y.; Chiu, H.-T. *Adv. Mater.* **2003**, *15*, 235. (c) Hsia, C.-H.; Yen, M.-Y.; Lin, C.-C.; Chiu, H.-T.; Lee, C.-Y. *J. Am. Chem. Soc.* **2003**, *125*, 9940.

(5) (a) Chen, F.; Liu, M. *Chem. Commun.* **1999**, 1829. (b) Kyotani, T.; Ma, Z.; Tomita, A. *Carbon* **2003**, *41*, 1451. (c) Ramesh, P.; Kishi, N.; Sugai, T.; Shinohara, H. *J. Phys. Chem. B* **2006**, *110*, 130. (d) Vallé, K.; Belleville, P.; Pereira, F.; Sanchez, C. *Nature Mater.* **2006**, *5*, 107.

(6) Fissel, A.; Schroter, B.; Richter, W. *Appl. Phys. Lett.* **1995**, *66*, 3182.

(7) Spetz, A. L.; Baranzani, A.; Tobias, P.; Lundström, I. *Phys. Stat. Sol. (a)* **1997**, *162*, 493.

(8) (a) Shin, Y.; Wang, C.; Exarhos, G. J. *Adv. Mater.* **2005**, *17*, 73. (b) Li, Y.; Bando, Y.; Golberg, D. *Adv. Mater*. **2004**, *16*, 93.

(9) Hatakeyama, F.; Kanzaki, S. *J. Am. Ceram. Soc.* **1990**, *73*, 2107.

(10) Seog, I. S.; Kim, C. H. *J. Mater. Sci.* **1993**, *28*, 3227.

(11) (a) Yajima, S.; Hayasht, J.; Hasegawa, Y.; Iimura, M. *J. Mater. Sci.* **1978**, *13*, 2569. (b) Hasegawa, Y.; Iimura, M.; Yajima, S. *J. Mater. Sci.* **1980**, *15*, 720. (c) Hasegawa, Y.; Okamura, K. *J. Mater. Sci.* **1983**, *18*, 3633.

(12) Kamlag, Y.; Goossens, A.; Colbeck, I.; Schoonman, J. *Chem. Vapor Deposition* **2003**, *9*, 125.

(13) Chiu, H.-T.; Huang, S.-C. *J. Mater. Sci. Lett.* **1993**, *12*, 537.

(14) Pitcher, M. W.; Joray, S. J.; Bianconi, P. A. *Adv. Mater.* **2004**, *16*, 706.

(15) (a) Liu, Q.; Wu, H.-J.; Lewis, R.; Maciel, G. E.; Interrante, L. V. *Chem. Mater.* **1999**, *11*, 2038. (b) Cheng, Q.-M.; Interrante, L. V.; Lienhard, M.; Shen, Q.; Wu, Z. *J. Eur. Ceram. Sci.* **2005**, *25*, 233.

(16) Sonnenburg, K.; Adelhelm, P.; Antonietti, M.; Smarsly, B.; Nöske, R.; Strauch, P. *Phys. Chem. Chem. Phys.* **2006**, *8*, 3561.

(17) Lu, A.-H.; Schmidt, W.; Kiefer, W.; Schüth, F. *J. Mater. Sci.* **2005**, *40*, 5091.

(18) Krawiec, P.; Geiger, D.; Kaskel, S. *Chem. Commun.* **2006**, 2469.

(19) Matsumoto, T.; Takahashi, J.; Tamaki, T.; Futagi, T.; Mimura, H.; Kanemitus. Y. *Appl. Phys. Lett.* **1994**, *64*, 226.

(20) (a) Connolly, E. J.; O'Halloran, G. M.; Pham, H. T. M.; Sarro, P. M.; French, P. J. *Sens. Actuators A* **2002**, *99*, 25. (b) Connolly, E. J.; Timmer, B.; Pham, H. T. M.; Groeneweg, J.; Sarro, P. M.; Olthuis, W.; French, P. J. *Sens. Actuators B* **2005**, *109*, 44.

(21) (a) Shor, J. S.; Grimberg, I.; Weiss, B.; Kurtz, A. D. *Appl. Phys. Lett.* **1993**, *62*, 2836. (b) Rittenhouse, T. L.; Bohn, P. W.; Adesida, I. *Solid State Commun.* **2003**, *126*, 245. (c)

Rittenhouse, T. L.; Bohn, P. W.; Hossain, T. K.; Adesida, I.; Lindesay, J.; Marcus, A. *J. Appl. Phys.* **2004**, *95*, 490.

(22) Takazawa, A.; Tamura, T.; Yamada, M. *Jpn. J. Appl. Phys.* **1993**, *32*, 3148.

(23) Burger, H.; Goetze, U. *Angew. Chem. Int. Ed.* **1968**, *7*, 212.

(24) Joint Committee for Powder Diffraction (JCPDS) File No. 04-0673. International Center for Diffraction Data, 1982.

(25) Moulder, J. F.; Stickle, W. F.; Sobol, P. E.; Bomben, K. D. *Handbook of X-ray Photoelectron Spectroscopy*, Physical Electronics, Eden Prairie, MN, **1992**.

(26) Zumdahl, S. S. *Chemical Principles*, D. C. Heath and Company 2nd edn., Canada, **1995.**

(27) Tolle, J.; Chizmeshya, A. V. G.; Fang, Y.-Y.; Kouvetakis, J.; D'Costa, V. R.; Hu, C.-W.; Menéndez, J.; Tsong, I. S. T. *Appl. Phys. Lett.* **2006**, *89*, 231924.

(28) Joint Committee for Powder Diffraction (JCPDS) File No. 29-1129. International Center for Diffraction Data, 1982.

(29) Jin, Y. D.; Cahen, D.; Fridman, N.; Sheves, M. D. *Angew. Chem. Int. Ed.* **2006**, *45*, 6325.

(30) Gorin, S. N.; Ivanova, L. M. *Phys. Stat. Sol. (b)* **1997**, *202*, 221.

(31) Wijesundara, M. B.; Gao, J. D.; Carraro, C.; Howe, R. T.; Maboudian, R. *J. Cryst. Growth* **2003**, *258*, 18.

(32) Muto, H.; Asano, T.; Wang, R.-P.; Kusumori, T. *Appl. Phys. Lett.* **2005**, *87*, 162106.

(33) Furukawa, K.; Vemoto, A.; Shigeta, M.; Suzuki, A.; Nakajima, S. *Appl. Phys. Lett.* **1986**, *45*, 1536.

(34) (a) Wróbel, A. M.; Wickramanayaka, S.; Nakanishi, Y.; Hatanaka, Y.; Pawłowski, S.; Olejniczak, W. *Diamond Relat. Mater.* **1997**, *6*, 1081. (b) Wróbel, A. M.; Stanczyk, W. *Chem. Mater.* **1994**, *6*, 1766. (c) Wróbel, A. M.; Wickramanayaka, S.; Nakanishi, Y.; Fukuda, Y.; Hatanaka, Y. *Chem. Mater.* **1995**, *7*, 1403. (d) Wróbel, A. M.; Walkiewicz-Pietrzykowska, A. *Chem. Vap. Deposition* **1998**, *4*, 133.

(35) Massalski, T. B.; Okamoto, H.; Subramanian P. R.; Kacprzak, L. *Binary Alloy Phase Diagrams, ASM International, Materials Park, OH, 2nd edn.*, **1990**, *3*, 3361.

(36) (a) Ahn, H.-J.; Kim, Y.-S.; Park, K.-W.; Seong, T.-Y. *Chem. Commum.* **2005**, *1*, 43. (b) Fyhn, M. F.; Chevallier, J.; Larsen, A. N. *J. Vac. Sci. Technol. B*, **1998**, *16*, 1777. (c) Min, K. S. ; Atwater, H. A. *Appl. Phy. Lett.* **1998**, *72*, 1884.

(37) Margitfalvi, J. L.; Kolosova, I.; Tálas, E.; Gőbölös, S. *Appl. Catal. A* **1997**, *154*, L1.

(38) Kim, I.-S.; Blomgren, G. E.; Kumta, P. N. *Electrochem. Solid-State Lett.* **2004**, *7*, A44.

(39) Liu, Y.; Xie, J. Y.; Takeda, Y.; Yang, J. *J. Appl. Electrochem.* **2002**, *32*, 687.

(40) (a) Yonenaga, I. *J. Cryst. Growth* **2005**, *275*, 91. (b) Bolkhovityanov, Yu. B.; Deryabin, A. S.; Gutakovskii, A. K.; Revenko, M. A.; Sokolov, L. V. *J. Cryst. Growth* **2005**, *280*, 309.

(41) Biskupek, J.; Kaiser, U.; Gärtner, K. *J. Electron Microsc.* **2005**, *54*, 493.

(42) Chiu, H.-T.; Shie, C.-S.; Chuang, S.-H. *J. Mater. Res*. **1995**, *10*, 2257.

(43) (a) Wen, H.-C.; Yang, K.; Ou, K.-L.; Wu, W.-F.; Luo, R.-C.; Chou, C.-P. *Microelectronic Engineering* **2005**, *82*, 221. (b) Uh, H. S.; Park, S. S. *J. Electrochem. Soc.* **2004**, *151*, H164.

(44) Zhang, J. H.; Feng, T.; Yu, W. D.; Liu, X. H.; Wang, X.; Li, Q. *Diamond Relat. Mater.* **2004**, *13*, 24.

(45) (a) Weng, C.-H.; Su, H.-C.; Yang, C.-S.; Shin, K.-Y.; Leou, K.-C.; Tsai, C.-H. *Nanotechnology* **2006**, *17*, 5644. (b) Fillot, F.; Tökei, Zs.; Beyer, G. P.; *Surf. Sci.* **2007**, *601*, 986.

(46) Geissberger, A. E.; Galeener, F. L. *Phys. Rev. B.* **1983**, *28*, 3266.

# Chapter 6

# Synthesis of Gold Nanowires via Galvanic Displacement Reaction

## 6.1 Introduction

One dimensional gold nanowires have been attracted great attention due to its superior optical, electronic and physical properties compare to bulk solid.[1] So far, several methods for the creation of gold nanowires have already been reported. These included, soft template, surfactant directed growth form spherical seeds and hard templates such as porous alumina oxide member, membranous polycarbonate, and carbon nanotube assisted growth.[2-3] It is not easy to produce high aspect ratio gold nanowires from surfactant directed growth method. Also, it is inconvenient to remove hard templates. Previous, our group reported a surfactant assisted synthesis of single crystalline cubic phase 3C Cu nanobelt and hexagonal phase 4H Ag belt-like materials via galvanic reductions. In the reaction, metal salts were reduced by bulk metal in the presence of CTAC (cetyltrimethylammonium chloride).[4] Here, we demonstrated that by using the same methodology, high aspect ratio gold nanowires can be grown on the surface of amorphous $Si_xC_{1-x}$. This is achieved via galvanic reductions of $HAuCl_4$ solution in the presence of CTAC by Sn nanoparticles embedded in amorphous $Si_xC_{1-x}$ layer obtained from sample **I** in Chapter 5.

## 6.2 Experimental.

### *6.2.1 Synthesis of Gold Nanowires*

Dark green thin film on Si wafer (from Chapter 5, sample **I**) was add to aqueous solution of $HAuCl_4$ (2 mM, 2 mL), and CTAC (7.2 mM, 2 mL). The mixture was then placed at room temperature without stirring. After 20 h, the dark green thin film on Si wafer was removed

and rinsed by deionized water. The surface color of the thin film on Si wafer turned from dark green to brown red.

### *6.2.2 Characterization*

SEM and EDX spectroscopic data were collected using a JEOL JSM-6330F at 15 kV. TEM and ED images were obtained on a JEOL JEM-2010 at 200 kV. HRTEM images were acquired on a JEOL JEM-4000EX at 400 kV. XRD studies were carried out using a BRUKER AXS D8 ADVANCE diffractometer using Cu Kα1 radiation. The electric property of gold nanowires were measured by multi-probe nano-electronics measurement system combined with a field emission gun scanning electron microscopy, JEOL JSM-7000F, four needles experimental probing device, Kammrath & Wiess GmbH, and I-V measurement system, Keithley Model 4200-SCS.

## 6.3 Result and Discussion

### *6.3.1 Characterizations of Gold Nanowires*

Figure 6.1 shows the results of the brown red thin films grown from $HAuCl_4$ in the CTAC solution at room temperature. A low-magnification SEM image displays numerous one-dimensional nanostructures with tens of micrometers in length on the surface in Figure 6.1. An EDX spectrum shown in the inset of Figure 6.1A indicates that it contained Si, C, Sn, and strong Au intensity is addition to the original elements. In addition to, some particles and triangular plate nanostructures, high-magnification SEM image shows one-dimensional nanostructures with diameters of 60 - 100 nm in Figure 6.1B. A bright field TEM image presents a typical nanowire with a diameter of 70 nm in Figure 6.1C. The SAED pattern in the inset of Figure 6.1C insert shows a spot pattern revealing single crystalline nature of the nanowire. The pattern was indexed to be viewing along the [-1,1,1] zone axis of a face-centered-cubic (f.c.c.) structure. The lattice parameter *a* was estimated to be 0.405 nm, close to the reported value of Au metal.[5] From the pattern, projected growth direction of the

nanowire was determined to be along [1,1,0] direction. A high resolution TEM (HRTEM) image of the area marked with red square in Figure 6.1C is shown in Figure 6.1D. The d spacing was measured to be 0.238 nm, close to the value estimated from the literature data, 0.236 nm Au (111).[5] Figures 6.1E shows an XRD pattern of the sample. The intensity peaks could be indexed to Au metal (JCPDS, No 04- 0784)[5] besides Sn metal (JCPDS, No 04-0673).[6]

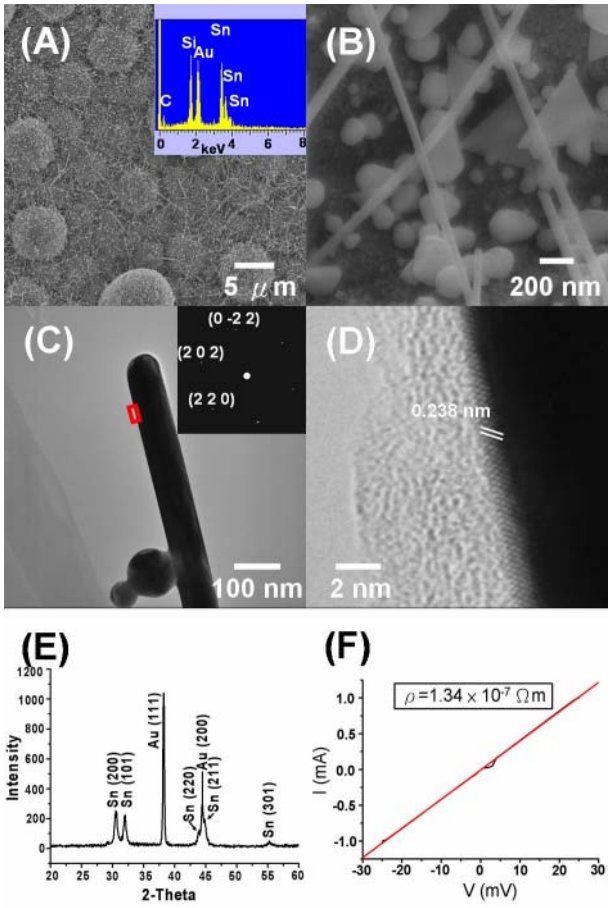


**Figure 6.1** Characterization of the dark green thin films reacted with $HAuCl_4$ in the CTAC solution.(A) low-magnification SEM image, and EDX (inset) (B) high- magnification SEM image (C) low magnification TEM image and SAED (inset) (D) high resolution TEM image (E) XRD partten, and (F) plot of current-voltage (I-V) curve of a gold nanowire.

The electrical property of an Au nanowire was measured by multi-probe nano-electronics

measurement system combined with a field emission gun scanning electron microscopy. Two-terminal current-voltage (I-V) curve of a gold nanowire is shown in Figure 6.1F. The nanowire's resistivity estimated to be $1.34\times 10^{-7}$ Ω·m, close to the reported value $1.5\times 10^{-7}$ Ω·m, but larger than the resistivity of bulk gold, $2\times 10^{-8}$ Ω·m.[1]

### *6.3.2 Proposed Growth Mechanism of Au Nanowires*

Comparatively, the Sn metal foil, instead of Sn nanoparticles embedded in amorphous $Si_xC_{1-x}$ to react with $HAuCl_4$ in CTAC at the comparable conditions did not grow Au nanowires. Particles and some dendridic structures were obtained. The preparation of Au nanowies is dependent on the presence of CTAC. Without it, the uncontrolled growths could produce particles structures only. A generalized CTAC assisted growth is presented Scheme 6.1. It describes the overall growth process. This deseribes the Galvanic reduction of $Au^{3+}_{(aq)}$ by more active $Sn_{(s)}$ to form Au nanowires. The $Au^{3+}_{(aq)}$ ions are reduced, then nucleate into Au metal on the amorphous $Si_xC_{1-x}$ surface. The reaction is spontaneous due to a positive redox potential $E^o = 1.13$ V, for the reaction $2\ AuCl_4^-{}_{(aq)} + 3\ Sn_{(s)} \rightarrow 2\ Au_{(s)} + 3\ Sn^{2+}_{(aq)} + 8Cl^-_{(aq)}$.[7] CTAC molecules probably adsorbe selectively on crystallographically facets (100), and (111) of a Au seed to form a bilayer interface structure.[8,9]

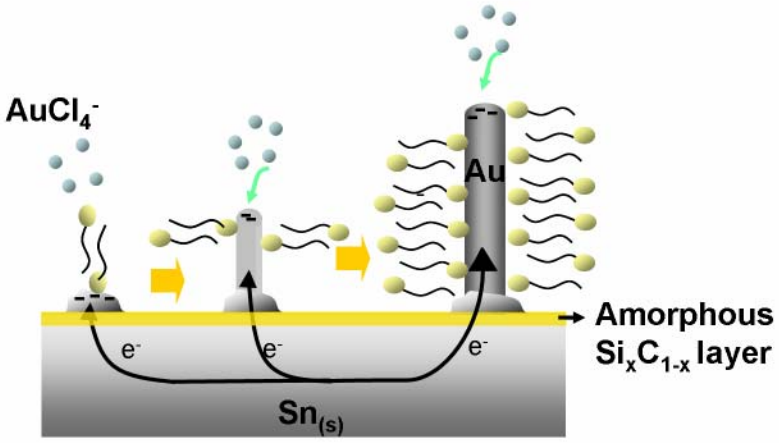


**Scheme 6.1** Propose the growth mechanism of Au nanowires.

Through the ionic ends of the surfactant molecules, one side of the CTAC bilayer binds to the

Au surface while the other side interfaces with the aqueous medium. Between two ionic sides, the aliphatic chains form an inner nonpolar sheet. This specific arrangement restricts the deposition of Au atoms on the CTAC passivated facets. Consequently, the Au crystal grows within the CTAC bilayer soft template and develops into a nanowire.

### 6.4 Conclusions

We have successful revealed that the Sn nanoparticles embedded in amorphous $Si_xC_{1-x}$ can be an excellent reductant to grown Au nanowires in a proper condition. In the future, we will grow gold nanowires on various substrates for special applications.

## 6.5 References


(1) (a) Keren, K.; Krueger, M.; Gilad, R.; Ben-Yoseph, G.; Sivan, U.; Braun, E. *Science* **2002**, *297*, 72. (b) Ma, F.; Xu, K. *Scripta Mater.* **2006**, *55*, 951.

(2) (a) Murphy, C. J.; Gole, A. M.; Hunyadi, S. E.; Orendorff, C. J. *Inorg. Chem.* **2006**, *45*, 7544. (b) Busbee, B. D.; Obare, S. O.; Murphy, C. J. *Adv. Mater.* **2003**, *15*, 414.

(3) (a) Kline, T. R.; Tian, M.; Wang, J.; Sen, A.; Chan, M. W. H.; Mallouk, T. E. *Inorg. Chem.* **2006**, *45*, 7555. (b) Wirtz, M.; Martin, C. R. *Adv. Mater.* **2003**, *15*, 455. (c) Fullam, S.; Cottell, D.; Rensmo, H.; Fitzmaurice, D. *Adv. Mater.* **2000**, *12*, 1430.

(4) Huang, T.-K.; Cheng, T.-H.; Yen, M.-Y.; Hsiao, W.-H.; Wang, L.-S.; Chen, F.-R.; Kai, J.-J.; Lee, C.-Y.; Chiu, H.-T. *Langmuir*, **2007**, *23*, 5722.

(5) Joint Committee for Powder Diffraction (JCPDS) File No. 04-0784. International Center for Diffraction Data, 1982.

(6) Joint Committee for Powder Diffraction (JCPDS) File No. 04- 0673. International Center for Diffraction Data, 1982.

(7) Bard, A. J.; Faulkner, L. R. Electrochemical Methods: Fundamentals and Applications, John Wiley & Sons, New York, **1980**.

(8) Gao, J.; Bender, C. M.; Murphy, C. J. *Langmuir* **2003**, *19*, 9065.

(9) Nikoobakht, B.; El-Sayed, M. A. *Langmuir* **2001**, *17*, 6368.

# Chapter 7

# Conclusions

Most materials come into nanoscale regime may reveal unique physical or chemical perpoties. The shapes effect also must be considerded besides size effect. Now it is well known that inorganic $sp^2$ carbon can form 0D fullerenes, 1D nanotubes, and stacked into 3D graphite from basic 2D graphene build blocks in nature. Diamond, which is constructed by $sp^3$ C, can be considered as a 3D bulk material. For all of theses carbon material, they reveal distinctive perpoties different from others. The SiC material studied here is a group 14 – group 14 binary compound. But it is not as easy to form low dimensional structures as carbon can do. Most studies report that hard templates must be added to assist morphology formation. In this thesis, we have demonstrated that 0D to 3D SiC nanostructures can be successfully fabricated form self-templating methods based on phase segregation at the reaction interface as shown in Figure 7.1.

We have developed vapor-liquid and vapor-solid reactions to prepare dersired SiC nanostructures. Different preceramic precursors were obtained form various vapors of organochlorosilanes to react with metal at varios reaction temperatures. These precramic studies showed different affinities to the salt products. The final products revealed the distinctive morphologies of the salt shapes. For example, three dimensional SiC cubic nanocages can be obtained from the ractions forming NaCl as the in-situ template. Two dimensional pseudo thin plates SiC and one dimensional tubular SiC can be obtained form $MgCl_2$ and $CaCl_2$ templates, respectively. On the other hand, rigid preceramic polymers could not cover the salt products. Thus, zero dimensional SiC nanoparticles are produced from the reaction between $MeSiCl_3$ and sodium.

In addition, we extended the phase segregation idea to grow porous SiC thin films on Si

wafers. We used $Sn(SiMe_3)_4$ as the MOCVD precursor to grow amorphous $Si_xC_{1-x}$ layer with in-situ generated Sn nanoparticles. The results are summarized in Figure 7.2. The porous SiC thin films were formed after the Sn naoparticles were removed.

Possible applications of the materials fabricated in this study are summarized in Figure 3. One dimensional tubular SiC nanostructures are an excellent candidate for field emission applications. From the tubes, emission of electrons with a current 10 $\mu A/cm^2$ can be obtained at an applied field as low as 2.5 V/μm. The data are much lower than most of the reported data of other SiC nanostructures. This excellent result indicates that the SiC tubes may have promising field-emitting applications for vacuum microelectronic devices. For another potential device application, we also demonstrated the p-n junction diode property via dopping P into the mesoporous n-type SiC thin film on p-type Si wafer. Furthermore, Sn nanoparticles embedded in the amorphous $Si_xC_{1-x}$ thin film can function as a reductant for the growth of one dimensional Au nanowires from a solution of $HAuCl_4$ and CTAC.

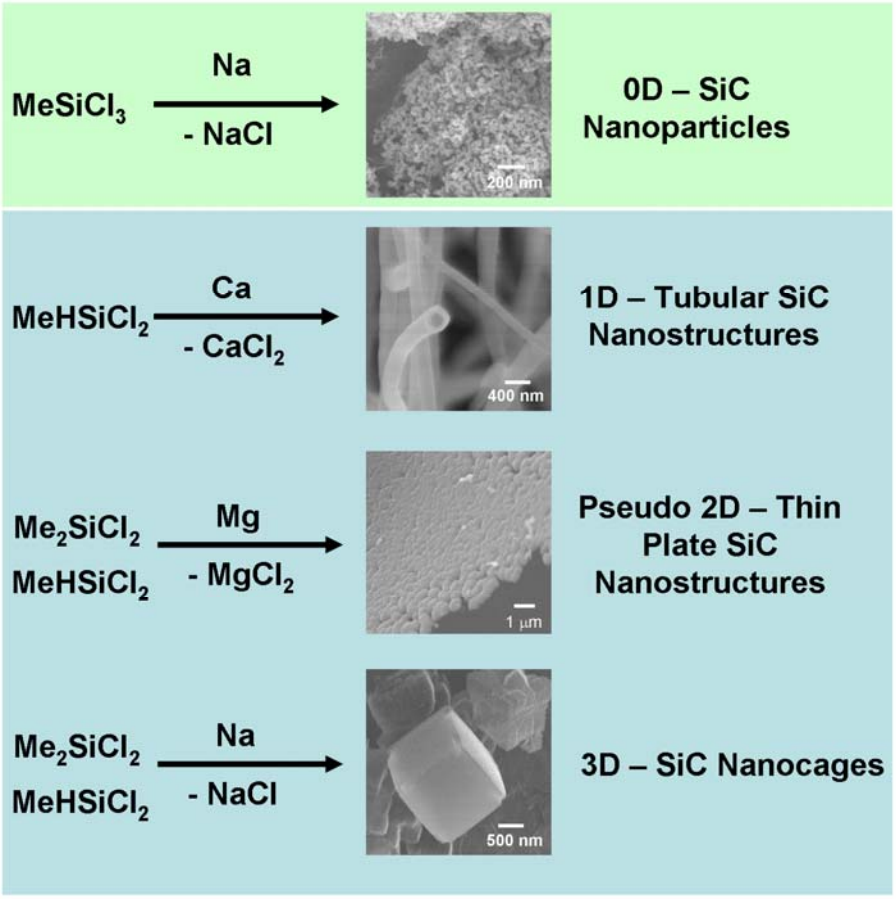


**Figure 7.1** SiC nanostructures obtained in this study from self-templating methods.

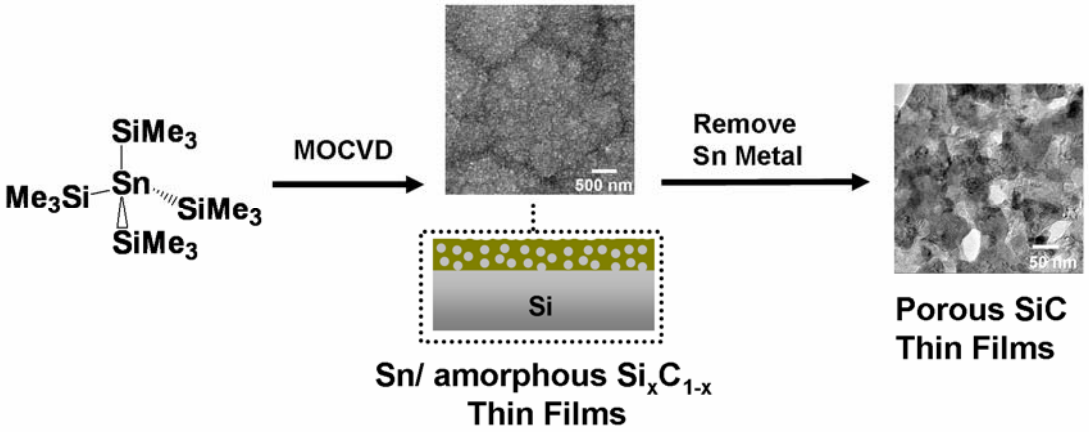


**Figure 7.2** Summarized the results from Sn nanoparticles embedded in amorphous $Si_xC_{1-x}$ thin films via $Sn(SiMe_3)_4$ as MOCVD precursor.

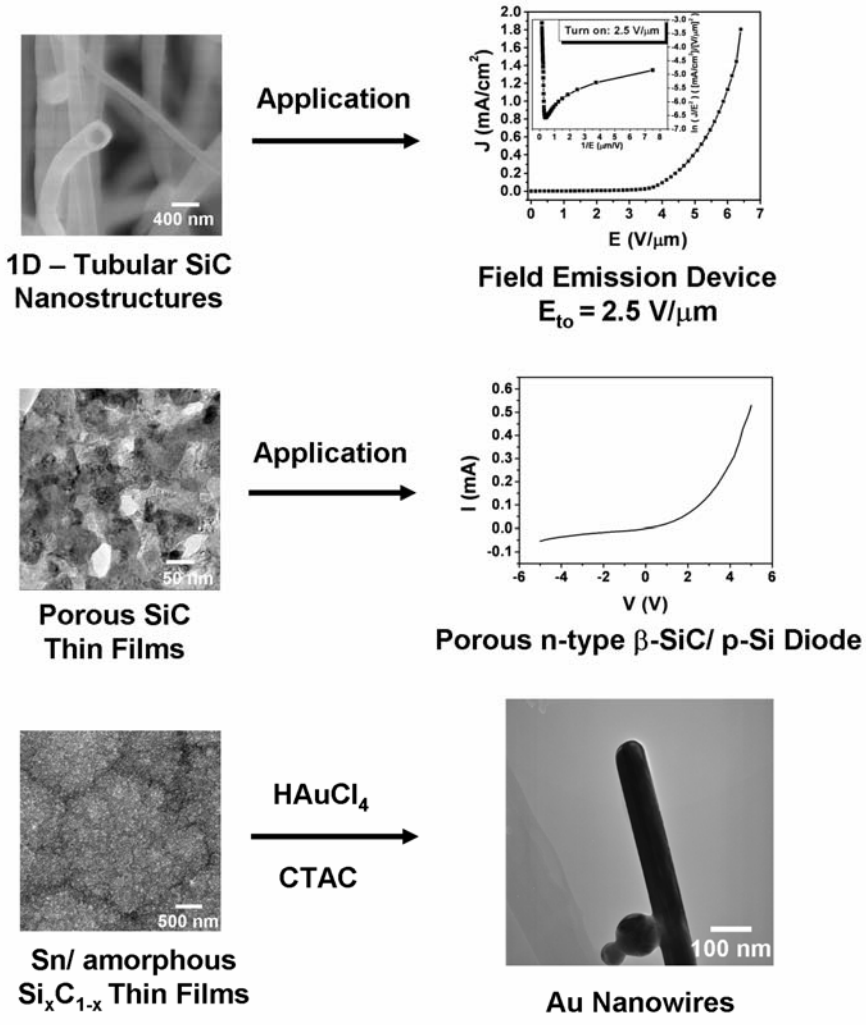


**Figure 7.3** Summarized the possible applications of the materials fabricated in this study.